Technische Universität München

Physik Department E20

Molecular Nanoscience and Chemical Physics of Interfaces

Supramolecular architectures as templates for atomic and molecular confinement

Dissertation

Saranyan Vijayaraghavan

TECHNISCHE UNIVERSITÄT MÜNCHEN

Lehrstuhl E20 -
Molekulare Nanowissenschaften & Chemische Physik von Grenzflächen

Supramolecular architectures as templates for atomic and molecular confinement

Saranyan Vijayaraghavan

Vollständiger Abdruck der von der Fakultät für Physik der Technischen Universität München zur Erlangung des akademischen Grades eines Doktors der Naturwissenschaften (Dr. rer. nat.) genehmigten Dissertation.

Vorsitzender:	Univ.-Prof. Dr. Björn Garbrecht
Prüfer der Dissertation:	1. Univ.-Prof. Dr. Johannes Barth
	2. Univ.-Prof. Dr. Friedrich Simmel

Die Promotion wurde am 21.06.2013 bei der Technischen Universität München eingereicht und durch die Fakultät für Physik am 10.07.2013 angenommen.

To my parents

Abstract

Selective confinement of atoms and molecules is of paramount importance in order to address them individually, understand their physicochemical properties and fabricate potential single molecule devices. In two-dimension (2D), such confinement could be achieved by capturing individual species using molecular porous networks or hosting them on dense packed molecular arrays. In the present thesis, distinct supramolecular networks are tailored in 2D on noble metal surfaces and characterized with an STM at low temperatures ($\sim$ 6 K). The networks are further used as templates for confining individual molecules or atoms which are investigated with angstrom scale precision. Firstly a threefold symmetric molecule is examined on Ag(111) and Cu(111), where robust nano-porous networks evolve, stabilized by pyridyl-pyridyl or metal-organic interactions or a combination of both. A $Ce(TPP)_2$ sandwich complex is confined in the porous network created on Cu(111). Furthermore, dense-packed islands of $Ce(TPP)_2$ are created by sublimation onto the Ag(111) surface. These networks are used for the confinement of C_{60} molecules which are studied individually, as extended arrays and mixed $C_{60}/Ce(TPP)_2$ architecture. Finally, Fe atoms are positioned on the macrocycle of Cobalt-tetraphenyl porphyrin (Co-TPP) molecules adsorbed on Ag(111). The individual Fe atoms were manipulated by the STM tip to create an atomic switch. Various coverages of Fe were studied on the Co-TPP arrays. X-ray magnetic circular dichroism (XMCD) experiments on the Fe-CoTPP system complement the structural information and reveal detailed insights into the electronic configuration. DFT studies provide additional explanation for the STM and XMCD results on the Fe-CoTPP system.

Contents

List of Figures

1 Introduction

1.1 Background

Long long ago, around the year 500 B.C, the greek philosopher Leucippus suggested that when matter is divided smaller and smaller, it would at some point lead to an indivisible unit which he called 'atom'. Aristotle dismissed that idea as worthless and hence the concept of atoms lay hidden for more than 2000 years. In the early 1800's the English naturalist Dalton, proposed that matter consists of minute particles and his experiments hinted towards something fundamental. From then on, 19th and the 20th century saw a huge development in the scientific understanding that not only proved beyond doubt the existence and nature of atoms, but also the subatomic constituents of it.

Even though atoms make up all of the universe's matter, we have little control in directing their behavior into more complex matter. It was nature's business to make complex matter and all the knowledge about fundamental particles were arrived at by investigating macroscopic objects and theoretical understanding. However, once we have such control over matter in atomic dimensions, we are already on the way to understand nature's way of building things into more sophisticated systems like organic or bio-molecules and their chemical composition. This understanding in turn leads to decipher the role of atoms or molecules in more convoluted systems like molecular self-assemblies, symmetries in nature, phenomena at the quantum scale and the nature of chemical bonds.

A fairly good understanding of atomic structure was achieved by the mid-20th century through the help of a rich theoretical platform of quantum mechanics. This understanding led to miniaturization of practical devices like electronic circuits, which began with the advent of the transistor in 1947 and consequently the efficiency of electronic devices was progressive over the years.

Richard Feynman, in 1959, suggested that the miniaturization of devices achieved by that contemporary electronics were nowhere near that of what could be achieved with controlled manipulation of atoms. [1] Feynman prophesied that if we could arrange the atoms in the way we want, we could miniaturise electronics and information storage to unimaginably small dimensions. For example, he mentioned that if we could write each word with only atoms, the whole 24 volumes of *Encyclopedia Brittanica* could be written on the head of a pin. And instead of writing the exact words with atoms, if we use codes to store information by arranging atoms in certain ways, all the information ever published in the world could be stored in the size of a dust particle. The technology present at the time when he gave his talk was not developed enough to see the manifestation of his ideas.

Over the years after Feynman gave his talk, techniques like electron beam lithography and ion beam lithography became more common for etching designs in microscopic dimensions. But the resolution of these techniques were still bigger than the dimensions of an atom. It was only after the invention of the Scanning Tunneling Microscope (STM) by Rohrer and Binnig in 1982, a phenomenal development was seen in imaging at the nanoscale. Even though older techniques like field ion microscope (**FIM**) were capable of making atomic resolution images, the imaging was restricted to the outer area of a tip made of specific materials and the experiments required complicated set-up and high electric fields. After the invention of the STM, it was possible for the first time to visualize atoms and molecules on all conducting surfaces in real space with considerable ease. Since its invention STM has become an indispensable tool in the field of surface science.

1.1.1 Scanning tunneling microscopy

STM is a very convenient and important instrument to study surfaces and atoms or molecules adsorbed on these surfaces. In the initial experiments after the invention of STM, a Si(111)-7×7 surface was resolved with atomic resolution. [2] But over the years STM grew more than a mere tool for imaging. Several successful manipulation experiments were performed by individually addressing single metal atoms or molecules with an STM tip. Eigler et al. reported the positioning of individual Xe atoms on a Ni surface using an STM. [3] A few years later Crommie et al. used an STM to pattern Fe atoms on a Cu(111) surface to create a *'quantum corral'*. [4] Researchers from the IBM arranged and manipulated carbon monoxide molecules on a surface to create the world's smallest movie at 242 frames, called *"the boy and the atom"*, in which a character befriends an atom and dances and plays with it. [5] Such experiments not only proved that it was possible to manipulate single atoms but it was also possible to study the effect such adatoms had on the immediate environment. Various studies have reported how atoms can be arranged on a surface in the way we want to confine electrons like water in a well. A recent experiment shows that atoms could be arranged on surfaces to write information not directly with the atoms, but by influencing the substrate to confine electrons in a specific pattern, thereby making information storage electronic rather than atomic. [6]

Serious consideration of single molecule studies began when Aviram and Ratner demonstrated a rectifier like behavior using a single organic molecule confined in a nano gap. [7] In order to study a molecule's electronic properties, nanometer sized gaps, usually made of gold, were used for anchoring single molecules. Current was passed through the molecules to study various mesoscopic effects like quantized conductance, coulomb blockade etc. [8] [9] Eventually single molecules were used for demonstrating the behavior of various electronic devices like diodes and transistors for use in molecular electronics. Molecular studies using nano gaps could be useful for studying conductance related properties of single molecules due to the effect of molecule-electrode bond on the conductance. However self-assembly and intermolecular interactions are difficult to understand using this method. This could be achieved by anchoring the molecules on conducting substrates where they have a possibility to form extended and stable islands, given the appropriate conditions. A molecule can also be decorated with appropriate functional groups to steer their self-assembly in a particular pattern or direction. The self-assembled islands can then be characterized using the STM and their ability to form various covalent and non-covalent architectures, host additional molecules, confine electrons etc. could be studied in detail. Hence the STM aids in obtaining a variety of such interesting information including topographical appearance at various voltages, apparent height of adsorbates, visualizing molecular orbitals, electron distribution on surfaces, molecule-molecule interactions, spin related properties etc. that can be extracted with angstrom scale precision. The extensive information about molecules on surfaces in particular that has been documented in the past two decades is largely due to the use of STM. STM also led to the invention of other similar instruments like atomic force microscope (AFM), chemical force microscopy (CFM), kelvin probe force microscopy (KPFM), magnetic resonance force microscopy (MRFM) etc. On the whole, the role of scanning probe techniques in bringing the field of surface science to the forefront of modern nanotechnology research is unprecedented.

1.1.2 Thesis overview

In the present thesis, dense-packed molecular assemblies and molecular porous networks have been studied in detail with an STM. The assemblies and porous networks are tailored as a template for hosting other molecules and atoms. This method of using extended molecular networks as templates to confine 'guest' atoms and molecules offers certain advantages like addressing the guest species individually, weakening the substrate's influence (c.f. chapter 4) and preventing diffusion on the surface and formation of clusters. Since STM is limited in use to conducting surfaces and hence the nobel metal surfaces, Ag(111) and Cu(111) single crystals have been used for the experiments.

The molecules used in the experiments mentioned in this thesis are 1,3,5-tris(pyridin-4-ylethynyl)benzene, C_{60}, Ce(TPP)$_2$ and a Cobalt-tetraphenyl porphyrin (Co-TPP). The present thesis is arranged in the following way:

- Chapter 2 of the thesis following this introduction, describes an overview of the working principle of the STM, theoretical background of the tunneling mechanism, experimental set-up of the STM used for the results presented in the thesis and the details of the simulations and XMCD technique used in respective chapters.
- Chapter 3 of this thesis describes how the three-fold molecules is used to create porous networks that are stabilized by lateral pyridyl-pyridyl interactions and metal-organic interactions. The molecule is studied on both Ag(111) and Cu(111). On Ag(111), the molecule forms an intricate architecture stabilized by pyridyl-pyridyl bonds. When Cu atoms were deposited onto this network, the network slowly dissolves to form various architectures mediated by metal-organic and pyridyl-pyridyl interactions. The same molecule was studied on Cu(111) where the molecule uses the free Cu adatoms, that are already present in the surface, to form a flexible but robust porous network thereby exhibiting a novel type of arrangement at the nanoscale: a 2D disordered crystalline network. As a first trial, a double decker molecule (made of two porphyrins and a Ce atoms) was deposited as a candidate for confining inside the flexible Cu pores.
- Chapter 4 details a study of Ce(TPP)$_2$ double decker complexes and C_{60} fullerene molecules studied on Ag(111). The Ce(TPP)$_2$ complex is a 3D system where two free base porphyrin molecules are joined together through a cerium atom in-between thereby evidencing a sandwich-like appearance. The complex was deposited on the Ag(111) substrate to create extended dense packed arrays that serve as a platform for confining molecules. Fullerene molecules were our choice for studying the confinement capabilities of the double decker array. Three different phases of fullerene arrangement was found on Ce(TPP)$_2$ named as α, β and γ. When deposited at low temperature (phase α), the fullerene molecules were found to confine at the center of the macrocycle of top porphyrin in the double decker complex thereby forming a dyad. The porphyrins in the Ce(TPP)$_2$ also have a bowl-like structural distortion that facilitates the fullerene confinement. The

fullerenes thus confined were studied topographically and electronically. They were further manipulated mechanically to create a molecular switch. In phase β, the fullerene-double decker structure was annealed at room temperature to create highly ordered arrays of C_{60}. The ordered arrays evidenced an interesting bi-layer arrangement. The bi-layer arrangement was again annealed unto 504 K (phase γ) to create another interesting architecture where the C_{60} molecules form a square like arrangement with the double decker complexes positioned in the center of the square. This study further advances our understanding of the long studied fullerene-porphyrin supramolecular architectures.

- Chapter 5, porphyrin molecules were used as templates for atomic confinement. Fe atoms were deposited in-situ at low temperature (6 K) on a highly ordered dense packed array of cobalt-tetraphenyl porphyrin (Co-TPP) assembly grown on Ag(111). The Fe atoms were seen to be adsorbed on four distinct positions on the porphyrin macrocycle. On increasing the amount of Fe deposited on the porphyrin arrays, the Fe atoms start to cluster on the porphyrin macrocycle, thereby still maintaining a site selective adsorption on the molecule. The individual Fe atoms were mechanically switched between the aforementioned four locations on the macrocycle evidencing an atomic switch. The magnetic behavior of the Co ion in the Co-TPP molecules were studied before and after the deposition of Fe atoms with another surface analytical technique, X-ray magnetic circular dichroism (XMCD). The magnetism of the Co that was quenched on the Ag(111) sample was revived after the deposition of Fe atoms. The STM and XMCD results were complemented by DFT studies.
- The last chapter summarizes the results presented and discusses future ideas and perspectives.

2 | Experimental Methods

The focus of this thesis is on the confinement properties of organic molecules adsorbed on metallic surfaces studied with a Createc low-temperature scanning tunneling microscope (LT-STM). In recent years several STM studies have been performed on organic molecules and most of them at low temperatures and pressures. These conditions offer advantages like lowering the thermal diffusion of molecular adsorbates, lesser gaseous contaminants, increase in resolution of energy etc. [10] [11] [12] which facilitates our purpose of exploring the geometric and electronic structure of molecules in great detail. In the present chapter, an overview of the experimental set-up used for this thesis is presented and the corresponding theoretical concepts and complementary simulations are introduced.

2.1 Ultra High Vacuum (UHV) - Set-Up

UHV systems are extremely critical for studying nanoscale structures since they ensure a highly clean environment with no contamination. UHV corresponds to a pressure of less than $\sim 7 \times 10^{-9}$ mbar, which is a trillion times less than atmospheric pressure. Such low pressures are necessary since even at a pressure of 10^{-6}, a layer of gas atoms from the environment will form on the surface in $\sim$ 3 seconds. [13] This is clearly not a conducive environment for carrying out studies involving single atoms and molecules. UHV is achieved by using custom-built vacuum chambers made of materials specifically designed for this purpose. The chambers are constantly pumped by various pumps to eliminate contaminants until a desired pressure is achieved. The three most important pumps used in order to achieve UHV pressures are rotary, turbo molecular (**TM**) and the ion getter (**IG**) pumps. Each of them have their own unique function and appropriate use (see text below). The low-temperature scanning tunneling microscope (**LT-STM**) system which we have used throughout this study was constantly maintained at UHV conditions.

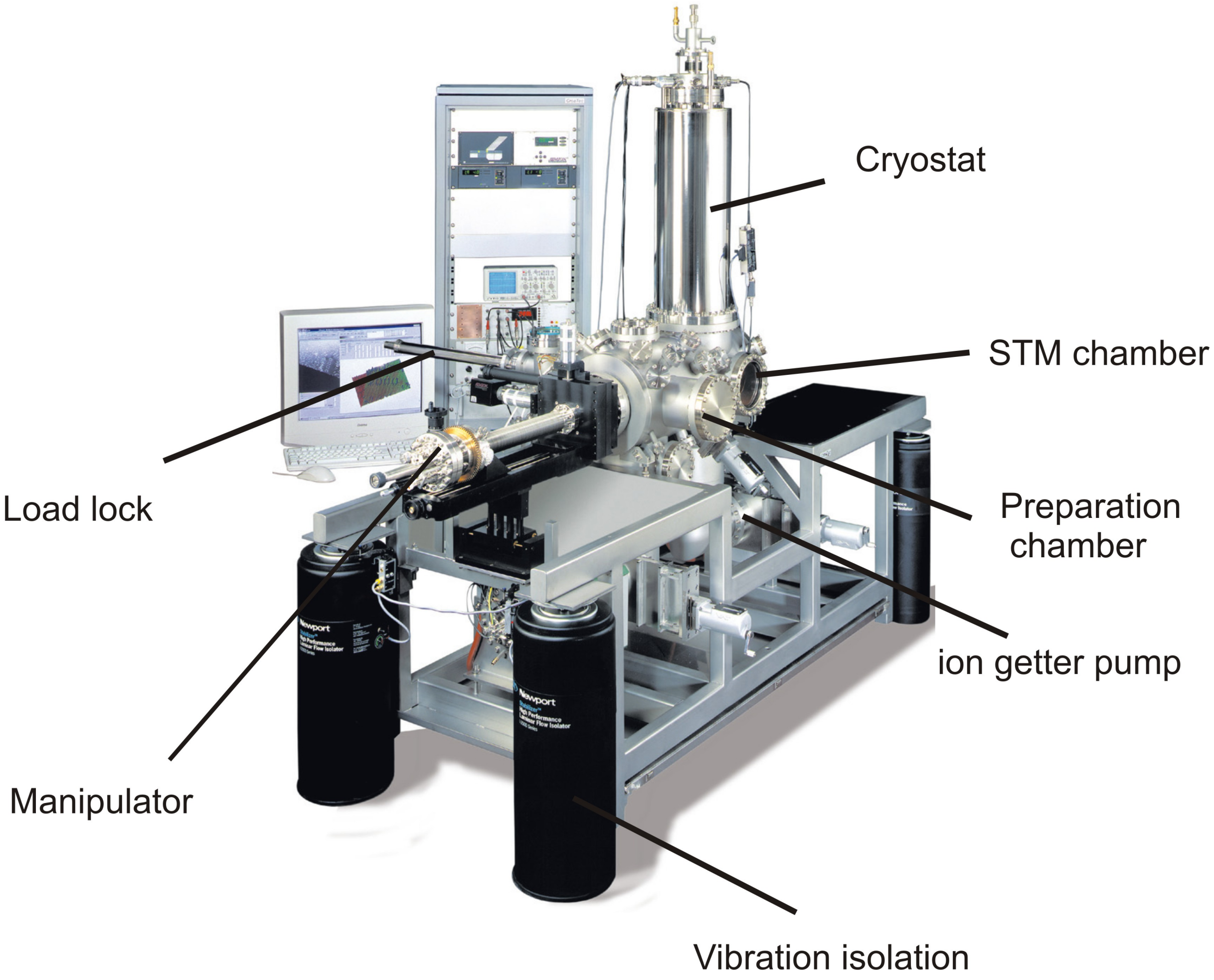

Figure 2.1: The LT-STM used for measurements presented in this thesis is shown. Below the cryostat is the STM chamber hosting the piezos and the scanner. The preparation chamber is separated from the STM chamber through a gate valve. A manipulator is attached to the preparation chamber for preparing and transferring samples. Molecules are deposited on to the sample in the preparation chamber and later transferred to the STM chamber. A load lock is used for introducing the samples in to the UHV chamber. Each chamber is pumped separately by various pumps [see text]. Adapted from [14]

2.1.1 Preparation and STM chambers

The LT-STM system consists of a preparation and an STM chamber. These two chambers are separated through a gate valve. The preparation chamber contains a Turbo Molecular (**TM**) pump, an Ion Getter (**IG**) pump, Titanium Sublimation Pump (**TSP**) and the sample preparation instruments: a sputter ion gun, a four cell molecule evaporator, metal evaporators, pressure gauges and a mass spectrometer. The STM chamber is pumped via an **IG** pump and contains the STM apparatus (see section 4) which is cooled down by cryostats to achieve the liquid helium temperatures (< 10 K) required for sample measurements. A manipulator attached to the preparation chamber is used for transferring sample to and from the STM chamber to the preparation chamber. The manipulator is equipped with feedthroughs for measuring the sample temperature, annealing and cooling the sample. A load lock is attached to the preparation chamber for introducing new samples and tips into the chamber. [figure 2.1]

2.1.2 Pumps

In the process of reaching UHV pressures, the **TM** pumps play a critical role. There are various stages of pumping carried out by the **TM** pump. The preparation chamber is pumped by a Leybold **TM** pump connected directly to the chamber. This pump is capable of pumping the chamber unto a pressure of 10^{-10} mbar. However this Leybold pump needs background pressure to start operating and this background pressure is provided by a smaller Alcatel **TM** pump which creates a pressure in the range of 10^{-6} mbar. This **TM** pump apart from creating the background pressure, is used for pumping parts of the manipulator. This smaller **TM** pump is connected to a rotary pump which is capable of creating a rough vacuum upto a range of 10^{-2} mbar. Such a pressure is needed for the turbo molecular pump to start functioning efficiently. The **TM** pumps are not connected to the STM chamber in order to minimize vibrations to which the STM operation is extremely sensitive. Since the **TM** pumps operate at very high speeds, the friction created during its operation limits its operation. This is overcome by the use of magnetic bearings which suspends the rotor during operation, eliminating the risk of contamination while minimizing noise, vibration, and maintenance requirements due to reduced 'touching' of the internals of the pump. [15] **IG** pumps are however connected to both the chambers and capable of reducing and maintaining the pressure in the 10^{-10} mbar range. **IG** pumps need a base pressure of 10^{-8} mbar to start operating smoothly. Occasionally the **TSP** is used to reduce the pressure still further when extremely clean and delicate sample preparations are needed. The **TSP** consists basically of rods of titanium connected to the base of the **IG** pumps. When high current (~ 40 A) passes through the Ti rods, clouds of Ti evaporate from the rods and sticks to the chamber walls dragging any contamination along with it. A cerium getter pump is used in addition to the **TSP**. The Ce pump works in the same manner as the **TSP** and is capable of reducing the systems base pressure to the range of 10^{-11} mbar

2.1.3 Vibration isolation

The STM measurements are extremely sensitive to external vibrations. In order to isolate the system from these vibrations, three typical damping mechanisms are employed. (*i*) The heavy chambers of the system are mounted on a frame and four strong damping legs are fixed at the corners of the frame. The legs are then filled with compressed air which lifts the frame and thereby makes the whole system float. This prevents the system from low frequency vibrations transmitted by the floor. (*ii*) In addition, the STM head that usually rests on a base plate for cooling is now suspended on four springs during measurement. This ensures that the STM is not in contact with the base plate inside the chamber thereby attenuating the possibility of noise. (*iii*) Magnetic eddy current damping is another solution to minimize vibrations. In the STM used in this thesis, three normal magnets surround the STM base plate and the magnetic field thus created acts as a damper when the STM is suspended on the springs. Eddy current dampers are a good isolation support because of its vacuum compatibility and its ability to vary the damping coefficient if necessary. [16]

2.2 Sample preparation

All the experiments relating to this thesis were performed on silver (Ag) and copper (Cu) single crystals with a (111) orientation. Ag(111) and Cu(111) has an ***fcc*** arrangement of atoms with a nearest neighbor distance of ~ 2.89 Å and ~ 2.55 Å respectively. The crystal is mounted on a sample holder containing six electrical contacts, two of which are used for measuring the temperature of the sample and two for heating the sample. All the instruments necessary for sample preparation are attached to the preparation chamber.

The first step of the cleaning procedure starts with sputtering the sample. Sputtering consists of bombarding the sample with high energy gas ions. The ions react with the top layer of the surface and removes dirt and contaminations sticking on to the surface. At higher energy, the ions could also remove the surface atoms. In our case the sample is sputtered with an energy of 800 eV with Ar^+ ions (Ar is introduced through a leak valve which is ionized in a high electric field) resulting in a sputter current of around 4 μA (measured on the sample) and a background pressure of 3×10^{-5} mbar.

Following the sputtering cycle, the sample is annealed to 725 K for 10 minutes (for both Cu and Ag) in order to achieve atomically flat and extended terraces. The annealing is carried out through an oven attached to the bottom of the sample on the sample holder.

The deposition of molecules on the sample was carried out by organic molecular beam epitaxy **(OMBE)**. The OMBE evaporator contains three quartz crucibles for hosting organic molecules and one cobalt evaporator. The crucibles are heated by resistive heating and the molecules are thoroughly degassed until their sublimation temperatures. The free base porphyrins used in the concerned experiments were deposited at 603 K, the $Ce(TPP)_2$ at 705 K, C_{60} at 673 K and Co-TPP at 625 K at a rate of 0.4, 0.6 and 1.2 monolayer/h respectively. The sample temperature was different for each particular experiment and is mentioned in the corresponding chapters. In one particular experiment, Fe atoms were deposited on cobalt tetraphenyl porphyrin (Co-TPP) molecules directly in the STM chamber and the details of this deposition is also given the respective chapter. After the deposition of molecules, the sample was cooled down through the manipulator with liquid helium ($< 150K$) and transferred to the STM chamber. There the sample is cooled down to $\sim$ 6 K (at an average rate of 1K/second) and subsequently inspected in the STM.

The tip used for scanning purposes was made of tungsten. Geometrically sharp tips are achieved by electrochemically etching tungsten wires. The tip can be inserted or taken out of the STM using a tip-holder that could be attached to the manipulator. The tip is sputtered once in a while to remove molecules and adsorbates that might be strongly attached to it during measurement.

2.3 Scanning Tunneling Microscope

2.3.1 The concept of tunneling

The phenomenon of tunneling has been an extremely fruitful consequence in the history of quantum mechanics. Tunneling is a purely quantum mechanical concept with no classical counterparts. In simple words, tunneling is described as the ability of a particle to pass through a potential barrier with a certain probability, where the

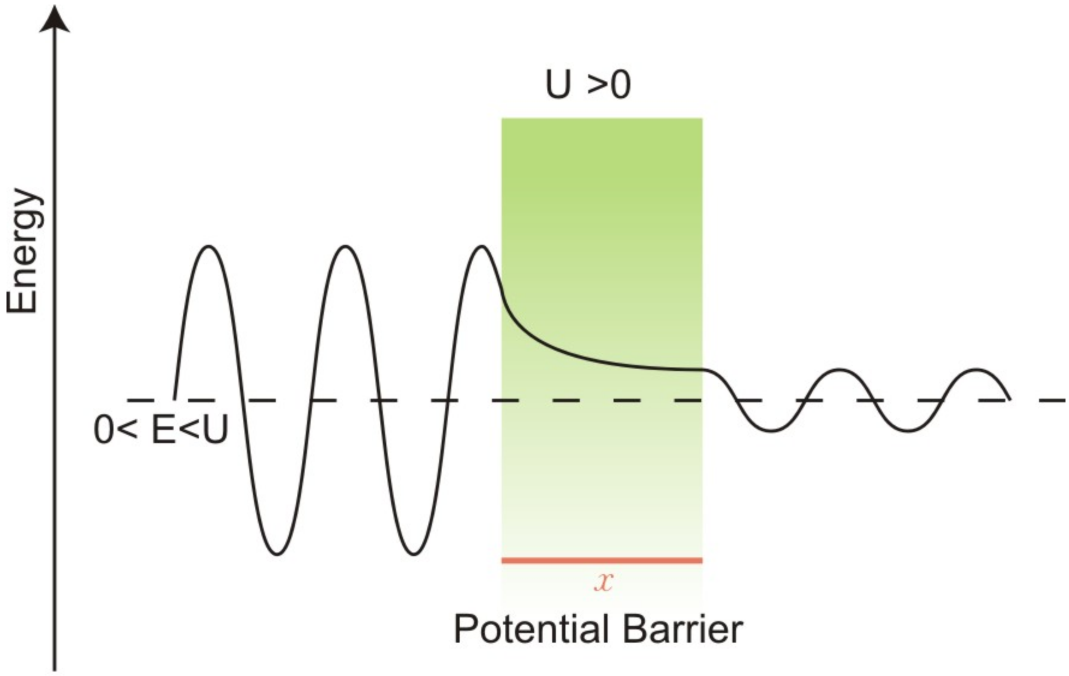

Figure 2.2: Depiction of a particle-wave tunneling through a potential barrier. According to classical mechanics the potential is considered to be impenetrable. Schrödinger's equation gives a solution to the wave function suggesting that the particle could tunnel through the barrier. The wave function exponentially decreases inside the barrier.

height of the barrier is higher than the energy of the particle. [Figure 2.2] However in classical mechanics, the particle has no possibility to cross through the barrier. The concept could be understood based on the idea of Heisenberg's uncertainty principle and the wave-particle duality of Louis de-Broglie. Schrödinger's equation is commonly used to describe the probable position and time evolution of the particle in the tunneling barrier.

Over the years, the concept of tunneling has been used to understand many fundamental processes like alpha decay, nuclear fission, chemical reaction kinetics and even certain biological processes. More recently, the theory was exploited to implement novel, ultra-precise instruments that serve as remarkable tools for the development of nanotechnology like Tunnel diodes, Josephson Junctions, Magnetic Tunnel Junctions (MTJ) ,Scanning Tunneling Microscopes (STM) etc.

Based on the tunneling effect, the Scanning Tunneling Microscope (STM) was invented in 1982 [2] and has been a milestone in the field of surface science. A year later, the (7×7) reconstruction on a Si (111) surface was imaged with atomic resolution with an STM. [17]. Over the years, STM studies have evolved to reveal hitherto unseen structural, [18] [19] electronic, [20] [21] magnetic [22] and superconducting [23] signatures of conducting surfaces and adsorbates on these surfaces with atomic resolution. In addition, the STM has been used to study various on-surface chemical reactions and induce mechanical manipulation of adsorbates, [24] molecular switches, [25] and visualize various mesoscopic phenomenon. [26] [27] [28]

An STM consists primarily of a sharp metal tip and a conducting sample and the electronics controlling the movements of the tip and bias applied to the sample. In the STM, a tunnel current is achieved by bringing the tip very close to the sample in the order of a few Angstroms separation. The tunneling current is extremely sensitive to the tip-sample distance. Initially the Fermi level of the tip and sample are aligned and the electronic states of the tip and sample overlaps and this overlap provides a channel for the tunneling current to traverse though the net current is zero. By applying a voltage between the tip and the sample, a directional tunneling current is achieved. The signs of the voltage determines the direction of the current (See below).

2.3.2 Theoretical description of the tunneling mechanism

This section gives a short introduction to the theory of tunneling that has been commonly used to understand STM functionality. There are various theories of tunneling that consider metal-barrier-metal junctions and various voltage ranges. [29] In this section, only a brief introduction to the tunneling descriptions of Bardeen and Tersoff-Hamann are mentioned.

When an electron encounters a potential barrier, classical mechanics considers the barrier impenetrable such that the electron cannot pass through it. In a quantum mechanical view, the electron can still penetrate the barrier and can even pass the barrier. There is a probability of an electron to be found inside the barrier at a given position x and this probability depends on the voltage applied to the sample. This probability can be obtained by solving the Schrödinger equation for a particle in 3D which is not easy and requires different degrees of approximation. However a first insight for finding the probable state of an electron is achieved by treating it as a simple one dimensional time-independent wave. This equation is a quantum mechanical counterpart of a classical energy equation $E_{tot} = E_{kin} + E_{pot}$.

$$-\frac{\hbar^2}{2m}\frac{d^2}{dx^2}\Psi(x) + U(x)\Psi(x) = E\Psi(x), \tag{2.1}$$

Here m is the mass of the electron, $\hbar$ is $h/2\pi$ where h is the Planck's constant, ψ

the wave function, E is the energy of the electron and U is the potential of the barrier. The above equation is a partial differential equation in x, whose solution in the barrier is given by

$$\Psi(x) = \Psi(0)e^{\pm ikx} \tag{2.2}$$

where $k = \frac{\sqrt{2m(E-U)}}{\hbar}$ is called the wave vector and $\psi(0)$ is the wave function at initial position $x = 0$.

In the case of an STM, the tunneling scenario is seen as a metal-insulator-metal junction and the probability P of finding an electron in the n^{th} state in the insulator (vacuum) region in the 1D approximation is given by

$$P_n(x) = |< \Psi(x) >|^2 \tag{2.3}$$

where x is the tip-sample distance. The tunneling probability could be written as,

$$P_n(x) = |\Psi_n(0)|^2 e^{-2\kappa x} \tag{2.4}$$

where $\kappa = \frac{\sqrt{2m(U-E)}}{\hbar} = \frac{\sqrt{2m\Phi_{eff}}}{\hbar}$. The above probability in equation 2.4 is still a finite value and hence there is a possibility to find the electron from the sample (or the tip) in the barrier. (Figure 2.3a) When a finite positive (negative) bias, V is applied to the sample, the Fermi level, E_f of the sample is shifted by the amount eV and the electrons from the occupied states of the tip (sample) tunnel into the unoccupied orbitals of the sample (tip) through the barrier. Here $(eV << \Phi_s)$ where Φ_s is the work function of the sample (Φ_t for the tip) - see Figure 2.3b,c. The barrier between the tip and the sample is modified after the application of the sample bias. Then the barrier experienced by the electron of energy E is the effective barrier height which is given by $\Phi_{eff} = \frac{\phi_t+(\phi_s+eV)}{2} - E$. The tunneling current is proportional to the number of states on the tip (sample) ψ_n within the energy interval $(E_f - eV, E_f)$ defined by the bias voltage V. Hence the tunneling current after applying the sample bias is defined as,

$$I_t \propto \sum_{E_f-eV}^{E_f} P_n(x) = \sum_{E_f-eV}^{E_f} |\Psi_n(x)|^2 = V \cdot \rho_s(x, E_f) \tag{2.5}$$

where $\rho_s(x, E_f)$ is the *LDOS* of the sample at the position x i.e. at the tip. In

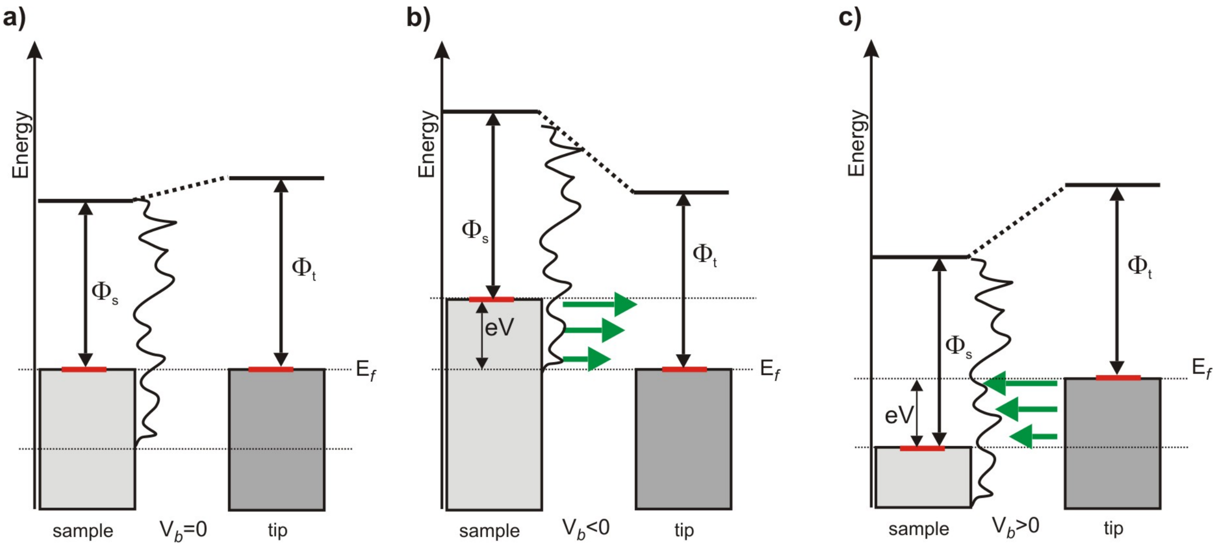

Figure 2.3: Energy diagram describing the electron tunneling through the vacuum junction (a) when no sample bias is applied, when a (b) negative and (c) positive sample bias is applied. Initially the Fermi levels (E_f) of the tip and sample are aligned (red line). But when a negative bias of energy eV is applied to the sample, the Fermi level of the sample shifts by that magnitude eV. The electrons from the occupied states of the sample (in the energy window E_f - eV) tunnel through the vacuum into the unoccupied states of the tip. The electrons are marked as green arrows and the electron close to the E_f experiences the least barrier. In the case of positive sample bias, the inverse happens: electrons from the occupied states of the tip tunnel into the unoccupied states of the sample.

addition taking into account that

$$\rho_s(x, E_f) = \rho_s(0, E_f)e^{-2\kappa x} \tag{2.6}$$

and substituting it into equation 2.5, the tunneling current can be written as

$$I_t \propto V \cdot \rho_s(0, E_f) \cdot e^{-2\kappa x} \tag{2.7}$$

where $\rho_s(0, E_f)$ is the local density of states, **LDOS** of the sample at $x = 0$ i.e. at the surface of the sample. Hence the tunneling current depends on the *LDOS* of the sample at the Fermi level. In addition the tunneling current depends exponentially and monotonically on the tip-sample distance. A change in 1 Å in the tip-sample distance changes the tunneling current by one order of magnitude. [29] Both these characteristics of the tunneling current are important in the real implementation of the STM instrument (see below).

The problem with the previous tunneling current expression is that it does not describe the rate of tunneling. To solve this problem, Bardeen, in 1961 proposed a tunneling mechanism [30] through a barrier between two metal electrodes. This model can be used to understand the mechanism of tunneling in the STM case considering certain assumptions like a low sample bias. In this formalism, the interaction between the tip and sample is sufficiently weak and could be neglected and the tunneling current can be evaluated from the eigenfunctions ψ_s and ψ_t, with eigen energies E_s and E_t of the sample and tip respectively. Herein, instead of considering the tip and sample as one quantum mechanical system, the electronic structure of the tip and the sample can be considered separately and the tunneling current is calculated from the overlap of the tails of ψ_s and ψ_t in the barrier. [31] The theory dictates that if the tunneling current in the barrier is the net effect of scattering events that transfers electrons across the barrier, no specific assumptions about the shape of the tip or sample are necessary. Hence the electronic states of the tip and sample are calculated separately and the electron transfer between the two is calculated using time-dependent perturbation theory. The tip-sample distance is assumed to be sufficiently big so that the presence of the tip is considered to be a small *perturbation* of the electronic properties of the sample. [32] Based on first order perturbation theory, the probability of the electron to tunnel from the tip to the sample is given as

$$P = \frac{2\pi}{\hbar} \sum_{S} |M_T|^2 \delta(E_t - E_s) \tag{2.8}$$

where $|M_T|$ is the tunneling matrix element and E_t and E_s are the energy eigen values of the states of the tip (ψ_t) and the sample (ψ_s). $\delta(E_t - E_s)$ is an element that ensures elastic transport between the junctions.
The tunneling matrix $|M_T|$ is expressed as

$$M_T = \frac{\hbar^2}{2m} \int_S (\Psi_s^* \nabla \Psi_t - \Psi_t^* \nabla \Psi_s) dS \tag{2.9}$$

where dS is the infinitesimal surface element in the vacuum barrier S, between the tip and the sample. From the above, the tunneling current for low voltages can be calculated [33]

$$I_t = \frac{4\pi e}{\hbar} \int_{E_f - eV}^{eV} \rho_s(E_f - eV + \epsilon) \rho_t(E_f + \epsilon) M^2 d\epsilon \tag{2.10}$$

where ϵ is an integration variable denoting that the integral is calculated as a function of energy.

In the Bardeen formalism, the tip and the sample are considered to be two independent electronic systems. However in practice, this may be not the case. The tip and the sample come close enough and that might influence each other and distort the electronic states.

The Bardeen formalism considered tunneling in a 1D case but Tersoff and Hamann in 1983 extended the previous result to arrive at a quantitative result in 3D. [34] Herein, in order to calculate a precise value for the tunneling matrix element, the tip and sample wave functions must be known. But the exact geometrical structure of the tip is difficult to know. Tersoff and Hamann assumed a model tip wave function to arrive at a more accurate answer. In this model, the wave function of the final atom on the tip is assumed to be an s-wave function. Since mainly the orbitals localized at the atomic tip plays a big role in the tunneling mechanism, the atom corresponding to this orbital is assumed to be spherical with a curvature R. With these assumptions about the geometry of the tip, Tersoff and Hamann arrived at the following expression for tunneling current, [31]

$$I_t \propto V_t e^{-2\kappa R} \rho_t(E_f) \rho_S(r_t, E_f) \tag{2.11}$$

where $\rho_S(r_t, E_f)$ is the $LDOS$ of the sample surface at the Fermi level calculated at r_t, which corresponds to the distance from the sample to the center of curvature of the tip. κ is the decay length.

It is important to realize that $\rho_S(r_t, E_f)$ includes the exponential decay of the current with distance, $\rho_S(r_t, E_f) = \rho_S(0, E_f)e^{-2\kappa r_t}$. It can be seen that the form of the tunneling current derived by the Tersoff-Hamann formalism is similar to the one derived by the Bardeen approach. Both the equations highlight that the tunneling current is proportional to the $LDOS$ of the tip and the sample and is exponentially dependent on the distance between tip and sample. The Tersoff-Hamann model is currently the widely used method to understand topographic and electronic information extracted from STM.

2.3.3 Scanning tunneling spectroscopy

In the previous section, we saw how tunneling equations are helpful in acquiring information about $LDOS$. The tunneling equations could be extended to to get information about the conducting substrate's electronic structure. This method is called scanning tunneling spectroscopy (**STS**) and can be used to identify the electronic signatures of metals and adsorbates. STS is particularly effective in detecting standing waves of confined electrons on metallic substrates, [35] and probing the occupied and unoccupied orbitals of molecular adsorbates [36] [37] etc. with high real space precision. [4]

The **STS** technique is based on the proportionality of the *differential conductance* to the *LDOS*. In order to find the differential of the tunneling current, a generalized expression of I is required. This is achieved by summing all the electronic states of the sample E_S that contribute to the tunneling current in the available energy range after applying a sample bias, written as follows:

$$I_T(V) \propto \int_0^{eV} \rho_s(E - eV + \epsilon)\rho_t(E + \epsilon)\, T(E, eV, x)dE \tag{2.12}$$

where $T(E, eV, x)$ is the transmission coefficient through the barrier. $T(E, eV, x) = e^{-2(x+R)\kappa}$ with $\kappa = \sqrt{\frac{2m\Phi_{eff}}{\hbar^2}}$ where $\Phi_{eff} = \frac{1}{2}(\Phi_s + \Phi_t + eV) - E$, the bias dependent effective barrier height. If we assume a constant density of states for the tip and a smoothly changing background signal in the case of small voltages, then the differential of the tunneling current expression could be written as, [38]

$$dI/dV \propto \rho_s(\epsilon)\rho_t(eV + \epsilon)\, T(eV, eV) \tag{2.13}$$

As we can see, the dI/dV is proportional to the LDOS of the tip and the sample. Experimentally, probing the electronic structure through STS is achieved by placing the tip fixed at a constant height (feedback loop opened) and sweeping the sample bias V at a constant rate between two voltage values, while recording the tunneling current. In this way the tip would sense the most prominent electronic state of the adsorbate as it exposes specific states at specific biases. Apart from acquiring the $I(V)$ curve separately, two methods can be employed to yield the desired dI/dV vs. V_{bias} dependence. *(i)* The $I(V_b)$ measured by the tip is then differentiated in order to get the dI/dV signal. *(ii)* The other method is applying a small sinusoidal wave modulation to the sample bias, which is then translated into a modulation of the current. In this thesis, the second method using a *lock-in* amplifier with an open feedback loop is employed due to the fast data acquisition time and increased signal to noise ratio.

The measurement of **STS** using the *lock-in* amplifier technique works in the following way: The *lock-in* amplifier compares two signals in the time domain and electronically gives the correlation in time of both signals. In the case of STS, an AC modulation denoted as $V_m \sin(\omega t)$ is sent as a reference signal to the *lock-in* and also used to modulate the bias voltage V, where V_m is the amplitude and ω is the frequency. Consequently this small modulation in the bias voltage, V_m causes also a modulation in the measured tunneling current given as $I(V_b + V_m \sin(\omega t + \phi))$. This modulated tunneling current is fed into the lock-in amplifier and correlated with the original reference signal and integrated over time and this gives the output of the lock-in. ϕ is the phase difference between the sent-in signal and the reference signal.

The relation between the modulated tunneling current and the reference signal can be understood by expanding the tunneling current in a Taylor series,

$$I(V_b+V_m \sin(\omega t+\phi)) = I(V_b)+\frac{dI}{dV}\cdot V_m \sin(\omega t+\phi)+\frac{d^2I}{dV^2}\cdot {V_m}^2 \sin^2(\omega t+\phi)+... \quad (2.14)$$

In the first order term of the above equation, we can see that the output of the lock-in is proportional to the differential conductance (dI/dV) × (reference sinusoidal signal). Hence information about the differential conductance dI/dV could be extracted from the lock-in output based on the reference signal. As the bias voltage of the sample is swept between certain distinct values and the tip is help at a constant height, the respective change in current dI/dV gives the peaks corresponding to specific orbitals of the sample, in the STS. In this thesis, the bias modulation of the reference signal was set to, $V_m = 25$ mV and frequency $\omega = 969$ Hz.

2.3.4 Modes of operation

STM operates mainly in two modes. The two modes can be exploited to obtain not only topographic measurements but also detailed information about the electronic structure of the sample. Both of these operation modes depend mainly on the feedback loop. The feedback loop is responsible for maintaining a constant tunneling current.

The feedback response in time is an important parameter in determining the spatial resolution of the sample during measurement. Typically the tunneling current is of the order of 100 pA and is measured with an acquisition bandwidth of $B \sim 1$ kHz, where B is determined as (spatial frequency of sample features) × (scanning speed). Hence for a spatial frequency of 4 atoms/nm and a scanning speed of 250 nm/s, a bandwidth of $B = 1$ KHz is sufficient to map each atom as a separate entity. [39]

- **Constant current mode:** This is the most common mode of STM operation. The images presented in this thesis were obtained by this mode of operation.

In this mode, the bias voltage and value for the tunneling current is kept fixed. The tunneling current is kept constant by the feedback system, which is *on* (feedback loop closed). The STM tip as it scans across the sample records the tunneling current. But since the current is fixed, whenever dents or adsorbates on the sample that affect the magnitude of the tunneling current are encountered, the tip retracts or approaches accordingly in order to maintain a constant current. The advantage of this method is the preservation of the tip during scanning.

- **Constant height mode:** In this mode, the tip is maintained at a constant height over the sample. To do so, the sample is set at a constant bias V_b and the feedback is *off* (feedback loop opened). As the tip scans over the sample, it experiences variations in the tunneling current. These variations are monitored to obtain a topographic image. When this mode is in use, it is important to ensure that the sample is more or less flat. Topographical variations like clusters, step edges etc might affect the movement of the tip. Hence constant current mode is usually preferred over this mode.

2.4 STM configuration

Taking into account that the tunneling current decreases monotonically and exponentially with the tip-sample distance, in order to obtain topographic images of high resolution, certain points are to be considered. We need to implement an instrument which *(i)* is able to move a tip in the x, y and z directions with sub-angstrom precision. *(ii)* is able to keep the tip-sample distance at a desired value and *(iii)* can measure small currents in the range of pA. In addition to that, the performance should produce a reasonable *signal/noise* ratio.

The technological implementation of the STM is based on piezoelectricity on the one hand and the set-up of electronics (pre-amplifier, feedback system, I/V converter, DSP etc.) on the other, as described below:

- Piezo-electric scanner
- STM electronics

2.4.1 STM Scanner

The tip movement should be sensitive and respond flexibly to the feedback electronics that controls the tip movement. This is achieved in STM by using piezo electric components to which the tip is attached. Piezo electric components by nature contract and expand depending on the electric potential applied to them. It is a core component of many modern day high precision instruments including almost all the scanning probe techniques. Piezo electric materials help to achieve nanometer scale movement of the tip by applying high potentials. The STM design used to measure the data in this thesis was developed by Gerhard Meyer at Freie Universität Berlin. [40] The design is now commercially sold by Createc GmBH. [14] The principle of operation of the STM head is shown in figure 2.4. The design is of Besocke-Beetle type [41] with some modifications. In this model, four piezo electric tubes are employed.

Each piezo tube is divided into four external sections, which provide four electrodes, while simultaneously the inner part of the tube constitutes the fifth electrode. These four outer electrodes will be responsible for applying a high voltage required to move the piezo tubes in x and y whereas the inner one controls z movement. The piezos are installed in the following arrangement:

- **Outer piezos:** Three of the four piezo tubes constitute the outer piezos and are located around the edge of a base plate (The base plate is a square of side 1 cm) forming a triangle. The top end of the three outer piezos are mounted with sapphire spheres.The sample is placed at the center of the triangle. On top of the sapphire spheres is an approach plate that is divided into three sections. Each of the piezos is confined to one of the sections and each section covers 120°. The three piezos facilitate approaching and retracting movements of a ramp positioned on top of the sapphire spheres on which the tip is held. The limit of such rotation (hence the approach limit) is defined and limited by the three sections. The outer piezo carry out a fast mechanical motion of the tip and brings it close to the sample. This is called the **coarse** approach.
- **Inner piezo:** The central or inner piezo is attached to the ramp which holds the tip. The central piezos is used in combination with the outer piezos for bringing the tip into the tunneling regime through the **fine** approach by using the Createc STM software. Once the tip is close to the sample in the tunneling regime, the central piezo is chosen for moving the tip in x,y and z directions. The central piezo can also be used in combination with the outer piezos for scanning the sample. In our case the central piezo was solely used for x,y and z directions of tip movement, while the outer piezo was used to approach the tip close to the sample until a tunneling current is achieved.

The speed of operation is limited by the resonance limits of the piezo elements. Resonance frequencies of 100 kHz for the stretching and 10 kHz for the bending for

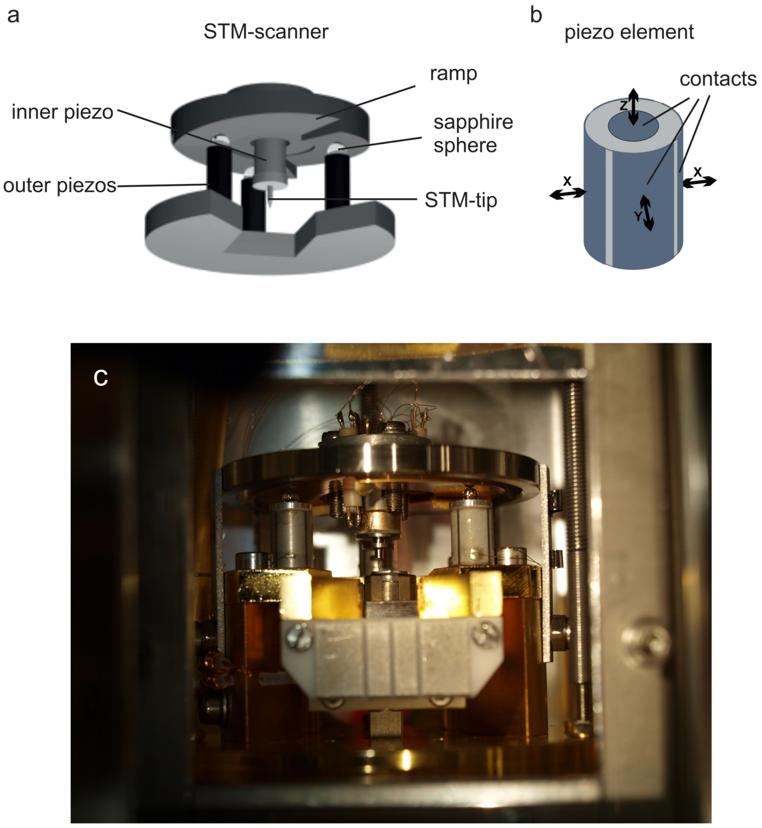

Figure 2.4: A graphic of the scanner holding the tip is shown in a). This scanner constitutes three outer piezos fixed to a base plate and one inner piezo holding the tip. In order to scan the sample, either a combination of the central and outer piezos or or only the central piezo can be used. An inner zoomed in view of the piezo element is shown in b). A photograph of inner and outer piezos mounted with a sapphire ball, the tip and the sample is seen in c). Adapted from [42]

the piezos were measured as the limits, which serves for our typical bandwidths of ~ 1 kHz. [41]

The sample rests below the base plate and in contact with a metal for cooling down to measurement temperatures.

Once the sample reaches a steady temperature of ~ 6 K, the sample is allowed to hang on springs in order to isolate it from vibrations and the measurements are performed.

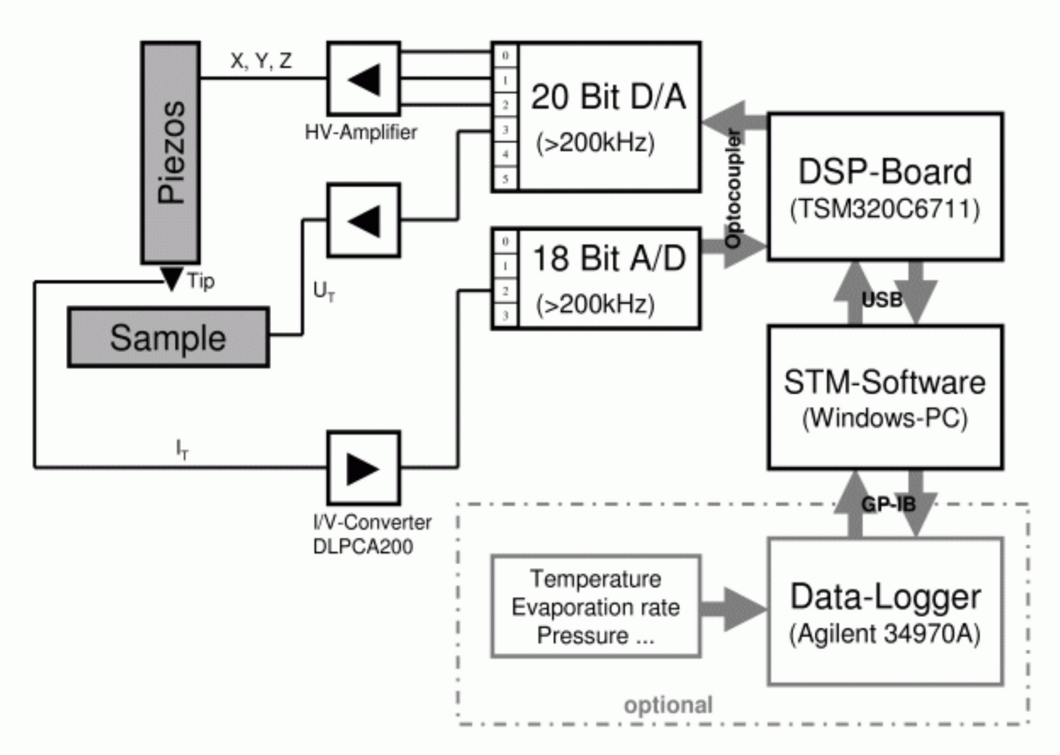

Figure 2.5: Schematic of the Createc LT-STM electronics. Voltage applied to the piezos, sample bias and tunneling current amplification are all controlled by a DSP unit through different D/A channels. The whole electronic unit is connected to the computer through a ESB 2.0 port. [14]

2.4.2 Electronic Set-Up

The operation electronics for the LT-STM are based on a digital design (figure 2.5). The digital signal processor (DSP) acts as the main mediator between the STM and the computer. The DSP controls helps in the control of the feedback loop, sample bias and the high voltages applied to move the piezos. Both the high voltage amplifier and the sample bias controller are connected to a 20 bit Digital-Analog (D/A) processor which is in turn connected to the DSP board. However the tunneling current is sensed and amplified using a separate pre-amplifier through a 18 bit D/A which is also connected to the DSP board. The gain of the pre-amplifier is manually controlled. All the DSP mechanism are controlled through the STM 3.0 software by CreaTec. The electronics is connected to the computer via a USB 2.0 link.

2.5 X-ray magnetic circular Dichroism

X-ray magnetic circular Dichroism (XMCD) measurements were performed as part of an experiment where Fe atoms were confined on the macrocycle of Co-TPP molecule. XMCD experiments helped to identify the magnetization of the Co ion in the Co-TPP molecule before and after the adsorption of Fe atoms. The measurements were preformed at the ID08 beam line at the European Synchrotron facility in Grenoble.

XMCD is an extension of the X-ray absorption spectroscopy technique. In X-ray absorption spectroscopy (XAS), when an photon is incident on a metal, the energy of the photon is absorbed by the core electrons of the metal and the electrons makes a transition to an excited state. At certain specific photon energies, sharp increases in absorption are observed. These specific energies are called *'absorption edges'*. However in the region near the absorption edges, the electrons could be excited into unoccupied bound states, producing a photoelectron. [43] The absorption occurs when the photon energy matches the ionization potential of the bound electrons at K, L, M etc. shells. The choice of the X-ray energies at these absorption edges (or the absorption coefficient σ of the element) determines the specific element being probed. [44]

XMCD is a technique where the XAS experiment is performed with certain modifications. [see Figure 2.6] In XMCD, the desired sample is placed under a uniform high magnetic field ($\sim$ 7 T) and is then irradiated with left and right circularly polarized X-rays. At specific energies of the photons, X-ray absorption occurs which is measured for both polarization at two different incident angles (0° and 70°). The difference between the absorption spectra of both polarizations gives the XMCD peak. XMCD can give information about spin and orbital magnetic moments and their magnetic anisotropies of the sample with high resolution. The technique is element specific and chemical sensitive and is an extremely useful tool in analyzing the magnetic properties of metals. [45]

2.6 Simulations

- Hyperchem 7.5 software [46] was used for building molecular models of porphyrins, C_{60} and 1,3,5 -tris (pyridine-4-ethynyl) benzene and the geometry of the molecules were optimized using a semi-empirical routine (**AM1**).
- Extended Hückel theory (**EHT**) was used to calculate the electronic structure (frontier orbitals) of free and confined fullerenes. **EHT** is a semi-empirical

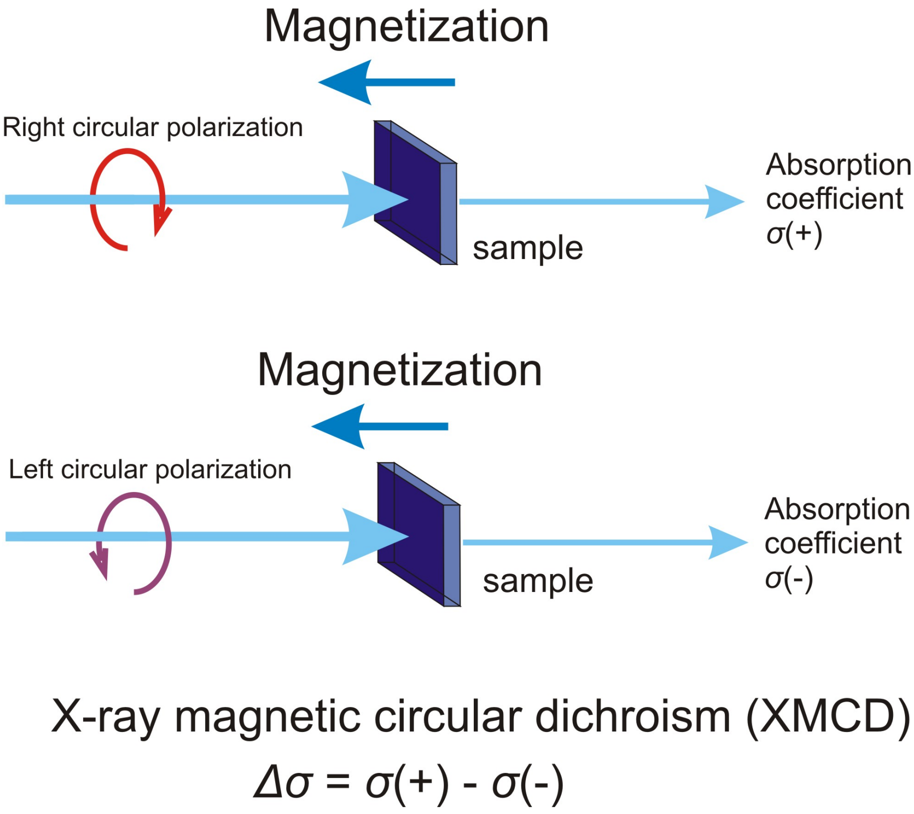

Figure 2.6: A schematic representing the working principle of the XMCD method. The sample is placed in a uniform magnetic field and left and right circularly polarized X-ray photons are incident on the sample. The XAS spectra is measured for the both polarizations. The difference between the two absorption spectra gives the magnetic signature of a species.

quantum chemistry method used for calculating the molecular orbitals that takes π and σ orbitals into consideration. [47] It can also be used for calculating the relative energies of different geometric configurations of the molecule and the total energy of the system. [48] EHT was calculated using Hyperchem 7.5 software. LUMO charge densities mimicking constant current STM images were obtained by using an STM generator software. [49]

- Density functional theory (**DFT**) was used for simulating geometrical structure, electronic and magnetic properties of various molecular systems throughout this thesis. The description of the specific **DFT** procedure is given at the respective chapters and sections. **DFT** was performed by Ari P. Seitsonen from the university of Zürich, Switzerland and Marie-Laure Bocquet from the École Normale Supérieure, Lyon, France.

- Molecular Dynamics (**MD**) simulations were carried out for calculating long-range electrostatic interaction in the assemblies of 1,3,5 -tris (pyridine-4-ethynyl) benzene molecule. Introducing the inputs from MD, the bonding and temperature stabilities of the same molecule was calculated using Monte Carlo (**MC**). Both (**MD**) and (**MC**) simulations were performed by Paweł Szabelski from Marie-Curie Sklodowska University, Lublin, Poland.

3 Metal-organic porous networks

3.1 Introduction

One of the largely explored aspects of nanoscience is the design of non-covalent self-assembled architectures by the use of organic molecules. These architectures help us (i) achieve highly ordered patterns and (ii) understand the chemical interactions that stabilize such patterns. A principle direction of such self-assembled networks has been the creation of porous networks using organic molecules. Porous networks are self-assembled architectures, where equally spaced molecules create cavities with molecular borders. Porous networks are used as a means to achieve insight into the nature of chemical bonds, create robust platforms and to direct the confinement and assembly of 'guest' species into the cavities or nodes of the porous structure. [50]

3.2 Porous networks

(i) In nature, porous networks occur in bio-organisms and such self-assembled natural porous networks are a big inspiration for designing its synthetic counterparts. [51] [52] These natural porous structures are models of perfect geometric adaptation for carrying out specific biological functions efficiently. A few examples of porous structures in nature include adenosine triphosphate (ATP) synthase for the production of ATP molecules which supplies energy to the cells in most bio-organisms, light harvesting protein complexes **LH1** and **LH2** in bacterium Rhodospirillum photometricum that are essential components of photosynthesis, [53] Alveopore corals from the great barrier reef which has a porous skeleton that helps to maintain a stable yet lightweight skeleton, [54] hexagonal structure of honeycombs and pore-forming protein like acanthaporin from acanthamoeba. [55] (figure 3.1)

(ii) Artificially created porous structures have used organic and inorganic modules and have been of tremendous interest to chemists due to their interesting applications and ability to confine guest molecules that would otherwise be difficult to isolate. [56] [57] [58] Several open porous structures have been tailored with organic and inorganic ingredients as 3D bulk crystals, [59] in solutions [60] and as 2D networks stabilized by non-covalent interactions like metal-organic, [61] hydrogen bonds, [62] van der Waals interaction [63] and dipole-dipole interactions. [64] Such networks have in turn been used to confine and study materials ranging from metal ions to molecules. [65] The final structure of the 2D porous network is determined by a very subtle balance between molecule-substrate and molecule-molecule interaction. Due to operational purposes, these networks should be robust, present sufficient periodic spatial extension between pores and adequate pore size. [66] Self assembled 2D molecular porous networks on surfaces has been studied with progressive interest after the advent of many surface analytical and scanning probe techniques especially STM. [67] [68] [69] [70] The main use of 2D porous networks on surfaces is the confinement of guest molecules and surface electrons. In some cases the guest molecules adsorbed in these porous networks have itself been shown to modify the host network or develop 3D architectures. [71] Therefore bottom-up fabrication of porous networks have reached a level of maturity where growth, stability and dimensions of these networks can be controlled to a high level of precision.

In the present chapter, a tripod molecule equipped with terminal pyridyl groups is studied on Ag(111) and Cu(111). Metal-organic porous networks based on the simultaneous expression of metal-organic bonds and pyridyl-pyridyl interactions are presented on Ag and Cu substrates.

- On Ag(111), the molecule evidences a highly regular porous network stabilized by pyridyl-pyridyl interactions when directly sublimated onto the substrate. On deposition of Cu adatoms, the molecules form various metal-organic coordination networks (**MOCN**) depending on the Cu adaptors density: a scenario in which an interplay between molecular bonds of different nature is visualized.
- Even though the molecule appears rigid on the Ag(111) surface, the situation is different on Cu(111), where the molecule evidences a flexibility which results in the formation of 2D short-range disordered crystalline networks. Extended phases of these disordered crystalline domains form as a consequence of a fine interplay between metal-organic and $N \cdots H$ non-covalent interaction. The main aspects of the results on Cu(111) were summarized by our group in a recent publication. [73]

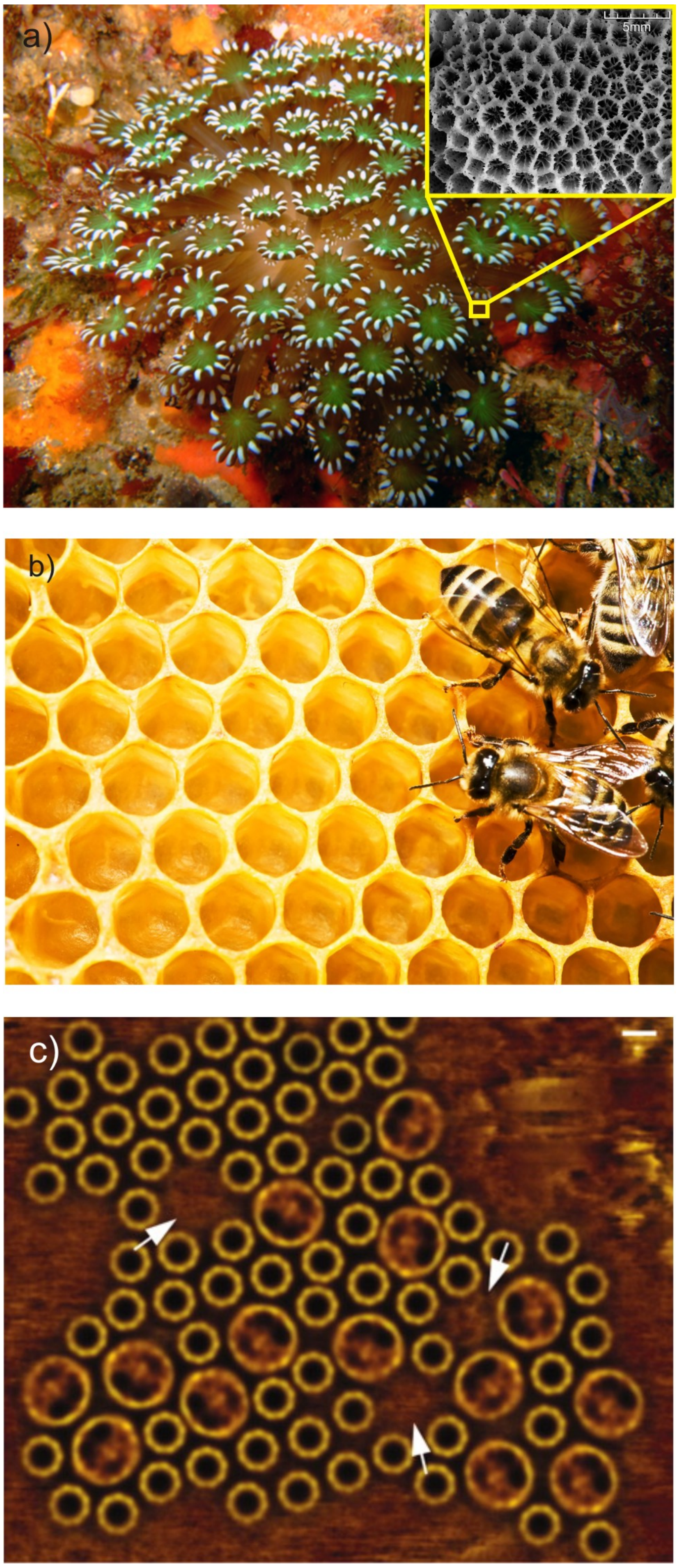

Figure 3.1: **Porous networks in nature:**
a) Photograph of coral *Alveopora Japonica*. The coral is characteristic of having a extremely light mass due to an intricately designed porous skeleton. The inset shows a zoom-in of the skeleton. [54]
b) A honeycomb showing perfectly symmetrical and ordered hexagonal pores. The combs are made of wax and are geometrically stable. The hexagon shaped pores consume less wax than circular ones and gives maximum storing space per unit volume. [72]
c) Photosynthetic apparatus in the bacterium *Rhodospirillum photometricum*. The larger circles are identified as **LH1** and the smaller ones as **LH2**, both of which are proteins that harvest the light and convert it into electro-chemical potential that is used by the bacteria. [53]

3.3 2D molecular porous network on Ag(111)

Here, we are interested in the formation of regular porous networks based on competing interactions, i.e., binding forces of similar strength. To this aim, we exploit the supramolecular linking characteristics of a tripod molecule equipped with three pyridyl functional groups (cf. module 1 in Figure 3.2a).

The threefold symmetric molecule used is referred to as molecule **1**. Molecule **1**: 1,3,5-tris(pyridin-4-ylethynyl)benzene, consists of three pyridyl groups connected to a central aryl ring through alkyne moieties (cf. Figure 3.2a). The functional terminal groups are programmed to steer simultaneously metal-organic interactions through pyridyl-metal-pyridyl coordination motifs, [74] [75] [76] [77] [78] [79] [80] together with lateral pyridyl-pyridyl links. [73]

3.3.1 Results and discussion

The deposition of submonolayer coverage of **1** on Ag(111) held at 350 K results in the formation of extended 2D molecular hexagonal porous networks (cf. Figure 3.2b), to be named phase α, with an average pore to pore distance of 20 Å ± 1 Å and a circular pore size of ~ 35 Å^2, as estimated from a careful inspection of the cavities in high resolution STM images. It is likely that an increase in the molecular coverage to saturation promotes the formation of a perfect porous molecular monolayer.

High resolution STM data (cf. Figure 3.2c) allow us to discern individual molecules with submolecular features. Each molecule is characterized by four lobes, which correspond to the central aryl and the three peripheral pyridyl groups, respectively. Remarkably, the molecular appearance in the STM images preserve a strict 3-fold symmetry, i.e., the apparent opening angles between pyridin-4-ylethynyl functions is 120°. Thus, the intrinsic flexibility attributed to the ylethynyl moietie, and visualized on Cu(111), as detailed in the next section. In addition, we observe two different molecular orientations related by a 60° rotation. As clearly depicted experimentally in Figure 3.2c and by the corresponding atomistic model in Figure 3.2d, the network is stabilized by just one type of recognition motif between molecules: an interaction of one pyridyl group with an adjacent pyridyl ring (to be called lateral pyridyl-pyridyl interaction), following a design in which each molecule is connected to three opposite oriented neighbors via two lateral pyridyl-pyridyl bonds, resulting in six pyridyl-pyridyl bonds per molecule. In analogy to the deposition of 1 on Cu(111), we assign this recognition motif to a non-covalent interaction with a characteristic N-H length of 1.8 ± 0.5 Å similar to the values encountered on Cu(111) [73] and at the solid-liquid interface. [81] Based on this recognition motif, we observe that

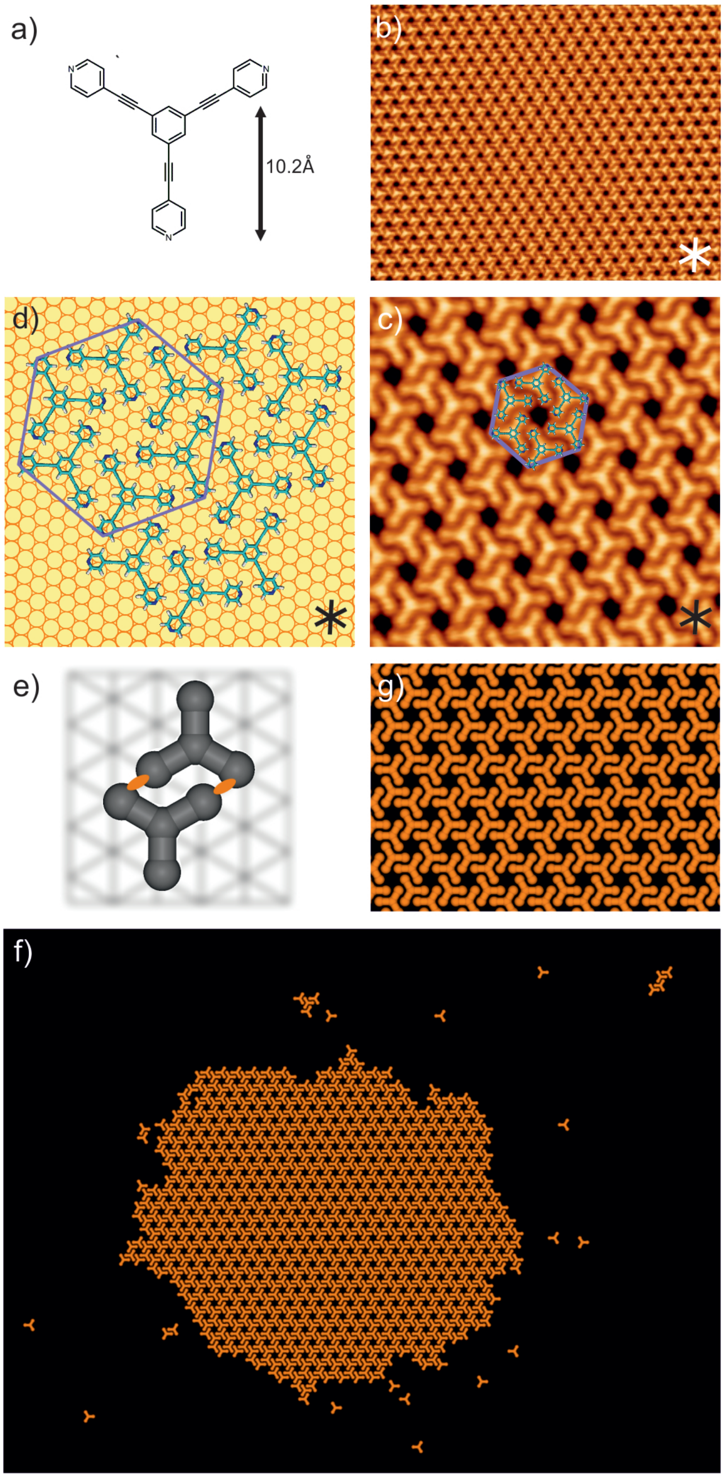

Figure 3.2: 2D hexagonal molecular porous network obtained by the deposition of molecule **1** on Ag(111). a) Scheme of compound **1**. b) Large-scale STM image displaying the porous assembly. c) Submolecular resolution STM image of a zoom-in region of b) exhibiting the three-fold appearance of the compound on the surface. d) Atomistic model of the assembly. The Rosetta pore described in the text is highlighted by a violet hexagon. The closed-packed directions of silver are depicted by white or black crosses. Image size: b) 403 Å × 325 Å and c) 129 Å × 129 Å. Tunneling parameters: b-c) I = 0.2 nA, $V_b = -1.7$ V. e) Adsorbed configuration of a pair of model molecules **1** used in the MC simulations, leading to development of the phase α. The N···H interactions stabilizing the configuration are shown in orange. f) Snapshot of the equilibrium configuration of 1000 molecules **1** obtained from the MC simulations in which only the directional N··· H interactions from e) were assumed. g) Magnified fragment of e).

each pore is made of six molecules, exhibiting a global Rosetta-like aspect. On the other hand, and within the experimental error, the assembly is commensurate with respect to the Ag(111) substrate. We tentatively propose a molecular adsorption site geometry in which the compound is placed with an aryle on top of a hollow site and the remaining pyridyl substituents are located on top positions. [82]

The supramolecular network features organizational chirality and accordingly two mirror-symmetric domains of the hexagonal porous network have been observed, designated α_1 and α_2 - network. Hereby, the unit cell vectors of the supramolecular hexagonal porous pattern form an angle of $-23°$ for chirality α_1 and of $+23°$ for chirality α_2 with respect to the close-packed directions of Ag(111)

In order to get a deeper insight into the stability and the porosity of phase α we have performed Molecular Dynamics simulations assuming islands of six molecules under periodic boundary conditions on Ag(111). We observe that a configuration of six linkers arranged like a Rosetta pore is stable, presenting six $N \cdots H$ interactions with a N-H length of 3.7 Å . In addition, two different close-packed assemblies of the modules turn out to be not stable. Finally, a simulation employing tripod modules equipped with phenyl substituents instead of pyridyls is not able to originate a Rosetta pore. Altogether, these results prove that the directional lateral pyridyl-pyridyl interaction is responsible both of the stability and porosity of phase α. This conclusion was also confirmed by separate lattice gas Monte Carlo simulations in which large assemblies of molecule 1 were modelled assuming the dominant role of the directional $N \cdots H$ interaction in the formation of the Rosetta motif (cf. Figures 3.2e-g).

In order to obtain deeper insight [83] into the stability and the porosity of phase α, we have performed Molecular Dynamics (MD) simulations assuming islands of six molecules under periodic boundary conditions on Ag(111). A configuration of six linkers arranged like a rosetta pore is stable at 100 K, presenting twelve $N \cdots H$ associations. Importantly, two different close-packed assemblies of the modules turn out to be unstable. Finally, a simulation employing tripod modules equipped with phenyl substituents instead of pyridyl termini is not able to create a rosetta-like pore. Altogether, these results prove that the lateral directional non-covalent interactions are responsible both for the stability and the porosity of phase α. To further corroborate this conclusion, we have performed separate lattice gas Monte Carlo (MC) simulations (cf. Figures 3.2e-g), which are parameterized according to the former MD output to account for the dominant contribution of the lateral pyridyl-pyridyl interactions in the stabilization of the rosetta motif, i.e., only the interactions marked in orange in the configuration from (cf. Figure 3.2e) are considered. As a result, large assemblies of the molecule are modeled confirming the dominant role of the lateral pyridyl-pyridyl contacts in the formation of phase α.

3.3.2 Polymorphism via competing interactions at submonolayer coverage

The deposition of small amounts of Cu atoms on a previously prepared submonolayer α-network changes dramatically the self-assembly scenario. Up to three new phases appear, coexisting with phase α, to be named phase β, phase γ and phase δ. As we will describe below, phase β and phase γ are based on competing lateral pyridyl-pyridyl interactions and pyridyl-Cu-pyridyl bonds, whereas phase δ is a fully metallated phase stabilized by pure pyridyl-Cu-pyridyl links. Remarkably, the deposition of enough Cu atoms, verified by the presence of Cu clusters on the steps, dissolve phase α into different patches of phase β, phase γ and phase δ. In any scenario, the presence of phase β is majority, highlighting its higher stability.

Figure 3.3a,b,c displays a long range STM image, a high resolution STM image and an atomistic model of phase β. The assembly is a complex porous network made of four types of pores: a small quasi-circular pore of ~ 20 Å^2 (displayed in violet in Figure 3.3a) and three different oriented pores, related by a 60° rotation, presenting the same size and distorted-hexagonal shape of ~ 200 Å^2 (colored in white, green and red, respectively in Figure 2a). The small pores are arranged on the surface following a hexagonal pattern, separated by 51 ± 0.5 Å. The unit cell vectors of this hexagonal pattern form an angle of 23° with respect to the closed-packed directions of the Ag(111). On the other hand, the arrangement of the distorted-hexagonal pores follows a Kagomé assembly, as depicted by pink lines in Figure 3.3a.

A zoom in this image (cf. Figure 3.3b) displays the molecules with submolecular resolution. Like in phase α, the molecular species are visualized as a tripod building block, exhibiting perfect three-fold symmetry, made of four lobes, corresponding to the central aryl and the peripheral pyridyl groups, respectively. In addition, we distinguish four different molecular orientations.

The stability of the network is provided by two different recognition motifs (cf. Figure 3.3c): **i)** a head to head orientation between two neighbor pyridyl groups with a projected N-Cu distance of 2.2 ± 0.5 Å , and ii) a lateral interaction of one pyridyl group with an adjacent pyridyl ring. In analogy with phase α, motif **ii)** is assigned to a noncovalent interaction with an average projected N-H length of 1.8 ± 0.5 Å. In addition, based on the assembly of species 1 on Cu(111) [73] we assign motif **i)** to a non-straight (dihedral angle of $\sim 15°$) pyridyl-Cu-pyridyl metal-organic interaction, in which the mediating Cu adatom is not resolved, [73] [74] [76] [77] presumably due to an electronic effect. [84] Remarkably, in any phase of this study exhibiting a Cu-pyridyl interaction we have detected an increase of the apparent height of the molecular moieties involved in the Cu-pyridyl bond in comparison with other moieties establishing lateral pyridyl-pyridyl interations, which reinforces our assumption of the formation of a metal-organic bond. In summary, the network is stabilized by a competition between non-covalent interactions of different nature, which is expressed in a complex hierarchic organization: Six molecules are forming a Rosetta-like structure, identical to the Rosetta found in phase α, via six lateral pyridyl-pyridyl interactions per molecule. This Rosetta-like tecton gives rise to the small circular pore. Simultaneously, the Rosettas are connected with each other following a hexagonal design by establishing pyridyl-Cu-pyridyl bonds with two different oriented molecular species. The remaining surface voids originate the distorted-hexagonal pores, to be named B pores. In summary, phase β is a hierarchic porous network exhibiting two levels of hierarchy: a first level to create the Rosetta tecton involving lateral pyridyl-pyridyl interactions and a second level to join the Rosettas together based on metal-organic coordination. Overall, the local Cu:molecule stoichiometric ratio is 0.75 : 1. In principle, the pyridyl-pyridyl interaction could be considered weaker than the pyridyl-Cu-pyridyl counterpart. However, as a whole, the Rosetta tecton is robust enough to be part of the first level of chirality. This is unprecedented in hierarchic assemblies involving a level of metal-organic coordination, since in these cases the metal-organic bonds form part of the first level of assembly, whereas the remaining (and typically weaker) forces intervene in the next levels of hierarchy. [85]

Due to the presence of the Rosetta, the self-assembly of phase β is exhibited in the form of two mirror-symmetric domains, non- coexisting in the same island, to be named β-network and β'-network (cf. Figure 3.3d). Hereby, the unit cell vectors describing the hexagonal arrangement of the Rosettas form an angle of $+23°$ for chirality β and of $-23°$ for chirality β' with respect to the closed-packed directions of Ag(111).

Figure 3.4a displays a long-range STM image of phase γ, which is visualized as a 2D molecular porous assembly based on alternating rows of two different kind of pores. The small pores present a mean area of 200 $Å^2$, forming a row with an interpore distance of 31 ± 0.5 Å. Simultaneously, the bigger voids exhibit a size of 350 $Å^2$ and a separation between pores of 31 ± 0.5 Å. High resolution STM data in Figure 3.4b and its corresponding tentative model in Figure 3.4c reveal that phase γ exhibits striking similarities to phase β regarding its building motifs: **i)** The same molecular aspect and four different molecular orientations identical to those of phase β; **ii)** Phase γ is also stabilized by a simultaneous expression of a lateral pyridyl-

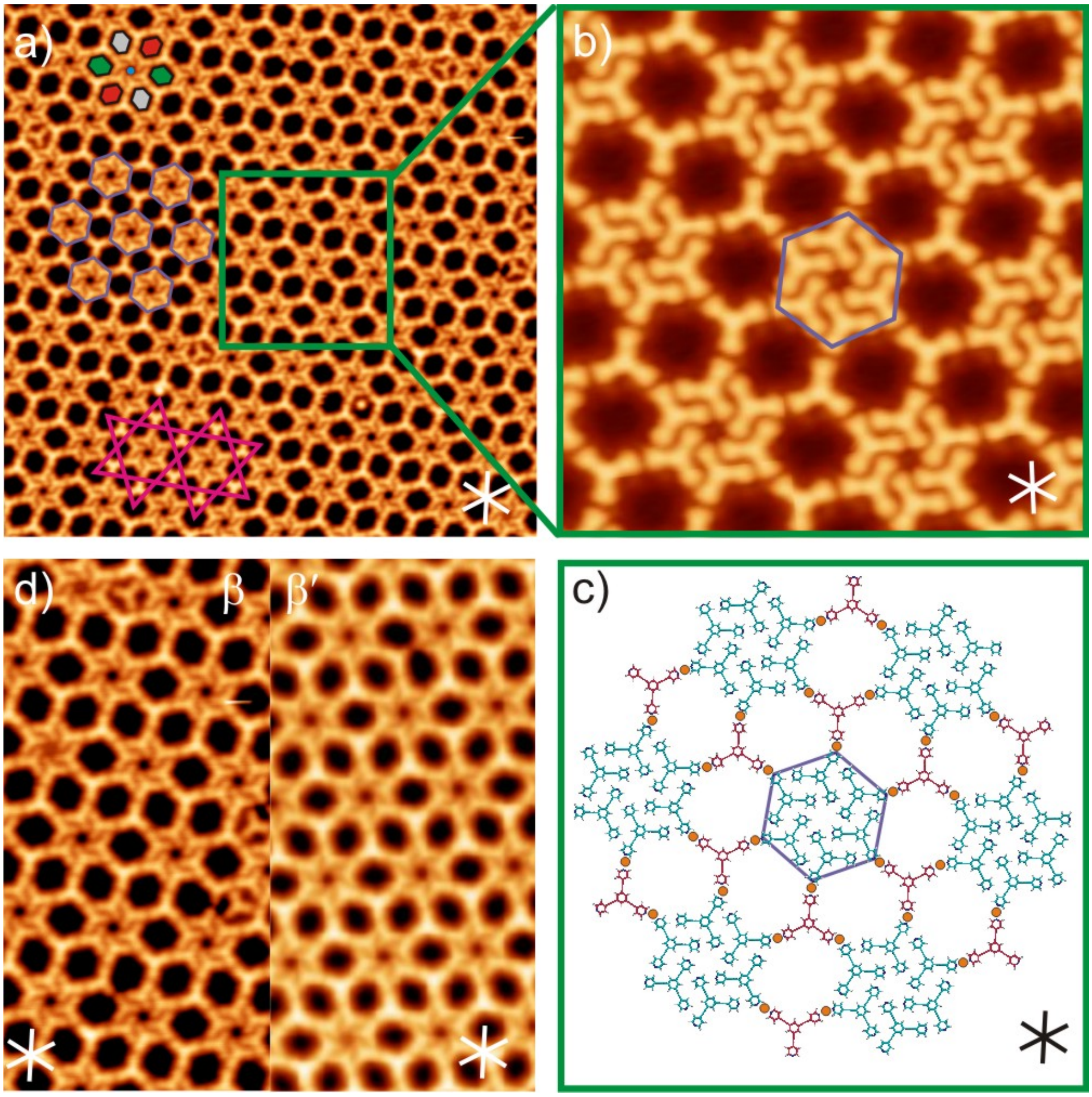

Figure 3.3: Phase β: A 2D hierarchic molecular porous assembly based on competing interactions obtained by the deposition of **1** and Cu atoms on Ag(111), for a local $0.75:1$ (Cu:molecule) stoichoimetric ratio. a) Large scale STM image of the porous assembly. The Rosetta pores are highlighted by a light violet hexagonal contour. In the top right part of the image, the different oriented pores B are filled in with colors white, red and green, respectively, whereas the Rosetta pore is filled in with blue. The assembly of pores B in positions of a Kagomé lattice is displayed by the pink lines. b) Zoom in of image a) exhibiting submolecular resolution features of the assembly. c) Atomistic model of b) displaying two types of recognition motifs: a lateral pyridyl-pyridyl interaction and a non-straight two-fold pyridyl-Cu-pyridyl bond. d) High resolution STM images showing the organizational chirality displayed by phase β, respectively termed β and β'. The closed-packed directions of silver are depicted by white or black crosses. Image size: a) 443 Å × 443 Å b) 140 Å × 140 Å and d) 144 Å × 287 Å each image. Tunneling parameters: $I = 0.2$ nA, $V_b = -0.7$ V.

pyridyl interaction and a pyridyl-Cu-pyridyl metal-organic coordination, exhibiting the same bond distances. **iii)** The small pore is identical to pore B found in phase β (depending on chirality, see below), whereas the big void is novel and, thus, will be named pore C. There are not traces of Rosetta pores in this phase. Thus, the differences between phase γ and β arise from different organizational routes, which employ for phase β a local 1.25 : 1 (Cu:molecule) stoichiometric ratio, higher than in the γ case. Hereby, two different oriented molecules (displayed in green in Figure 3.4c) are involved in a simultaneous expression of interactions, a lateral pyridyl-pyridyl link and a non-straight pyridyl-Cu-pyridyl contact (dihedral angle of $\sim 15°$), whereas the other two different oriented molecules are just establishing straight pyridyl-Cu-pyridyl contacts (depicted in pink in Figure 3.4c).

Regarding the self-assembly of phase γ, an statistical analysis of long-range STM images exhibits the presence of three organizational domains, to be named domain γ_1, γ_2 and γ_3, respectively rotated by 60°. As depicted in Figure 3.4a-c, domain γ_1 is forming an angle of 11° with respect to the closed-packed directions of the Ag(111). In addition, due to the presence of the lateral pyridyl-pyridyl interactions, which express chirality on the surface, phase γ displays the corresponding three organizational chiral domains, to be named γ_1', γ_2' and γ_3' (cf. Figure 3.3d for a comparison of the two mirror-symmetric domains γ_1 and γ_1').

Figure 3.5a shows a long-range STM image of phase δ, which is a 2D molecular porous network, exhibiting distorted hexagonal pores with a pore size of 500 Å^2 and arranged in a hexagonal fashion with an interpore distance of 32.0 ± 1 Å. High resolution STM images and a tentative atomistic model (cf. Figure 3.5b,c) decipher the building protocol stabilizing the network: two different oriented molecules are involved in a pure pyridyl-Cu-pyridyl interaction following a stoichiometry (Cu:molecule) = 1.5 : 1. Remarkably, like in phases β and γ, the metal-organic bond presents the same bond distance and it is not straight (dihedral angle of $\sim 15°$), which, together with the assembly protocol, gives rise to a distorted hexagonal appearance of the pore, to be named pore D. Since there are no traces of the lateral pyridyl-pyridyl interaction, phase δ can be considered as a fully Cu-metalated network

Concerning the organizational self-assembly, phase δ presents two orientational domains related by a 36° rotation. Figure 3.5a-c displays domain 1, in which the unit cell vectors describing the hexagonal assembly of the pores form an angle of $-13°$ with respect to the closed-packed directions of Ag(111).

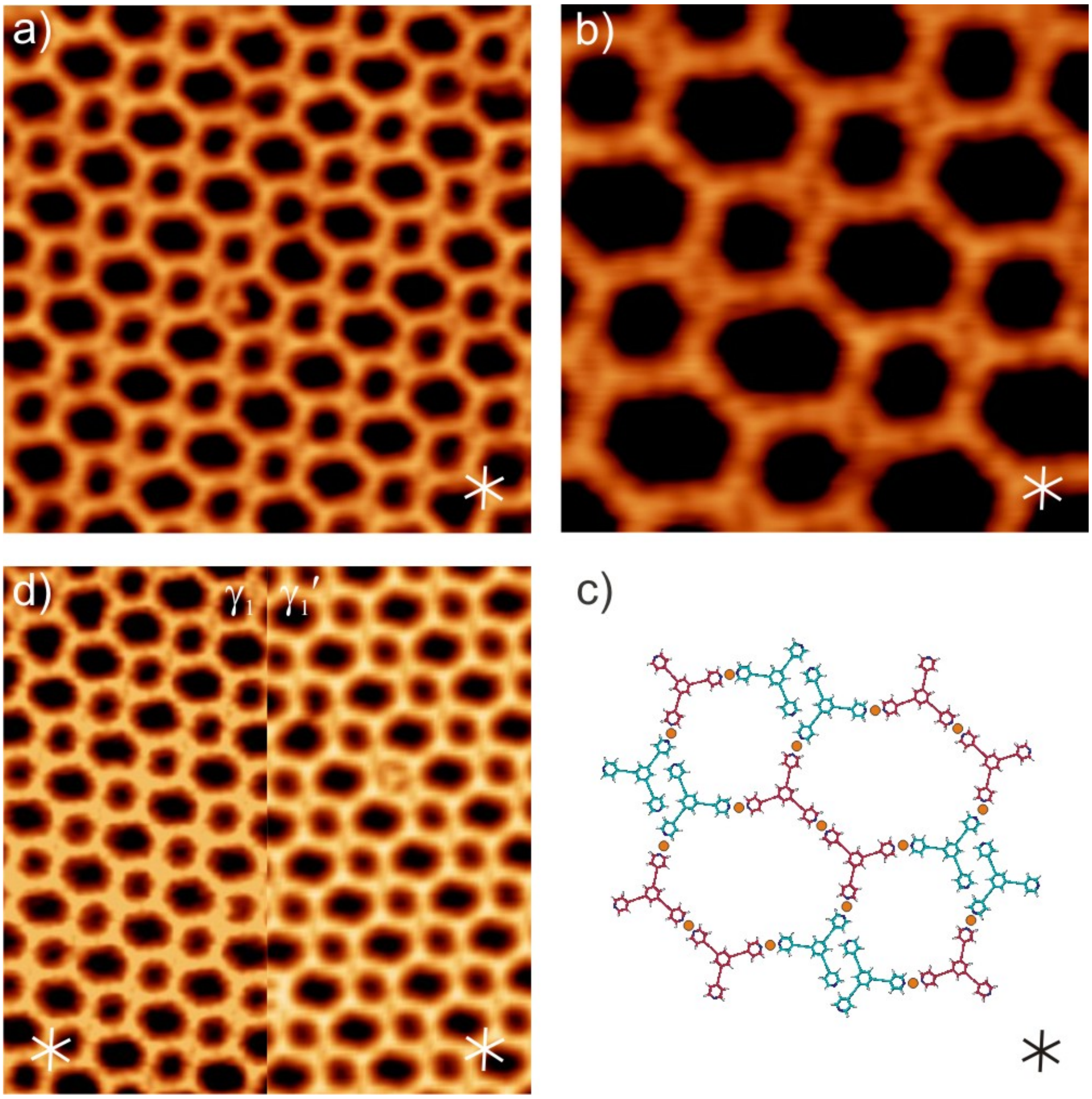

Figure 3.4: Phase γ: A 2D molecular porous assembly based on competing interactions obtained by the deposition of 1 and Cu atoms on Ag(111), for a local 1.25 : 1 (Cu:molecule) stoichoimetric ratio. a) Large-scale STM image displaying the alternating rows of pores. b) High resolution STM image of a zoom-in region of a) exhibiting submolecular resolution. c) Atomistic model of the assembly revealing the simultaneous expression of lateral pyridyl-pyridyl and pyridyl-Cu-pyridyl interactions. d) STM images comparing two chiral-symmetric domains. The closed-packed directions of silver are depicted by white or black crosses. Image size: a) 251 Å × 251 Å b) 111 Å × 111 Å and d) 300 Å × 150 Å each image. Tunneling parameters: a) $I = 0.1$ nA, $V_b = -0.7$ V; b) $I = 0.2$ nA, $V_b = -1$ V; d) $I = 0.1$ nA, $V_b = -1$ V.

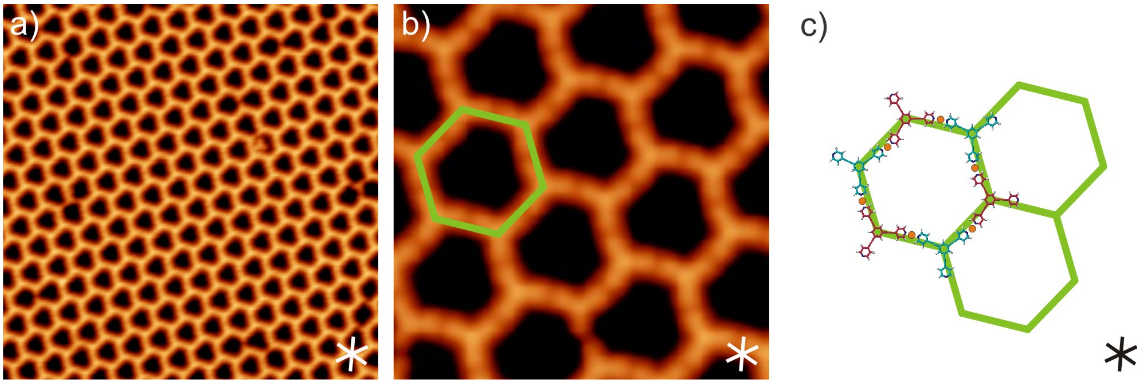

Figure 3.5: A 2D molecular porous network based on pyridyl-Cu-pyridyl interactions obtained by the deposition of **1** and Cu adatoms on Ag(111), presenting a local stoichiometry (Cu:molecule) = 1.5 : 1. a) Large scale STM images of the two domains of the 2D porous assembly. b) High resolution STM image of a) displaying submolecular recognition and exhibiting the head to head pyridyl-Cu-pyridyl recognition motif stabilizing the network. c) Schematic model of image b). The closed-packed directions of silver are depicted by white or black crosses. Image size: a) 443 Å× 443 Å, b) 221 Å× 221 Å. Tunneling parameters: a) $I = 0.2$ nA, $V_b = -1$ V; b) $I = 0.2$ nA, $V_b = -0.6$ V.

3.3.3 Self-assembly modified by molecular pressure:

The coexistence of phases α, β, γ and δ at submonolayer coverage is due to a very subtle balance between molecule-substrate interactions and the simultaneous expression of lateral pyridyl-pyridyl and metal-organic bonds. Clearly, from phase α, to phase γ, there is an increase in the porosity of the networks. Thus, a rational way to promote a better homogeneity of the molecular coverage of Ag(111), i.e., to select a phase, is based on the intrinsic in-plane compression pressure built up by the molecules confined on the surface, which, in principle, could enhance phase β. [79]

For a molecular coverage of 0.8 ML, after the dosage of Cu adatoms, we observe the coexistence of phases α (non coordinated phase) and β, whereas phases γ and δ are not detected.

Surprisingly, for a molecular coverage close to the monolayer (above 0.9 ML), followed by Cu deposition, a new phase appears, termed phase ϵ, which just coexists with a minority of phase α. A long-range STM image, a high resolution STM image and a tentative atomistic model of this phase are depicted in Figure 3.6. Remarkably, we observe the formation of a 2D hierarchic porous assembly exhibiting two levels of hierarchy. The first one corresponds to the Rosetta tecton, previously described above and stabilized by lateral pyridyl-pyridyl interactions. Secondly, these Rosettas are positioned on the surface in a hexagonal lattice, being joined together by three-fold pyridyl-Cu bonds. As a result, phase ϵ, like its phase β and

γ counterparts, is based on a simultaneous expression of interactions, though in this case the metal-organic bond is three-fold, whereas for phases β and γ is two-fold. A comparison in Figure 3.6a between phase γ and phase ϵ, reveals that the same two molecular orientations are involved in the formation of both phases. In particular, phase ϵ follows a design pattern in which each molecular module establishes four lateral pyridyl-pyridyl interactions and one pyridyl-Cu bond, presenting a 1 : 3 (Cu:molecule) stoichoimetric ratio. Within the experimental error, the lateral pyridyl-pyridyl interactions presents a identical $N \cdots H$ distance to that of phase α, whereas the N-Cu bond distance is of 1.9 ± 0.5 Å. Interestingly, as a result of the hierarchic design, phase ϵ exhibits the Rosetta pores in an hexagonal lattice, like phase α, but with a different interpore distance and orientation with respect to the substrate. Thus, the molecular pressure together with the simultaneous expression of interactions hints a way to tune the porosity of molecular networks. In particular, for phase ϵ the interpore distance between the Rosetta tectons is of 33.5 ± 0.5 Å, whereas the unit cell vector of their hexagonal assembly forms an angle of $+18°$ with respect to the closed-packed directions of Ag(111).

On the other hand, due to the presence of the Rosetta tecton, phase ϵ should exhibit two mirror-symmetric domains on the surface. However, we could only detect the formation of domains of one type of chirality, i.e., domains ϵ, but not ϵ'.

We have tried to estimate the binding energy per molecule of each phase, taking into account recent results, which report a binding energy of 0.101 eV [86] for a pyridyl-hydrogen interaction and of 0.2 eV/molecule [87] for a Cu-pyridyl bond. Our calculations show a preference for the fully metalated phase, which is not consistent with a simultaneous expression of a lateral pyridyl-pyridyl interaction and a Cu-pyridyl interaction, as experimentally visualized by the coexistence of different phases. These results suggest that in order to have a competition between interactions the pyridyl-hydrogen binding energy could be closer to the Cu-pyridyl value in our scenario than in the previous reports.

3.3.4 Simulations:

The Molecular Dynamics (**MD**) and Monte Carlo (**MC**) simulations were carried out by Pawel Szabelski from the Maria-Curie Sklodowska University, Lublin, Poland.

All Molecular Dynamics (**MD**) simulations were performed with the *Gromacs* **4.5.5** Software Package. [88] [89] The calculations were carried out in a canonical (**NVT**) ensemble at 100 K using the $Nos - Hover$ thermostat. The interaction parameters

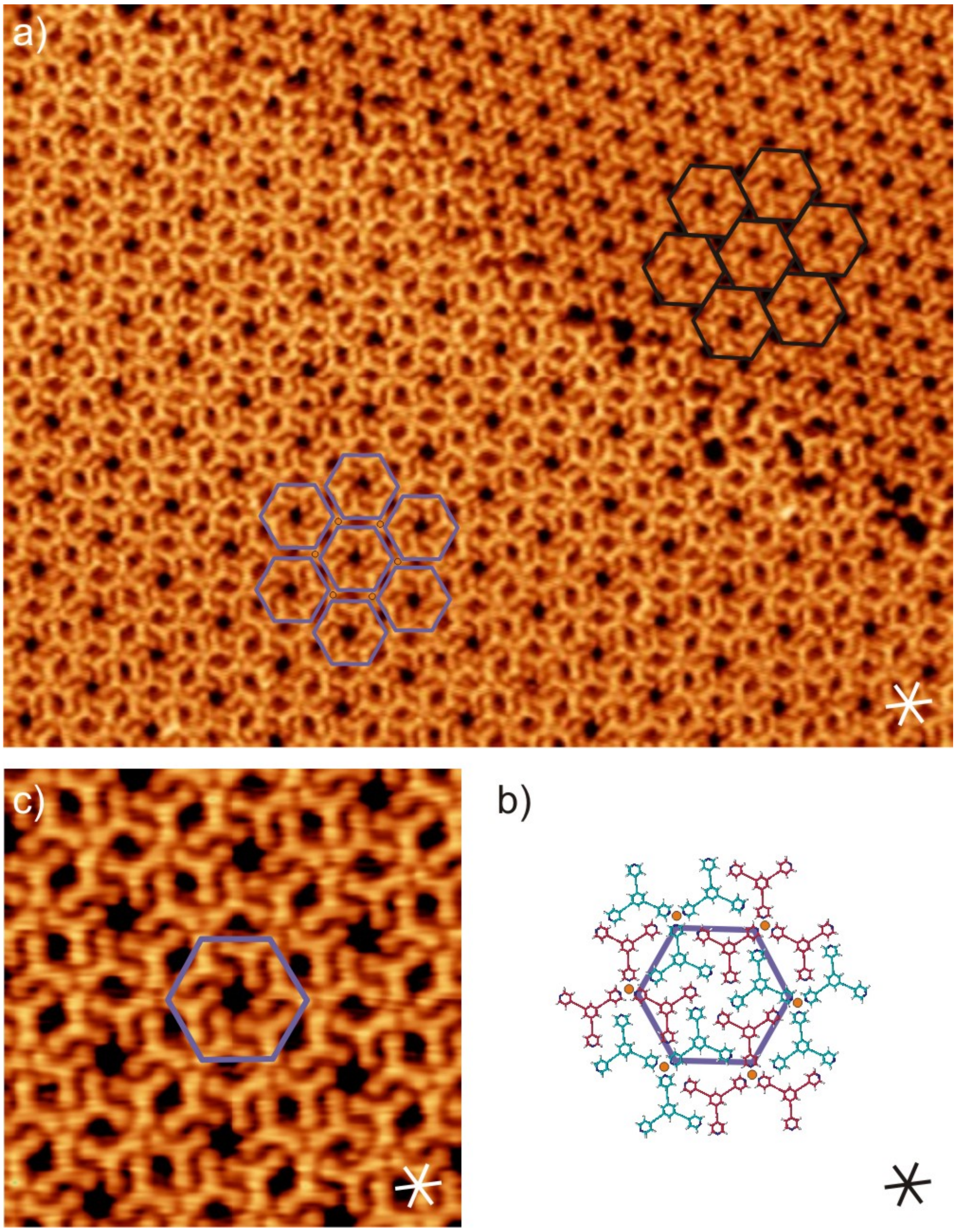

Figure 3.6: Phase ϵ: A 2D molecular porous network exhibiting a simultaneous expression of three-fold Cu-pyridyl interactions and lateral pyridyl-pyridyl links, obtained by the deposition of 0.9 ML of module **1** and Cu on Ag(111). a) Long-range STM image of the coexistence of phases α (non metallated) and ϵ. b) Zoom-in of image a) displaying submolecular resolution of phase ϵ. c) Atomistic model of phase ϵ. The black and violet hexagon represent the countour of the Rosetta tecton in phase α and in phase ϵ, respectively. The closed-packed directions of silver are depicted by white or black crosses. Image size: a,d) 440 Å × 344 Å b,e) 111 Å × 111 Å. Tunneling parameters: a) $I = 0.2$ nA, $V_b = -1$ V; b) $I = 0.4$ nA, $V_b = -1$ V.

for molecule 1 were taken from **OPLS-AA** force field while for the Ag (111) surface the modified **GolP** model [90] with the parameters for silver from Ref. [91] was used. The simulation box (58 Å× 50 Å× 80 Å) consisted of four layers of silver atoms (400 atoms each) and 6 molecules **1**. Long-range electrostatic interactions in the system were calculated using the particle mesh Ewald method with cutoff equal to 12 Å. To calculate van der Waals interactions the same cutoff (12 Å) was used. All **MD** runs were done for 5 ns.

The Monte Carlo simulations were performed on a 120 × 120 triangular lattice of equivalent adsorption sites using the conventional canonical ensemble Monte Carlo method with Metropolis sampling. [92] [93] To eliminate edge effects periodic boundary conditions in both directions were applied. The tripod molecule 3.2 was represented by the rigid **C3**-symmetric planar structure comprising four identical segments (core and three one-membered arms) showed in Figure 3.2. It was assumed that one molecular segment occupies one lattice site. The molecules were assumed to interact via a short-ranged segment-segment interaction potential limited to nearest-neighbors on a triangular grid. To account for the dominant contribution of the directional $N\cdots H$ interactions in stabilization of the Rosetta motif, only the interactions marked in orange in the configuration from Figure 1 were considered and their energy was set to -2.5, expressed in **kT** units. For all remaining molecular configurations (not shown) the segment-segment interaction energy was equal to zero. The simulations were performed for 1000 molecules **1** . To equilibrate the system up to **AAA** MC steps were used. [92] [93]

3.4 2D Short-Range Disordered Crystalline Networks From Flexible Molecular Modules

In this section, a 2D short-range disordered molecular crystalline networks with the module **1** is presented, which, regarding spatial organization, can be considered as surface analogues of 3D flexible crystals. It is interesting to note that the molecule **1**, which appeared rigid on the Ag(111) substrate, evidences a flexibility on Cu(111) substrate. The flexibility of the molecule **1** gives rise to distinct phases, whose characteristics have been examined in real space by STM: a 2D short-range distortional disordered crystalline network and a 2D short-range orientational disordered crystalline network, respectively. Both phases exhibit a random arrangement of nanopores that are stabilized by the simultaneous presence of metal-organic and pyridyl-pyridyl interactions. In the 2D short-range distortional disordered crystalline network, the framework displayed unprecedented flexibility as probed by the

STM tip that modifies the pore shape, a prerequisite for adaptive behavior in host-guest processes.

3.4.1 Introduction:

Unraveling the nature of complex condensed matter systems like glasses, glassy crystals, quasicrystals, protein and virus crystals is of paramount importance in actual material science. [94] [95] [96] [97] [98] [99] The traditional conception of a crystal based on translational symmetry has been widened upon the discovery of quasicrystals and since 1992 a crystal is defined by the International Union of Crystallography as any solid having an essentially discrete diffraction pattern. [100] On the other hand, in three-dimensional (3D) materials science, an amorphous solid is considered as a material that possesses a non-crystalline structure. [101] In particular, it is called a glass if it undergoes a glass transition when heated to the liquid state. [95] [101] In addition, a flexible molecular crystal is a material exhibiting a glass transition involving a rotational disorder of the constituting molecular units, whereas these constituents span a regular crystalline lattice. [102] [103] [104] [105] [106] [107] [108] [109] [110] Recently, by exploiting self-assembly protocols on surfaces, [67] two-dimensional (2D) supramolecular random networks have been fabricated on metallic surfaces and associated with glasses. [111] [112] To simplify terminology (cf. Scheme 1.b) and transferring the former definitions and concepts into the 2D space, in this paper we employ the term 2D short-range disordered crystalline network to describe a 2D material that displays a discrete diffraction diagram and presents any of the following ordering characteristics: 1) the constituents are positioned following a crystalline lattice, but at the same time disordered with respect to their orientational or distortional degrees of freedom or 2) the intermolecular links span a crystalline lattice, but the molecular building blocks present distortional (cf. bottom left of Scheme 3.7b) or orientational (cf. bottom right of Scheme 3.7b) short-range disorder. Therefore, regarding the spatial organization, a 2D short-range disordered crystalline network could be considered as a surface analogue of a 3D glassy crystal, though a temperature dependent glass transition should be identified for certainty from the thermodynamic point of view.

Traditionally, most insights into the structure of non-crystalline materials have been based on diffraction techniques that rely on space averaging. Only recently, the employment of self-assembly protocols on surfaces to create surface-confined supramolecular random networks and their in-situ visualization with Scanning Tunneling Microscopy (STM) have provided crucial breakthroughs regarding the local order characteristics of the 2D amorphous structures. [111] [112] [113] [114] The

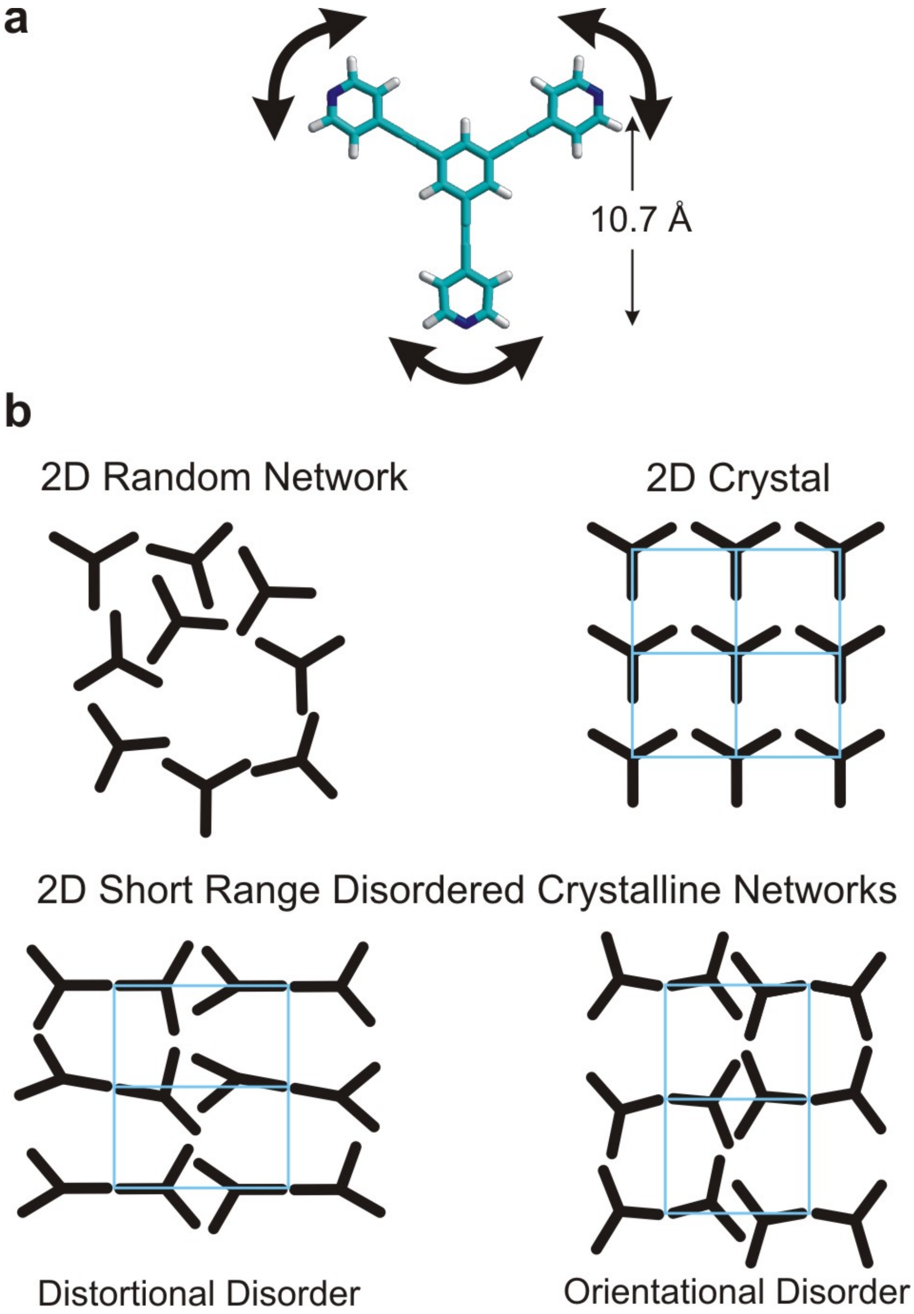

Figure 3.7: *

Scheme 1: a) Schematic model of compound 1 (top view), in which molecular dimensions were obtained for an isolated molecule in the gas phase using the Hyperchem software (**MM+** method). Black arrows indicate the flexibility of the terminal groups. b) Types of assembly of a 2D supramolecular structure with different short- and long-range order characteristics for a tecton with 3-fold symmetry and geometrical flexibility. The blue network represents a crystalline lattice.

extension of this approach to other complex condensed matter systems could allow us to develop new materials and to greatly enhance our understanding of the physical phenomena associated with crystallization and vitrification, which are of crucial importance in a variety of fields like pharmacology or materials science.

Regarding the supramolecular approach, for many surface-confined self-assembled nanostructures, the enthalpies associated with lateral intermolecular interactions are relatively weak thus implying that a fine interplay of enthalpic and entropic contributions determines the final self-assembled pattern. In particular, upon formation of a nanostructure, freezing conformations of a flexible molecule can make loss of the conformational entropy more significant to the self-assembly process, [115] even leading to non crystalline condensed matter states. The realization of 2D disordered systems thus requires a specific balance between molecule-surface and intermolecular interactions and entropic contributions in the self-assembly to avoid the formation of patterns dictated by the surface lattice periodicity.

In this section, exploiting the self-assembly route to organize an inherently-flexible molecular module (molecule 1), we report the formation of 2D porous short-range disordered crystalline networks on Cu(111): a 2D short-range distortional disordered crystalline phase (ζ) and a 2D short-range orientational disordered crystalline phase (η). Our study visualizes with submolecular resolution a molecular self-assembly exhibiting simultaneously short-range disorder and crystalline long-range order. Furthermore, we probe the flexibility of the nanoporous phase ζ by inducing a flipping of the terminal groups with an STM tip, suggesting an adaptive behavior of the hosting networks towards molecular guests, a crucial property for exploitation in molecular recognition. [116] [117] Consequently, phase ζ represents a *soft porous crystal* in 2D. [118]

3.4.2 Results and discussion:

Molecule **1**, **1,3,5**-tris(pyridin-4-ylethynyl)benzene, consists of three pyridyl groups connected to a central aryl ring through alkyne moieties (cf. scheme 3.7.a). The functional terminal groups are programmed to steer metal-organic interactions through pyridyl-metal-pyridyl coordination motifs. [74] [75] [76] [77] [78] A key characteristic of this molecular module is the inherent flexibility of the substituents (≡CPyr) at the central aryl group, which can substantially deviate from the ideal 120° internal angle between two pyridin-4-ylethynyl peripheries, distorting the expected three-fold symmetry. This phenomenon has been previously observed by us with porphyrin derivatives equipped with identical pyridyl functional groups exhibiting a distortional adaptation upon surface adsorption. [77] [119]

The deposition of compound **1** on Cu(111), at a substrate temperature of 350 K, results in an assembly that exhibits polyamorphism controlled by the coverage. Images taken at very low coverage (< 0.01 ML) show that the molecular species completely decorate the steps before ordering on the terraces, indicating a high mobility at 350 K. For increased coverages below 0.2 ML, module 1 self-assembles in a 2D porous short-range distortional disordered crystalline network (phase ζ, cf. Figure 3.8 a,c,d and 3.9). Phase ζ appears in coexistence with a minority 2D porous random network (cf. Figure 3.9a,b). At intermediate coverage ($0.2 - 0.5$ ML) phase ζ coexists again with residues of the 2D random network and an additional phase labeled η, which represents a 2D porous short-range orientational disordered crystalline network (Figure 3.8). At higher coverage (> 0.5 ML), phase ζ is not detected and densely packed crystalline molecular islands emerge, coexisting with phase η domains, which diminish with the coverage. For all coverage ranges an annealing procedure close to the temperature of desorption ($T_{desorption} \approx 393$ K) had no noticeable impact on the organization. Whether the 2D short-range disordered crystalline phases are kinetically frustrated or thermodynamically stable is still under debate.

3.4.3 Low coverage polymorphism:

As depicted in Figure 3.8a, for coverages below 0.2 ML the deposition of compound 1 results in the formation of a 2D porous short-range distortional disordered crystalline network (phase ζ, cf. Figure 3.8c) that coexists with a minority 2D porous random network (cf. Figure 3.8b). For clarity, the structural nature of phase ζ as a 2D short-range disordered crystalline network will be addressed below. Phase ζ is based on pores formed by the combination of six molecules (named as pores A); whereas the 2D random network exhibits pores formed by six, eight, nine, ten, eleven and twelve molecules (named as pores A, B, C, D, E and F, respectively, cf. Figure 3.8b). Remarkably, phase ζ and the 2D random network share pore A as a constituent motif. A statistical analysis of the fractional pore occurrence at ~ 0.2 ML coverage reveals a distribution where pores of type A dominate ($\approx 60\%$), followed by those of type B ($\approx 20\%$). With a probability of less than 10%, bigger pores of type C ($\approx 9\%$), D ($\approx 9\%$) and F ($\approx 2\%$) are observed. Rarely, pores constituted of eleven molecules were also detected (named as pore E, cf. Figure 3.8b).

High-resolution data (cf. Figure 3.8d) allow us to discern individual molecules with submolecular features. Each molecule is characterized by four lobes, which correspond to the central aryl and the three peripheral pyridyl groups, respectively. Notably, the molecular appearance in the STM images deviates from a strict threefold symmetry (cf. Scheme 1), which highlights the intrinsic flexibility of molecule

1 upon adsorption on Cu(111). Herein, a minor contribution of the out-of-plane rotation of the pyridyl end groups cańt be neglected. [120] A structural analysis displayed apparent opening angles between pyridin-4-ylethynyl functions ranging from 99° to 155° (cf. Figure 3.8e and Figure 3.8h). The intramolecular flexibility is the major element for the formation of the 2D short-range disordered crystalline networks and the minority 2D random network, respectively, as it leads to multiple configurations of the molecule, [121] to be called *scissomers*, in analogy to the scissoring vibrational mode. In addition, as clearly displayed in Figure 3.8d, the networks exhibit two different recognition motifs (cf. Figure 3.8g): i) a head-to-head orientation between two "dim" pyridyl groups of neighboring molecules with a projected **N-N** distance of 3.4 ± 0.4 Å [74] [75] [76] [77] [78] and ii) an interaction of one bright pyridyl group per molecule with an adjacent pyridyl ring. The latter motif is assigned to a noncovalent interaction with a characteristic **N-H** length of 1.8 ± 0.4 Å, similarly identified at the liquid-solid interface. [81] The pyridyl groups involved in this lateral pyridyl-pyridyl interaction are visualized as bright protrusions independent of the applied bias voltage, suggesting a non-parallel orientation of the heteroaromatic ring relative to the surface. Based on the N-N spacing and previous reports, motif i) is identified as a pyridyl-Cu-pyridyl metal-organic interactions, where the mediating Cu adatom (supplied by the surface) [122] [84] is not resolved. [74] [76] [77] [84] [123] [124] Summarizing, each molecule is engaged in two metal-organic coordination bonds and two lateral pyridyl-pyridyl contacts. This demonstrates for the first time a simultaneous expression of these two different interactions, in contrast to previous studies based on the same terminal functional groups, where only metal-organic interaction dominates. [74] [76] [77] [78] The prevalent expression of type A pores signals a more favorable bonding configuration as compared to pores of type B and C. [125]

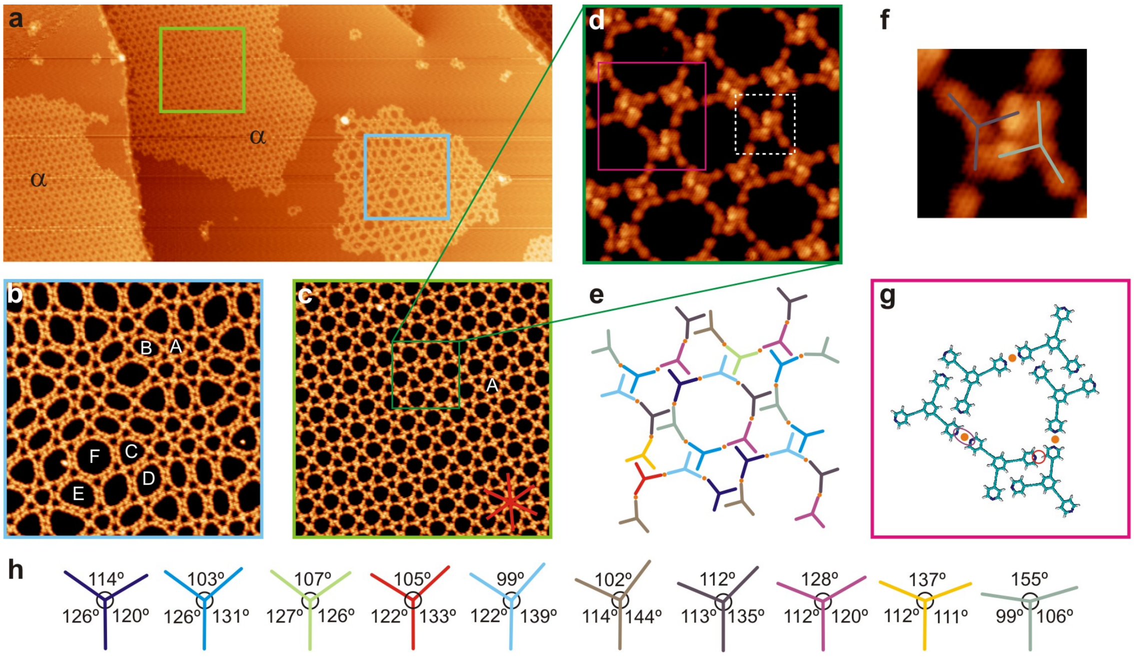

Figure 3.8: Self-assembly of compound **1** on Cu(111) into a 2D short-range distortional disordered crystalline network (phase ζ) coexisting with a 2D random network, for coverages below 0.2 ML. a) Large scale STM image displaying one 2D random network island (blue square) and one 2D short-range disordered crystalline island (green square). b) Zoom in the 2D random network region of Figure 1a. The different types of pores are labeled with the letters **A, B, C, D, E** and **F**, respectively. c) Zoom in the 2D short-range disordered crystalline region of Figure 1a. Only the pore of type A is present in this assembly. The red star represents the close-packed directions of Cu(111). d) High resolution STM image obtained with a CO terminated tip depicting with submolecular resolution phase ζ. e) Model of Figure 1d in the "stick" representation, in which each stick reflects the angular deviation from the ideal three-fold molecular symmetry. Molecular units exhibiting the same apparent opening angles are depicted with the same colors. Cu adatoms are represented by an orange circle. f) Zoom-in of white-doted area of Figure 1c and superposition of the stick model on two molecules. g) Model of the two bonding motifs stabilizing the network in the Hyperchem framework: a two-fold pyridyl-Cu-pyridyl bond (highlighted by a purple ellipse) and a pyridil-pyridyl interaction (highlighted with a red circle). h) Stick representation of the different molecular configurations of Figure 1d, scissomers, as adapted upon surface adsorption. Images sizes: a) 2963×1380 Å^2; b-c) 443×443 Å^2; d) 110×110 Å^2; f) 25×25 Å^2. Tunneling parameters: a-c) $I = 0.03$ nA, $Vb = 1$ V; d, f) $I = 0.05$ nA, $Vb = -0.075$ V.

3.4.4 2D short-range distortional disordered crystalline network

A close inspection of phase ζ reveals to be constituted by pores of type A with slightly different shapes and a mean area of 576 Å^2 which combine to an assembly exhibiting long-range order (cf. Figure 3.9). The corresponding 2D autocorrelation plot, a mathematical technique to identify repeating patterns by depicting the cross-correlation of a measured image with itself, clearly shows a six-fold symmetric pattern with a periodicity of 44 Å (cf. inset of Figure 3.9a), with a deviation of 1.5 ± 0.5 Å, deriving from identical oriented protruding pyridyl-pyridyl contacts. These results are in full agreement with the Fast Fourier Transformation of the same image (not displayed). Due to the flexibility of the terminal groups, the molecules present distortions through the assembly, giving rise to pores A of different shapes (labeled with subscripts An in Figure 3.9b), which are responsible of the deviation of the lateral pyridyl-pyridyl motifs from a perfect lattice. Herein, the influence of the substrate is manifested in the presence of two organizational chiral domains, in which the lattice of the pyridyl-pyridyl contacts of the clockwise (counterclockwise) chiral domain is rotated 25° ± 5° (−25° ± 5°) with respect to the close-packed directions of Cu(111) (cf. Figure 3.8c, 3.8d and 3.9a for clockwise chirality). Based on the features of a 2D short-range disordered crystalline network introduced in the first paragraph and considering the deviation due to the flexibility of the modules, we conclude that phase ζ represents a molecular 2D short-range distortional disordered crystalline network. This visualization of a supramolecular 2D short-range disordered crystal represents a distinct condensed-matter state as compared to well-established 2D crystalline phases or 2D random networks. Such type of molecular architectures exhibiting a coexistence of amorphous and highly correlated structures are occasionally observed at the 3D mesoscale, for example in virus crystals. [126]

3.4.5 2D short-range orientational disordered crystalline network

For coverages exceeding 0.2 ML a second 2D short-range disordered crystalline phase appears. Figure 3.10a depicts a high-resolution image of the molecular assembly in phase η, in which, as in phase ζ, the molecular appearance deviates from a three-fold symmetry. However, in contrast to phase ζ and within the limits of the STM intramolecular resolution, we identify only a single molecular configuration (scissomer) constituting phase η, which exhibits apparent intramolecular opening angles between two legs of 107°, 120° and 133°, respectively. In addition, we distinguish six different molecular orientations of the scissomer (cf. Figure 3.10b). The bonding motifs of the assembly are identical to phase ζ, i.e., each molecule presents

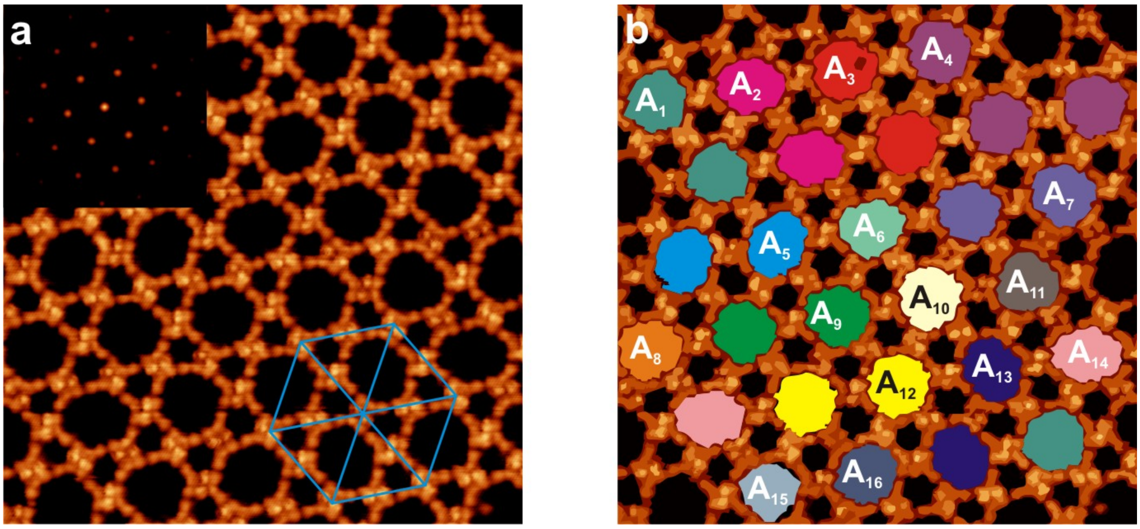

Figure 3.9: Self-assembly of compound **1** into a molecular 2D short-range distortional disordered crystalline network (phase ζ). High resolution STM images of an arrangement of type A pores in phase ζ obtained with a CO terminated tip. a) The inset displays the autocorrelation plot of the figure. Blue lines are used to describe the repeat motif with a unit cell vector length of 44 Å. b) Filling of the pores by assigning one color to each type of pore. The different pores are labeled with the term A_n (from A_1 to A_{16}). Images sizes: a-b) 242 × 242 Å^2. Tunneling parameters: a-b) $I = 0.052$ nA, $Vb = -0.075$ V.

two lateral pyridyl-pyridyl contacts and two pyridyl-Cu-pyridyl links with adjacent molecules (cf. Figure 3.10c). However, the density and topology of phase η differs from phase ζ: in phase η the links between adjacent pores rely on pyridyl-Cu-pyridyl bonds, whereas in phase ζ the connection between pores is solely based on the lateral pyridyl-pyridyl interactions. The resulting porous network comprises different pores of rhombic shape, with a mean area of 184 Å^2, each one characterized by a particular combination of orientations of the scissomers. The repeatedly observed pore shapes are labeled in Figure 3.10b,d (F1 to F9) and displayed with a color-coded filling in Figure 3.10d. Within the assembly, the spatial distribution of the pore shapes is random (Figure 3.10d). Nevertheless, the autocorrelation plot of the assembly (inset of Figure 3.10a) displays a periodic order with a rectangular repeating motif of size 29.5 Å × 17.7 Å, defined by the lateral pyridyl-pyridyl contacts (see blue rectangular lattice in Figure 3.10a). Herein, the influence of the substrate is again visualized by the presence of a chiral organization, constituted by three orientational domains per chirality giving a total of six domains, in which the long unit vector of the lattice of the lateral pyridyl-pyridyl contacts forms an angle of $17° \pm 5°$ in chirality of type I and $-17° \pm 5°$ in chirality of type **II** with respect to the close-packed directions of Cu(111) (cf. Figure 3.10a for chirality of type I). Thus, by analogous arguments as those used for the description of phase ζ, we conclude that the assembly of phase η constitutes a 2D short-range orientational disordered crystalline network.

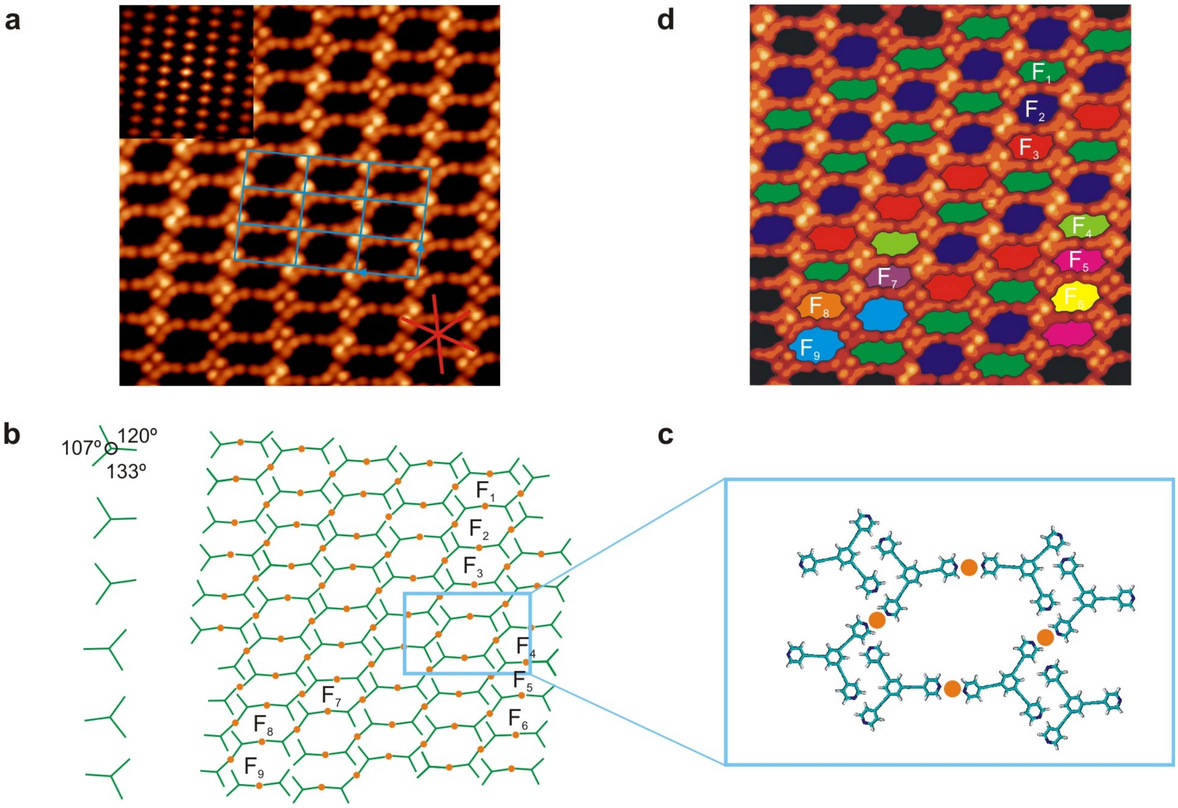

Figure 3.10: Self-assembly of compound 1 into a supramolecular 2D short-range orientational disordered crystalline network. a) High resolution STM image depicting different types of rectangular pores obtained with a CO terminated tip. To clarify the visualization of the molecular units a green "stick" model is superimposed on the top right of the image. The inset represents the autocorrelation plot of the image. The repeating motif is displayed as a blue lattice with unit cell vector lengths of 29.54 Å and 17.7 Å. The red star represents the close-packed directions of Cu(111). b) Model of Figure 3a in the "stick" representation, in which each stick reflects the angular deviation from the in-gas three-fold molecular symmetry. Molecular units exhibit the same configuration (scissomer) and six different orientations upon adsorption on the surface. c) Model of the two bonding motifs stabilizing the network: a two-fold pyridyl-Cu-pyridyl bond and a lateral pyridyl-pyridyl interaction. In Figures 3a-3c Cu adatoms are represented by an orange circle. d) Filling of the pores of Figure 3a, assigning one color to each type of pore and labeling them with the term Fn (from F1 to F9). Images size (a,d): 184 × 184 Å^2. Tunneling parameters: $I = 0.2$ nA, $V_b = -0.2$ V.

The molecular flexibility resulting in different configurations upon adsorption that deviate from a strict three-fold symmetry is a key ingredient for the assembly of the above-discussed 2D short-range disordered crystalline network and of interest for engineering functional templating structures. Remarkably, the flexibility of the terminal groups is directly proven by STM experiments that can simultaneously induce and visualize distortional changes in the networks. To this aim, we modified the STM scanning conditions that were initially established to image the assembly under non-perturbative conditions. Thus, it was possible to induce modifications of the networks and directly observe the resulting temporal variations of the pore shapes in phase ζ (cf. Figure 3.11a-h). A detailed analysis reveals that these alterations are mediated by a subtle variation in the opening angle of the pyridyl legs involved in the two-fold pyridyl-Cu-pyridyl bond, thus inducing a change in the size and shape of some pores (*cf.* Figure 3.11i-k). This intrinsic flexibility of the metal-organic motif has been already observed for porphyrin-based coordination-polymers on Cu(111) presenting the same peripheral pyridyl groups. [76] [119] It was attributed to the inherent flexibility of the substituted leg ($\equiv$ CPyr) combined with a low-energy cost for deflecting the pyridyl-Cu-pyridyl bond angle away from 180°.

Our results suggest that phase ζ represents a soft porous crystal in 2D. Analogous materials are established in 3D as third generation porous coordination polymers revealing to be of paramount importance in the field of host-guest complexation, because they exhibit dynamic frameworks that are able to respond/adapt to external stimuli such as light, electric fields or particular guest species, while retaining high regularity. [118]

3.5 Guest confinement in a flexible porous network

Inspired by the flexibility of the porous network and taking into account that this assembly on Cu(111) presents pores of different size and shape, we have focused on the adaptive behavior of the host framework towards a functional module, in particular, a molecular rotor, [127] [128] a Bis(porphyrinato)cerium double decker, i.e., Ce(TPP)$_2$. [129] The structure and electronic properties of Ce(TPP)$_2$ (referred here as module **2**) and its capabilities as a rotor is described in chapter 4. Due to its rotor capability, the double decker is a promising candidate for confining them on flexible porous networks because by confining the double decker in a flexible pore, the top porphyrin of the double decker can be manipulated in the azimuthal angle with the STM tip while the bottom porphyrin remains fixed in the adapted pore.

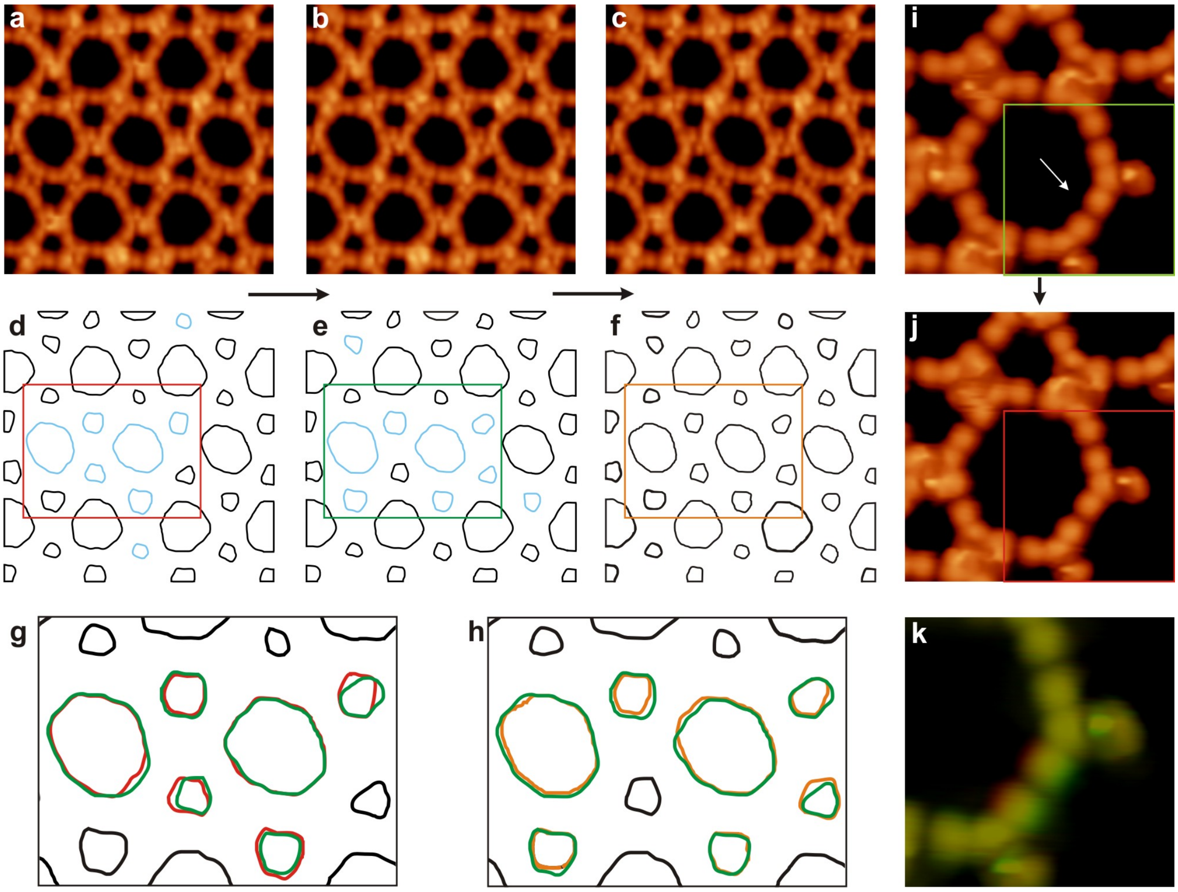

Figure 3.11: Dynamics of the ζ-short-range disordered crystalline network probed by scanning with an STM tip. a-c) STM images of an a) initial, b) intermediate and c) final configuration of an assembly of phase ζ, after recording three subsequent STM images. d-f) Vectorization of images a-c, respectively, outlining the contour of the pores by a trace. Blue line in d) and e) represents those pores which change their shape while scanning from d) to e) and from e) to f), respectively. g) Zoom in and superposition of figures d) (red rectangle) and e) (green rectangle). h) Zoom in and superposition of figures e) and f) (orange rectangle). Black line is used to depict those pores which does not modify their shape; whereas red, green and orange line represent pores of d), e) and f), respectively, which change their shape while scanning from one image to another. i,j) Initial and final configuration of a pore of type A at the border of an assembly, displaying the change in geometry of the pyridyl-Cu-pyridyl bond, marked with a white arrow. k) Superposition of a zoom-in of image i) (green rectangle) and j) (red rectangle), to address the change between both images. Images sizes: a-c) 140 × 140 Å^2; i,j) 48 × 48 Å^2, k) 29 × 29 Å^2; Tunneling parameters: a-c) $I = 0.1$ nA, $V_b = -0.7$ V; i,k) $I = 0.1$ nA, $V_b = -0.07$ V.

As detailed in chapter 4, the $Ce(TPP)_2$ consists of a double decker complex with a rare-earth ion (Cerium) connecting two macrocycles of a porphyrin. This sandwich structure provides rotational degrees of freedom, where the top molecular plane (rotor) is able to rotate with respect to the bottom one (stator), anchored on the surface. [130] [131] [132] [133] In order to block any undesired lateral translation of the whole module **2** during rotation attempts, it is crucial that the bottom porphyrin of the $Ce(TPP)_2$ complex is well fixed by the host pore. In this sense, the porous network made by module **1** constitutes the ideal playground to test the behavior of module **2**2 on surfaces, regarding the confinement of the stator within pores of different sizes by the host framework.

Figure 3.12 exhibits the adaptation of pore *a* to the molecular guest. By a careful inspection of the shape and size of pores of kind *a* before (*cf.* Figure 3.12a and 3.12d) and after the insertion of a host molecule (cf. Figure 3.12b and 3.12e), we detect that the opening angles of the molecular species **1** that build pore *a* are modified in order to host the double decker complex. As a result, the area comprised by pore *a* is increased, but also the adjacent pores of type A are modified. In addition, by a comparison of the topographic appearance and apparent height of the double decker complex in pores of bigger size, we observe that compound **2** is adsorbed directly on the metal whenever it is trapped on any type of pore, thus establishing molecule-substrate interactions through its bottom porphyrin.

One important consequence of the adaptation of pore *a* to the double-decker complex is that the bottom porphyrin of the guest module is locked by the surrounded framework. As a result, by scanning with the STM tip at normal imaging conditions ($I = 0.09$ nA, $V_b = 1.4$ V) we are able to rotate $\sim 60°$ the top porphyrin of the double-decker species with respect to the bottom porphyrin, without translating the whole species (cf. Figure 3.12c and 3.12f), which is in further agreement with tip induced rotations of these double decker species on Ag(111). [129] Herein, since no alteration of the host pore was observed while inducing the STM manipulation, we discard any rotation of the bottom porphyrin. Further experiments on bigger pores like B, C or D lead to a combined movement of rotation and translation. These results open the way towards novel techniques to anchor functional modules on surfaces by exploiting inherent flexibility of the host framework, while keeping the functionalities of the designed guests.

3.5.1 Conclusion

In summary, we have studied the self-assembly on Ag(111) and Cu(111) of a tripod molecular compound explicitly synthesized to exhibit a coexistence of supramolec-

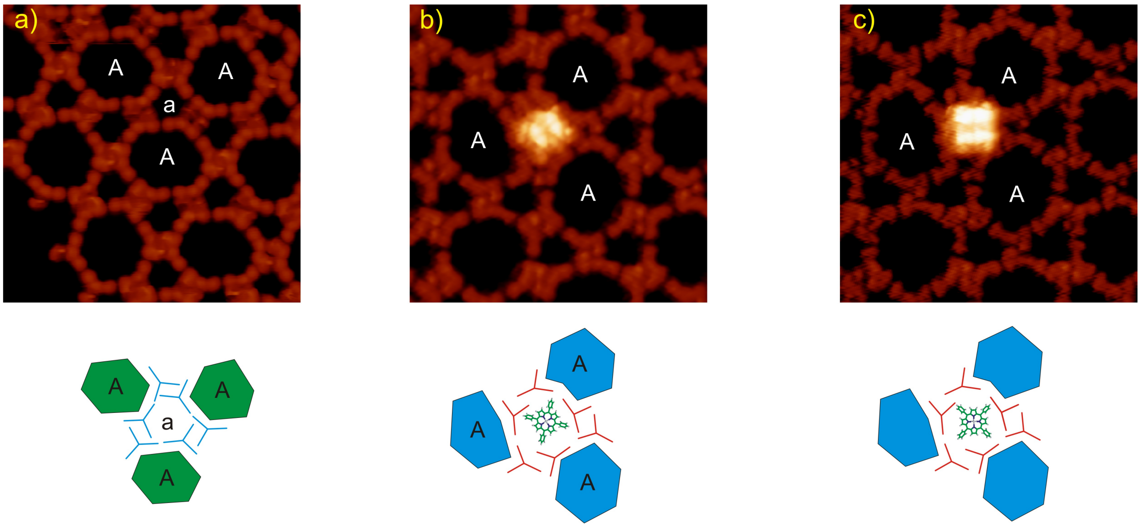

Figure 3.12: Accomodation of a molecular rotor guest (compound 2) on a pore of type A of the flexible porous network made by module 1 on Cu(111). The chirality of the porous network is different in a) than in b) and c). a-c) STM images: a) Flexible porous network exhibiting two types of pores, *a* and A; b) One of the pores of type *a* is decorated by a double decker complex; c) Rotation of the double-decker depicted in b) by STM scanning at $I = 0.09$ nA, $V_b = 1.4$ V. STM image a) corresponds to a different substrate orientation than b,c). d-f) Schematic representation of the STM images. d) Initially, pores of type A present a quasi-hexagonal shape. e) After the dosage of Ce(TPP)$_2$, pore of type *a* adapts to fix tightly a molecular rotor unit, through the folding of some pyridyls groups, which results in a distortion in the shape of both pore *a* and adjacent pores A. f) The nice match between the bottom porphyrin of double-decker complex and the host frameworks allows rotation by an STM tip. For better clarity, molecule **1** is modeled by tubes, while Ce(TPP)$_2$ exhibits the functional groups from a top-view perspective, depicting only the top porphyrin. Images sizes: a-c) 111×111 Å^2. Tunneling parameters: a) $I = 0.7$ nA, $V_b = -0.05$ V; b) $I = 0.9$ nA , $V_b = 1$ V; c) $I = 0.9$ nA , $V_b = 2$ V.

ular interactions in the presence of Cu adatoms, i.e., lateral pyridyl-pyridyl and pyridyl-Cu links. The deposition of the linkers on bare Ag(111) results in the formation of a 2D molecular hexagonal porous network (coined phase α) based on lateral pyridyl-pyridyl interactions, with a characteristic pore shape (Rosetta) made of six interacting molecules. At submonolayer molecular coverage, subsequent deposition of Cu alters dramatically the scenario giving rise to a coexistence of three different 2D molecular porous phases: β, γ and δ. Phases β and γ are based on a simultaneous expression of the expected interactions, whereas phase δ corresponds to a fully metalated network, being stabilized by just pyridyl-Cu-pyridyl metal-organic bonds. Remarkably, phase β exhibits a two-level hierarchic design protocol by which the Rosettas pores are placed in a hexagonal arrangement, with a higher interpore distance than in phase α, being connected together thanks to additional linkers establishing two-fold Cu-pyridyl bonds with the Rosettas. By increasing the molecular coverage, the influence of the molecular pressure is manifested in a reduction of the previous polymorphism. At a coverage of 0.8 ML, only phase β is detected coexisting with phase α. Close to the monolayer, a new phase evolves (phase ϵ), coexisting only with residues of phase α. Phase ϵ is described as a two-level hierarchic porous assembly in which the Rosettas are hexagonally distributed on the surface being directly linked to each other by three-fold Cu-pyridyl bonds, giving an intermediate interpore distance, when compared to phases α and β.

In addition, phases α, β, γ and δ present organizational chirality, which enhances the potential of the 2D molecular porous networks described above for future molecular recognition process.

Thus, on Ag(111) we have described in detail the potential use of the simultaneous expression of interactions on a surface as a route to promote hierarchic porous designs, which, in our particular case, resulted in the formation of porous networks exhibiting a tuning of the interpore distance.

On Cu(111) we report the formation of novel porous networks, which exhibits 2D short-range distortional or orientational disorder respectively. The networks exhibit the disorder due to the inherent flexibility of the molecule. They have been produced on a Cu(111) support by exploiting supramolecular self-assembly protocols relying on a programmed flexible molecular module and characterized at the molecular level by scanning tunneling microscopy. These 2D short-range disordered crystalline networks are stabilized by a combination of pyridyl-pyridyl links and metal-organic bonds. The intermolecular pyridyl-pyridyl links follow a regular lattice, but through the network either the distortion (phase ζ) or the orientation of the molecular modules (phase η) is random. Two coexisting 2D short-range disordered crystalline networks exhibiting a different topology were observed at intermediate molecular coverage. One is described by a rectangular repeating motif in the autocorrelation plot (phase η), whereas the other one exhibits a hexagonal symmetry (phase ζ). The flexibility of phase ζ is addressed via STM stimuli that results in slight distortional changes of the pores, whereby the network structure is retained. This represents a 2D representation of soft porous crystals, suggesting a dynamic adaptive behavior, crucial in molecular recognition and self-repairing processes. In this sense, the simultaneous stabilization by metal-organic coordination bonds and pyridyl-pyridyl links provides an advantageous balance between robustness and adaptability for future applications. Altogether, our results open new avenues towards the fabrication and understanding of novel condensed matter systems.

Finally, to conclude, this host framework which is made of an inherently flexible molecule allows the smallest type of pore to accommodate an azimuthal molecular rotor based in a double-decker porphyrinato complex. By manipulation with an STM tip, we show that it is possible to induce a rotation of the top porphyrin of the double-decker complex, without translation of the module.

Taking into account the versatility of both organic chemistry and surface-confined supramolecular chemistry, we consider our work will pave new avenues towards the design of complex 2D molecular porous networks that are useful for confining explicitly synthesized organic guests.

3.5.2 Experimental details

For all the experiments, a submonolayer coverage of molecular derivative **1** was deposited by organic molecular beam epitaxy from a thoroughly degassed quartz crucible held at 463 K. During deposition of module **1** the surface was kept at 343 K and the pressure remained $< 5 \times 10^{-10}$ mbar. All data were acquired at a sample temperature of ~ 6 K using electrochemically etched W tips. In the figure captions, V_b refers to the bias voltage applied to the sample. Simulations were performed in the framework of the Hyperchem 7.5 Software Package. The Monte Carlo simulation details for the molecule 1 on Ag (111) is described in the appropriate section.

4 | C_{60}-Ce(TPP)$_2$ architectures on Ag(111)

4.1 Outline

In the present chapter, we focus our attention on a potential technologically relevant binary system composed of a donor and an acceptor molecule on a noble metal surface, Ag(111). A non-covalent dyad consisting of a Ce(TPP)$_2$ double decker (DD) complex and a C_{60} molecule is presented.

To begin with, the protocols used for creating extended and ordered dense packed arrays of the Ce(TPP)$_2$ complex is mentioned followed by a description of its structure and electronic properties. The well ordered double decker island serves as an ideal platform for positioning individual molecules that could be addressed at a single molecule level. Herein C_{60} molecules are chosen for confinement on the double decker islands due to their interesting electronic properties. The electron rich double deckers and the electron accepting C_{60}s together make quintessential ingredients for potential donor-acceptor systems and photovoltaic devices.

The confinement of C_{60} on the double decker islands is studied in three separate phases named α, β and γ. Phase α denotes an individual C_{60} confined on top of a Ce(TPP)$_2$ (which is embedded in a dense packed island) thereby forming a dyad. After the single C_{60} molecules are studied, the sample is annealed at room temperature to create well ordered islands of C_{60} named as phase β. Phase β evidences a highly regular bi-layer arrangement where the C_{60}s lie in a unique zig-zag fashion. Further annealing of the sample leads to phase γ where the C_{60}s form a square like arrangement with a Ce(TPP)$_2$ molecule confined in the square. We first proceed by giving a brief introduction to porphyrins and the C_{60} molecules in the two following sections before describing phases α, β and γ. All the phases are studied at low temperatures. A major portion of the results reported in this chapter is reproduced from our previous publications. [129] [134]

4.1.1 Porphyrins

Porphyrins are extremely important molecules that occur naturally and play a key role in many biological processes and they have also been extensively studied in a chemical perspective. The structure of a porphyrin consists of four smaller pyrrole rings. Each pyrrole ring is made up of a nitrogen atom and four carbon atoms. The rings are linked to each other by a carbon atom that bridges one carbon atom nearest to the nitrogen atom of one ring to the carbon atom nearest to the nitrogen atom of the next ring (called the α carbon). Two hydrogen atoms are bound to two orthogonally placed nitrogen atoms resulting in a vacancy at the center. This parent molecule is called a freebase porphine and the central space in the molecule is helpful for metallating the porphyrin. The structure is aromatic and has delocalized π electrons spreading throughout the structure. [135] This delocalization of the electronic structure gives the porphyrin is unique structure when imaged through an STM.

Due to their interesting electronic structure and versatile geometry, porphyrins have been studied extensively alone and also in combination with various atoms, molecules and gases. Herein they have been an important ingredient in organic chemistry for creating extended metal-organic networks, [136] supramolecular architectures, [137] charge transfer systems, [138] photovoltaic devices [139] and host-guest chemistry. [140] Since several bacteria and plants contain chromophores based on light-harvesting porphyrins, these molecules play a key role in artificial photosynthetic devices. [141] Porphyrins have also been successfully used as donors in several donor-acceptor complexes and more recently as critical components in dye-sensitized solar cells especially due to their assistance in enhanced charge separation. [142] [143] [144] [145]

Sandwich complexes made of tetra pyrrole backbones that comprise lanthanide metal centers are extremely interesting. Such complexes can play an important role as single-molecule magnets, [146] [147] [148] field-effect transistors, [149] receptors for metal ions and functional units that express positive allosterism based on the rotation between the porphyrin planes, [150] and molecular multibit information storage, as a result of their rich redox properties. [151] Among the series of rare-earth double-decker complexes, those with cerium centers are especially interesting because they can exist in both +3 or +4 oxidation states. [152] [153] These kind of complexes have been studied in liquid [154] [155] and novel surfaces [131] environments in details but only recently they were successfully confined and imaged on surfaces. These sandwich structures provide rotational degrees of freedom, where the top molecular plane (rotor) is able to rotate with respect to the bottom one (stator) that is anchored on the surface. Hence the double decker molecules have been shown to behave as a molecular rotor that has a special appeal for next generation synthetic machines. [132]

4.1.2 C_{60}

After their discovery in 1985, Fullerenes have been widely researched for their fascinating properties like high temperature stability, tensile strength, geometry and electrical conductivity and also in combination with several other materials. Fullerenes are considered to be a third form of stable carbon structure after graphite and diamond. The most common form of Fullerene is the C_{60}. Their interesting chemical properties and various technological implications have made C_{60}s one of the key components in contemporary materials science and electronics. The C_{60} comprises of 60 carbon atoms and has a **truncated icosahedron** structure with a van der Waals diameter of ~ 1 nm. C_{60} fullerenes also occur in nature when carbon atoms at sufficient pressure and temperature nucleate to form the structurally stable spherical carbon ball. This method has been mimicked to synthesize high purity C_{60}s commercially. [156]

With regard to surface science C_{60}s have been studied extensively by STM and other surface sensitive techniques leading to a wealth of information on their electronic and geometrical structure. The structure of a C_{60} molecule has 20 hexagons and 12 pentagons and evidences two different bond lengths: the shorter double bonds between the hexagons and the longer ones between a hexagon and a pentagon. Due to their geometrical shape and rehybridization effects, C_{60}s are excellent electron acceptors. [157] They have an electron affinity of 2.65 ± 0.05 eV [158] and are shown to accept unto 12 electrons under special circumstances. [159] Hence C_{60}s have been considered for various donor-acceptor and charge transfer systems. [160] Due to its symmetrical structure, the molecular orbitals of C_{60} are largely degenerate. [161] The energy of highest occupied molecular orbital (**HOMO**) and lowest unoccupied molecular orbital (**LUMO**) resonances of a C_{60} in gas phase has been accurately determined by photoemission and inverse photoemission techniques and a band gap of ~ 4.9 eV has been identified. [162] However when deposited onto a surface, factors like screening effects from neighboring molecules, coulomb repulsion from the substrate alter their band gap significantly. Even molecular orientation and adsorption sites can have an influence on the energy level alignment of the C_{60}s on surfaces. [163] For example one molecule embedded in an extended C_{60} island on a Au(111) substrate, was shown to have a band gap reduced by 400 meV compared to a free C_{60}. This is because in an island the molecular states of the C_{60}s overlap and the local charges on the C_{60} are screened by free charge carriers due to this overlap. On various surfaces, STM studies have proven useful in addressing this issue of modified electronic structure of a C_{60} on a single molecule level. [164] [161] Consequently it is of high interest to study an individual C_{60} molecule which is further decoupled from the substrate, such that influence from neighboring molecules and screening effects are reduced.

4.1.3 Donor-acceptor dyads

In the present work, an attempt has been made to create a donor-acceptor dyad where the $Ce(TPP)_2$ porphyrin complex would act as a donor with C_{60} as the acceptors. The dyad has been addressed and characterized at a single molecule level in order to understand that intramolecular forces that stabilize the dyad.

A donor-acceptor **(D-A)** system consists of an electron rich donor and an electron acceptor forming a chemical bond that is capable of charge transfer. Such systems are essential pre-requisites for creating a photovoltaic devices. A photovoltaic device is a material in which visible light (UV and IR light in some cases) is converted into electric current. The operating principle of the device is described as follows: a photon is absorbed in the electron donor material leading to the formation of an electron-hole (exciton) pair. When the exciton reaches the **(D-A)** interface, they dissociate and the electrons and the holes are collected by separate electrodes. The exciton dissociation is typically mediated by using electric fields or heterojunctions. In recent years, many organic molecules have been studied for use in **(D-A)** systems since the optical absorption coefficient of organic molecules is high. Organic photovoltaic materials have some disadvatanges like low efficiency and stability, but certain advantages like cost effectiveness and ease of engineering overrule the drawbacks. Hence molecular donor-acceptor systems are crucial ingredients to build organic photovoltaic devices and to construct novel organic solar cells based on heterojunction interfaces [165] [166] [167] that serve to dissociate strongly bound photogenerated excitons. [168] [169] Herein, research efforts focus both on the combination of different **D-A** materials and the intermolecular coupling mechanisms aiming at the maximization of the power conversion efficiency of the device. [170] Specifically, fullerene-porphyrin architectures attract considerable interest given their remarkable photoactive, structural and magnetic properties. [171] [172] Fullerenes present extraordinary electron accepting characteristics, promoting ultra fast charge separation and exhibiting very slow charge recombination characteristics. [173] On the other hand, as key players in natural photosynthesis, porphyrins are ideal light harvesting units to be combined with electron acceptors as fullerenes. Recently, sandwich-type porphyrin and related tetrapyrrole complexes incorporating large central rare-earth ions have attracted widespread attention. [174] [146] [151] [150] [129] In particular, their unique electronic and optical properties include tunable broadband absorption, large exciton delocalization length, and ultrafast energy transfer between the macrocycles, which make these complexes as promising donors for photovoltaic devices. [175] [176] Accordingly, recent articles report successful photovoltaic cells with increased power conversion efficiency based on such complexes. [177] [178] [179] [180] In order to improve the performance of these devices it is of paramount importance to thoroughly characterize the **D-A** interface, where the decisive exciton dissociation takes place. [170] In the system presented in this thesis, no significant charge transfer was observed to make it an efficient photovoltaic system, but an attempt has been made to study a potential **(D-A)** system at a single molecule level.

Beyond being prototypes for donor-acceptor heterojunctions in organic photovoltaics, surface-confined dyads (bi-molecular units) provide significant potential for organic light emitting diodes, molecular switches or molecular machinery. The binding characteristics and the inherent electronic and mechanical properties of such bi-molecular nanostructures can be controlled by appropriately choosing the type of intermolecular interactions. Especially interesting are dyads where molecular recognition and stabilization occurs via weak van der Waals interactions, thus preserving the main electronic structure of the components and potentially permitting the molecular manipulation of the constituents. Herein, a particularly favorable situation is encountered with fullerene-porphyrin systems, where close intermolecular contats and selective supramolecular interactions prevail, [181] [182] [183] [184] however, to date only limited progress was made regarding the realization of related nanoscale arrangements amenable to single-molecule investigations. For an in-depth understanding of the physico-chemical principles of such systems, a thorough characterization of the geometric, mechanical and electronic properties of the dyad and the donor-acceptor interface is required.

To this end, we construct $C_{60}/Ce(TPP)_2$ dyads via self-assembly on Ag(111) as a model system to study the coordination of a promising donor ($Ce(TPP)_2$) [175] [176] and a well established acceptor unit C_{60}. [185] This approach is advantageous as the size and limited thermal stability of covalently linked $Ce(TPP)_2/C_{60}$ dyads [186] generally prevents a direct sublimation of the entire complex onto surfaces. In addition, studies of **D-A** dyads assembled by non-covalent interactions at solid-liquid interfaces lack the resolution to elucidate the nature of the intermolecular interactions involved, and, thus, cannot address the essential details of the **D-A** interface. [187] In particular, by combining **STM** and **STS** experiments we report the site-selective adsorption, electronic characterization, molecular orientation and controlled manipulation of C_{60} molecules on regular arrays of Ce(TPP)$_2$ double-decker complexes adsorbed on a Ag(111) single crystal support. The in-situ formed dyads exhibit a predominant face-to-face geometry between a porphyrin derivative and fullerenes which, despite considerable efforts, was not achieved previously at interfaces under ultra-high vacuum conditions. [188] [189]

The sample containing individually confined C_{60}s on Ce(TPP)$_2$ was was annealed at room temperature to create extended and ordered arrays of C_{60}s. This ordered array, phase β evidences a unique bi-layer arrangement of C_{60} where the bottom layers are still positioned on top of the double deckers. Hence we describe a way to conveniently create an organized C_{60} architecture that could potentially lead to bigger charge transfer systems as an extension of the single molecule system described previously.

Further annealing of the C_{60}/Ce(TPP)$_2$ leads to phase γ which is a square like arrangement of the C_{60}s with the Ce(TPP)$_2$ molecules confined in the center of the square. The Ce(TPP)$_2$ complex presumably undergoes a rotation that facilitates the square arrangement of the C_{60}s.

Hence we present three interesting surface architectures with the C_{60}/Ce(TPP)$_2$ combination. This highly controlled environment allows us to characterize the geometric, electronic and mechanical properties of the system. Our findings thus advance the understanding of surface-confined porphyrin-fullerene **D-A** dyads and the intricate supramolecular interactions involved. In view of the importance of a fullerene-porphyrin dyad structure in various potential photo-physical applications, it is useful to have a brief overview of the C_{60} fullerenes and porphyrins before describing the procedure to prepare a dyad made of these two molecules: the C_{60} and porphyrin related compounds.

4.2 Topographic analysis of the Ce(TPP)$_2$ complex

In this section, a platform of porphyrin double decker sandwich complexes mediated by a cerium atoms is described. After a highly regular 3D surface architecture of Ce(TPP)$_2$ (double decker) is created, this structure is used as a platform for the confinement of C_{60} molecules that could lead to a potential donor-acceptor complex. A **DFT** model of the Ce(TPP)$_2$ complex is shown in Figure 4.1.

In order to tailor extended islands of Ce(TPP)$_2$ complexes on a surface, two different protocols could be employed. *(i)* The first is an in-situ bottom-up fabrication approach where the porphyrins and the lanthanide metal are supplied separately

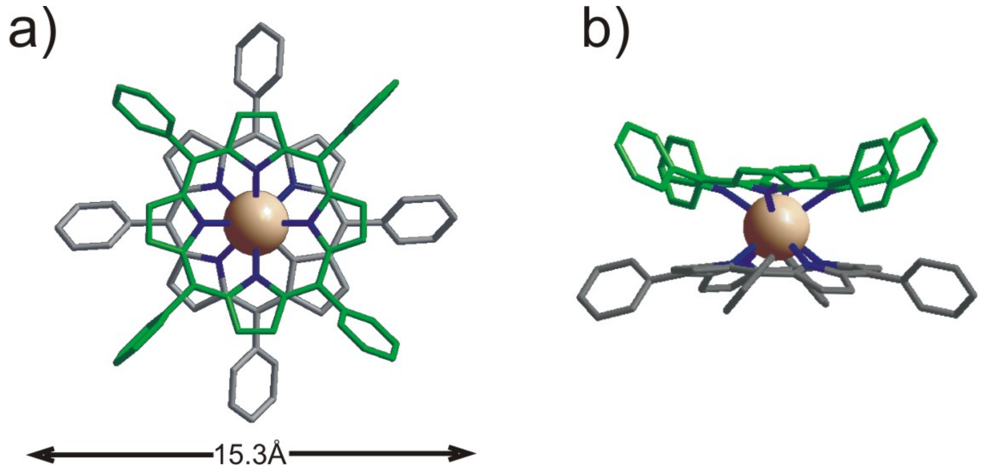

Figure 4.1: Top (a) and side (b) views of the **DFT** models of cerium double decker (Ce(TPP$_2$)) porphyrinatos. The bottom porphyrin is depicted in gray and the top porphyrin in green. The top porphyrin evidences a bowl-shaped geometry and has its axis rotated by $\sim 45°$ with respected to the bottom porphyrin. The central brown lobe corresponds to a cerium atom. Hydrogen atoms are not shown for clarity.

and appropriate conditions implemented to allow the growth of Ce(TPP)$_2$. Such an approach helps in understanding the fabrication pathways, stability, appearance and electronic structure of the complex. [129] *(ii)* The other approach is where the Ce(TPP)$_2$ molecules are sublimated directly as-synthesized, on to the surface to provide a ready made platform for guest adsorption. However such sublimation has to be performed carefully lest a risk of thermal decomposition and unclean molecular islands is encountered. Once the structure and electronic properties of Ce(TPP)$_2$ is understood, a platform of dense-packed Ce(TPP)$_2$ array is ready be used for manipulation or additional guest confinement.

In this thesis protocol *(i)* is used for studying the appearance of Ce(TPP)$_2$ and protocol *(ii)* is used for fullerene confinement.

Figure 4.2 shows a double decker array prepared by the in situ procedure. In the islands prepared by *(i)* it is observed that the upper porphyrin of the double decker lies exactly on top of the bottom porphyrin in the individual species as well as the dense-packed lattice. (Figure 4.5) In the dense packed array, the double deckers are in registry with the surrounding porphyrin lattice. Further the upper porphyrins of Ce(TPP)$_2$ are rotated about the azimuthal axis in the individual as well as the dense packed arrays. While a precise determination of the double decker conformation is difficult, we can rationalize the orientation of the Ce(TPP)$_2$ upper porphyrin. The double-decker molecules evidence a different structural symmetry at different sample biases. As we sweep through the sample bias from the negative to positive, it is possible to see a shift in the central axis of the molecule. This difference in

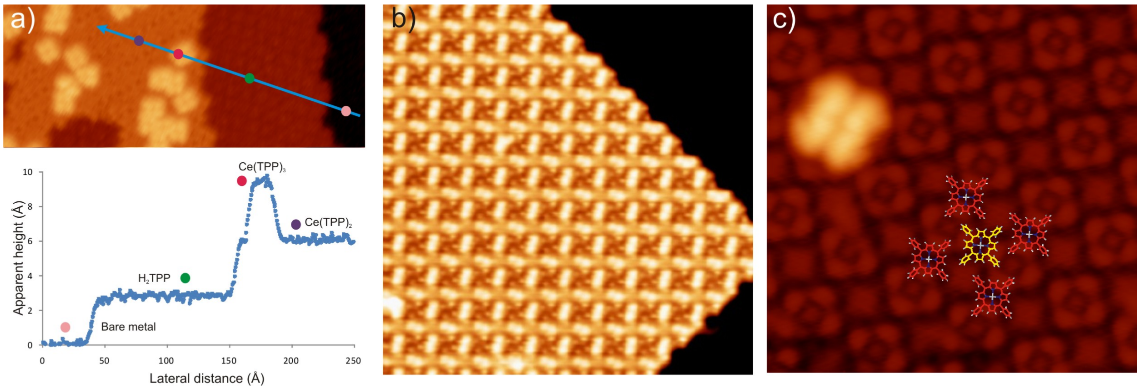

Figure 4.2: STM images of the self-assembly of double-decker cerium porphyrinatos on Ag(111) obtained by the in-situ procedure. (a) shows an STM image where the bare Ag(111) substrate, free base porphyrin (2HTPP) layer and a double decker layer is seen with bright individual triple decker molecules embedded on the double deckers. The apparent height of all the respective species in this image is shown alongwith. The double eskers co-exist with free base porphyrin islands at this coverage of 0.05 ML. 321 x 127 Å^2, I = 0.2 nA, V_b= 2.4 V (b) Image of a highly ordered Ce(TPP)$_2$ dense-packed layer at a different bias voltage. The double deckers imaged at this bias helps to identify the central axis of the complex as every molecule has an axis rotated by 90° with respect to its nearest neighbor. 443 x 443 Å^2, I = 0.4 nA, V_b= 0.3 V (c) Models of porphyrin superimposed on the STM image in order to identify the molecular position and orientation of the complexes in the dense packed structure. The isolated bright molecule corresponds to a single triple decker species. 96 x 96 Å^2, I = 0.1 nA, V_b= 1.4 V

appearance helps greatly in defining the main axis of the molecule (named as α and β orientations) which is useful for the C_{60} confinement experiments described in the following sections. An overview on the voltage-dependent appearance of Ce(TPP)$_2$ is given in Figure 4.3.

It was shown by the in-situ procedure that the upper porphyrin in the double decker is rotated by $(15 \pm 5)^\circ$ in the individual Ce(TPP)$_2$ complex, and by $(-45 \pm 5)^\circ$ or $(+45 \pm 5)^\circ$ in the dense packed islands, with respect to the bottom porphyrin. From this rotation of the porphyrin in the islands we could understand that the double decker islands form a square unit cell with Ce(TPP)$_2$ at each corner of the square and another Ce(TPP)$_2$ at the center of the square whose top porphyrin is rotated by 90° with respect to the others. The nearest neighbor distance amounts to 13.9 ± 0.5 Å . High-resolution images (Fig. 4.2b) exhibit a two-fold symmetry of the top porphyrin macrocycle which indicates a non-planar deformation. [Figure 4.5a]

The observation of a reduced macrocycle symmetry is consistent with an X-ray diffraction analysis of Ce(OEP)$_2$ revealing a slightly distorted square antiprismatic geometry with two bowled macrocycles [190] and theoretical descriptions of Ce(OEP)2 and CeP$_2$. [191] Indeed, our DFT-based geometry optimization of an isolated Ce(TPP)$_2$, considering the experimentally observed alignment of the macrocycles, reveals a non-planar deformation of the porphyrins and a propeller-like arrangement of the terminal phenyl groups of the top porphyrin of the complex (cf. Fig. 4.5b,d).

In particular, the macrocycle of the top porphyrin represents a bowl-like configuration, where one opposing pair of pyrrole rings is tilted more than the other pair, giving rise to the main axis of the complex introduced above and favoring the confinement of C_{60} (vide infra), which results in a molecular recognition phenomenon. The asymmetries in the Ce(TPP)$_2$ structure is shown in Figure 4.4.

4.3 Fullerene confinement on Ce(TPP)$_2$ arrays - phase α

4.3.1 Structural characterization of C_{60}/Ce(TPP)$_2$ dyad

To assemble C_{60}/Ce(TPP)$_2$ dyads, small amounts of C_{60} were deposited on porphyrin double-decker arrays held at 120 K. Generally, we employed submonolayer Ce(TPP)2 coverages enabling a direct comparison of C_{60} adsorption on bare Ag(111) and Ce(TPP)$_2$. The STM images in Fig. 4.5c and e recorded after the deposition of C_{60} onto the precursor lattice show individual C_{60} molecules on top of the Ce(TPP)$_2$ island. An analysis of STM images exhibiting submolecular resolution allows us to

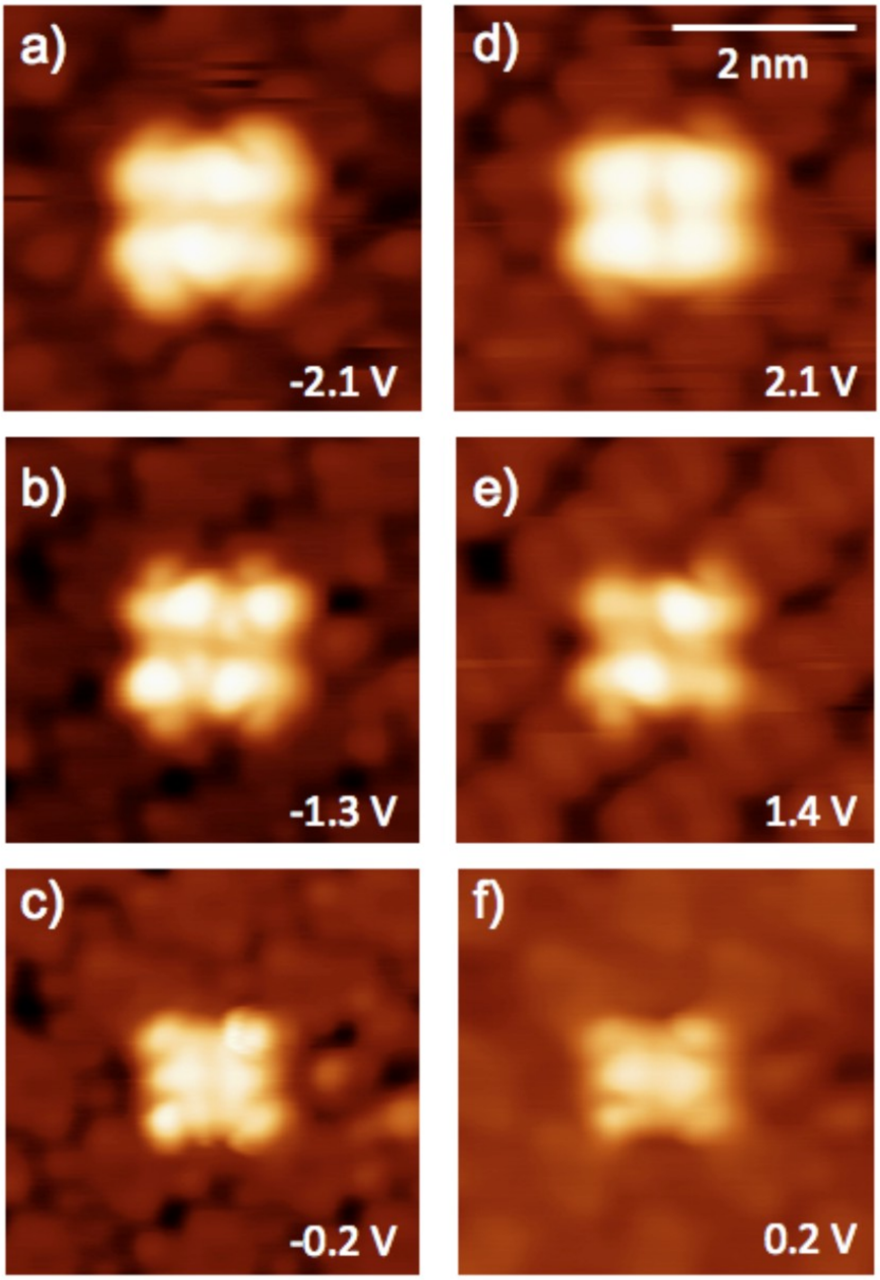

Figure 4.3: Individual Ce(TPP)$_2$ complex seen at various sample bias voltages. The double decker shows a 90° change in the two-lobed central axis at positive and negative biases. 55 x 55 Å^2, I = 0.1 nA.

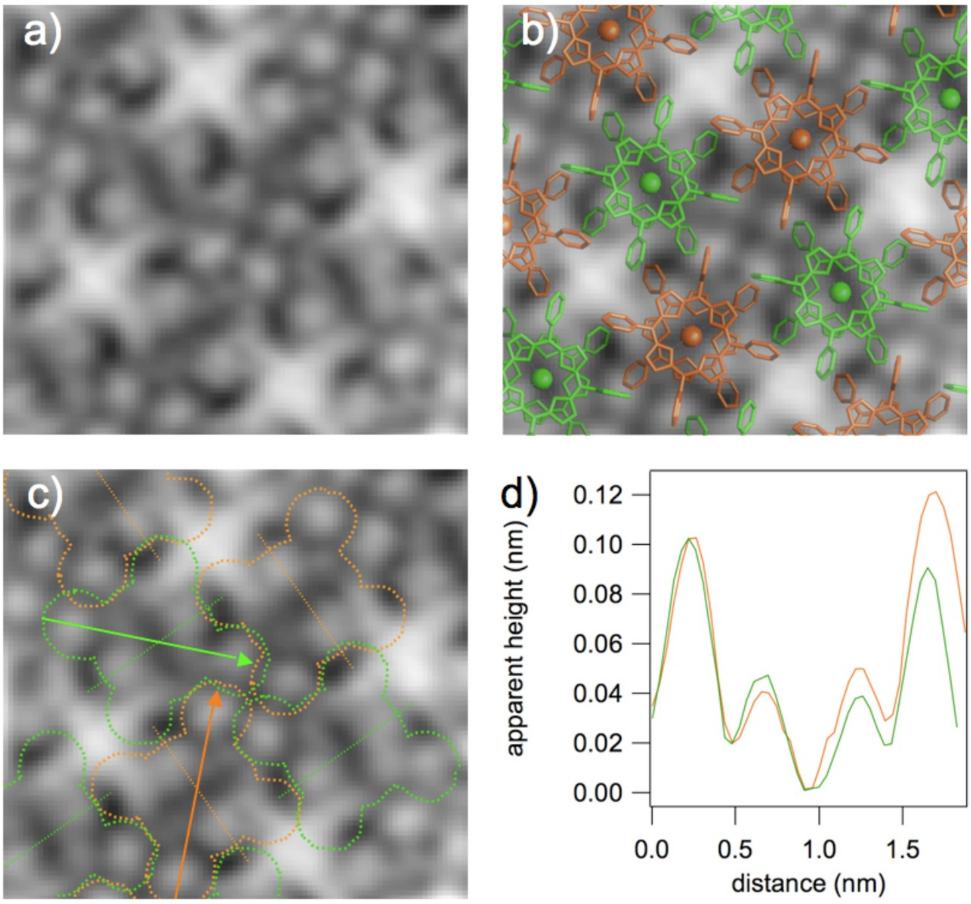

Figure 4.4: a) High-resolution image of a Ce(TPP)$_2$ array on Ag(111) (V_b = 0.3 V). The individual double-decker units (outlined in c) show a rich intramolecular structure. The two-fold appearance of the macrocycle and the contrast of the terminal phenyl groups exhibiting two distinct pairs of lobes agree well with the geometry and symmetry of the Ce(TPP)$_2$ structure optimized by **DFT**. b) **DFT**-based structural models overlaid on the STM image introduced in a). Note the chiral nature of the surface-anchored Ce(TPP)$_2$ units. c) The dashed lines highlight the molecular main axis given by the macrocycle deformation, which yield the two orientations of the top porphyrins (α, green and β, orange). The arrows represent the direction of the height profiles shown in d). Height profiles averaged over six α and β species indicating subtle deviations from a two-fold rotational symmetry in the Ce(TPP)$_2$ complex. We tentatively relate this asymmetry to the two distinguished current levels for the α_1 and α_1 (or β_1 and β_1) configurations reported in the article.

identify the adsorption sites of C$_{60}$ on Ce(TPP)$_2$ and reveals a site-selective attachment: The spherical C$_{60}$ units are almost exclusively (94% out of $>$ 700 molecules) centered above the upper porphyrin of the Ce(TPP)$_2$ complex, regardless of the orientation (α or β) of the subjacent unit (cf. Fig. 4.5c). We can rule out an embedding of C$_{60}$ in the Ce(TPP)$_2$ arrays since the C$_{60}$ could be selectively removed by STM manipulation revealing an unaltered double-decker species underneath. In addition, the apparent height of C$_{60}$ measured with respect to the double-decker is 8.6 Å(at $V_b = 1.8$ V), considerably higher than for C$_{60}$ directly adsorbed on the metal (7 Å), indicating an electronic decoupling (vide infra), thereby confirming the adsorption of the acceptor on the Ce(TPP. Thus, the C$_{60}$ follows the square lattice of the underlying double-decker array (cf. Fig. 4.5e) resulting in a minimal inter-fullerene distance of 13.9 Å clearly exceeding typical C$_{60}$ nearest-neighbor distances of $\sim$ 10 Å on bare metal (vide infra).

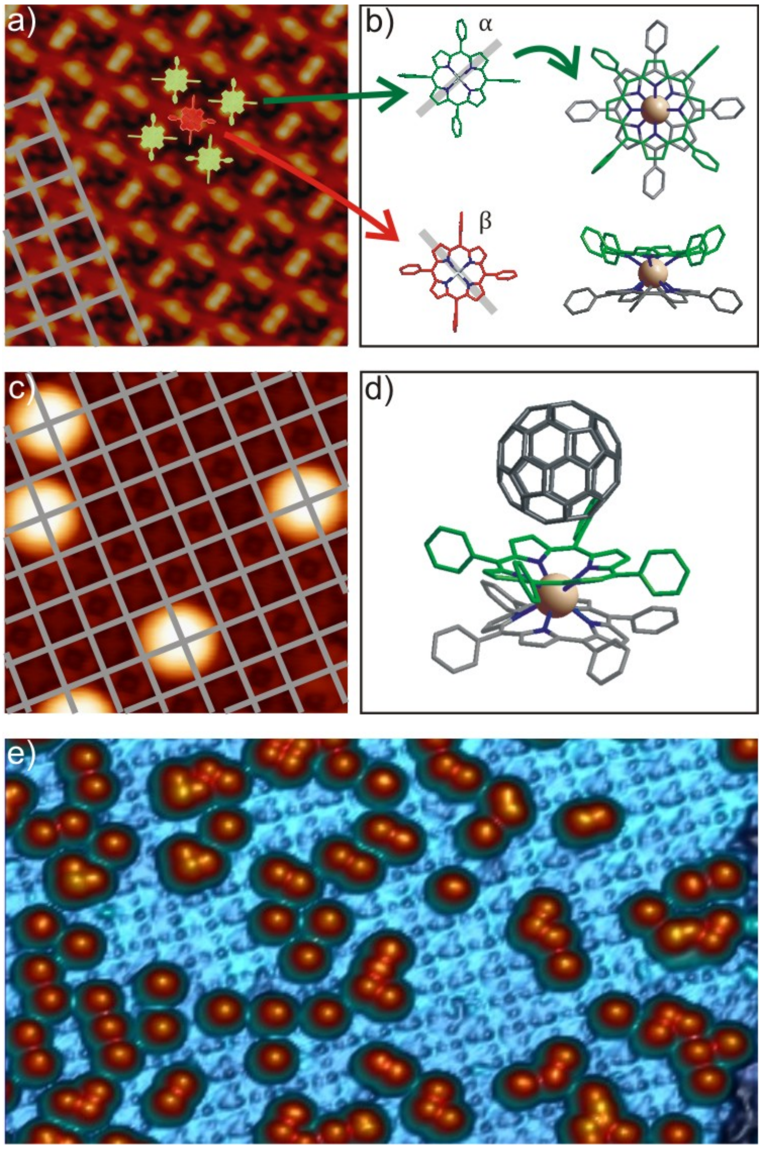

Figure 4.5: Site-selective adsorption of C60 on porphyrin double-deckers. **(a)** STM topograph of a Ce(TPP)$_2$ array on Ag(111). The green and red models represent the two orientations (named α and β) of the non-planar top porphyrin in the Ce(TPP)$_2$. Image size: 110.7 × 110.7 Å^2, Tunneling parameters: $Vb = 0.2$ V, $I = 0.1$ nA. **(b)** Schematic top and side view representation of a Ce(TPP)$_2$ complex obtained from **DFT** calculations visualizing the bowl-shape deformation (see text for discussion). For clarity, the hydrogen atoms are not shown. The top porphyrin of the double-decker is rotated ±45° with respect to the bottom one, resulting in α and β configurations. **(c)** Molecular recognition: The bright protrusions correspond to individual C$_{60}$ molecules on a double-decker array, which is resolved in the background. The superimposed grid represents the centers of the Ce(TPP)$_2$ units. Image size: 110.7 × 110.7 Å^2, $Vb = 1.7$ V, $I = 75$ pA. **(d)** **DFT** based structural model visualizing a C$_{60}$ molecule confined on the bowl-shaped macrocycle of a double-decker. **(e)** Pseudo 3D representation of an STM topograph at higher C$_{60}$ coverage highlighting the influence of the square Ce(TPP)$_2$ lattice on the C$_{60}$ positioning, Image size: Image size: 443 × 266 Å^2, $Vb = 1.7$ V, $I = 30$ pA.

Several recent studies applied templated nanostructures for the organization of fullerenes. [192] [193] [194] [195] [196] [197] [198] Solid-state architectures and assemblies in solution reveal a general attractive interaction between porphyrins and fullerenes, resulting in structures characterized by fullerenes in close face-to-face contact to the porphyrin macrocycle. [171] [172] It is generally agreed that these supramolecular complexes are stabilized by non-covalent bonding between the π systems combined with electrostatic interactions and charge transfer. However, these attractive interactions are not preserved for C_{60} deposited on conventional two-dimensional porphyrin arrays supported on metallic surfaces. [192] Instead of binding to the porphyrin macrocycle, the fullerene species tend to incorporate into mixed porphyrin-C_{60} arrays maximizing the C_{60}-metal interaction and thus hampering the prospects outlined in the introduction. [188] [189] [199] [200] [201] In ultra-high vacuum, the confinement of C_{60} on a tetrapyrrolic macrocycle was only achieved partially by employing a phtalocyanine derivative substituted by bulky terminal groups. [202] Even at solid-liquid interfaces, a face-to-face adsorption of fullerenes on porphyrins is uncommon and was only accomplished by employing open cage C_{60} derivatives, [203] [204] whereas an off-center adsorption of C_{60} was possible on a mixed molecular template. [205]

Here we present a truly site-selective molecular recognition in a solvent free environment where the C_{60} species are positioned on the π conjugated upper porphyrin core of the double-decker complex, thus permitting a direct electronic interaction between the potential donor and the acceptor units. It is important to stress that the face-to-face bonding motif is thermally robust and persists even after annealing at room temperature. Our **DFT** calculations shed some light on the C_{60}/Ce(TPP)$_2$ coupling: Upon binding of the fullerene, the two-fold bowl shape of the Ce(TPP)$_2$ persists and the phenyl groups of the top porphyrin tilt slightly away from the C_{60} (cf. Fig. 4.5d). The resulting binding energy for C_{60} exposing a 6 : 6 bond to the center of the top porphyrin (vide infra) amounts to 1.16 eV and is mainly given by dispersion, i.e. van der Waals interaction. Only minor polarization effects contribute to the binding (cf. Fig 4.6). The calculations confirm that the peculiar concave deformation of the top porphyrin maximizes the $\pi - \pi$ interaction with the convex surface of the C_{60} and promotes the site-selective adsorption and the successful formation of a surface anchored C_{60}/porphyrin dyad. Related shape-complementarity features were recently employed to stabilize fullerenes on corranulene bowls on Cu(110). [206] [207]

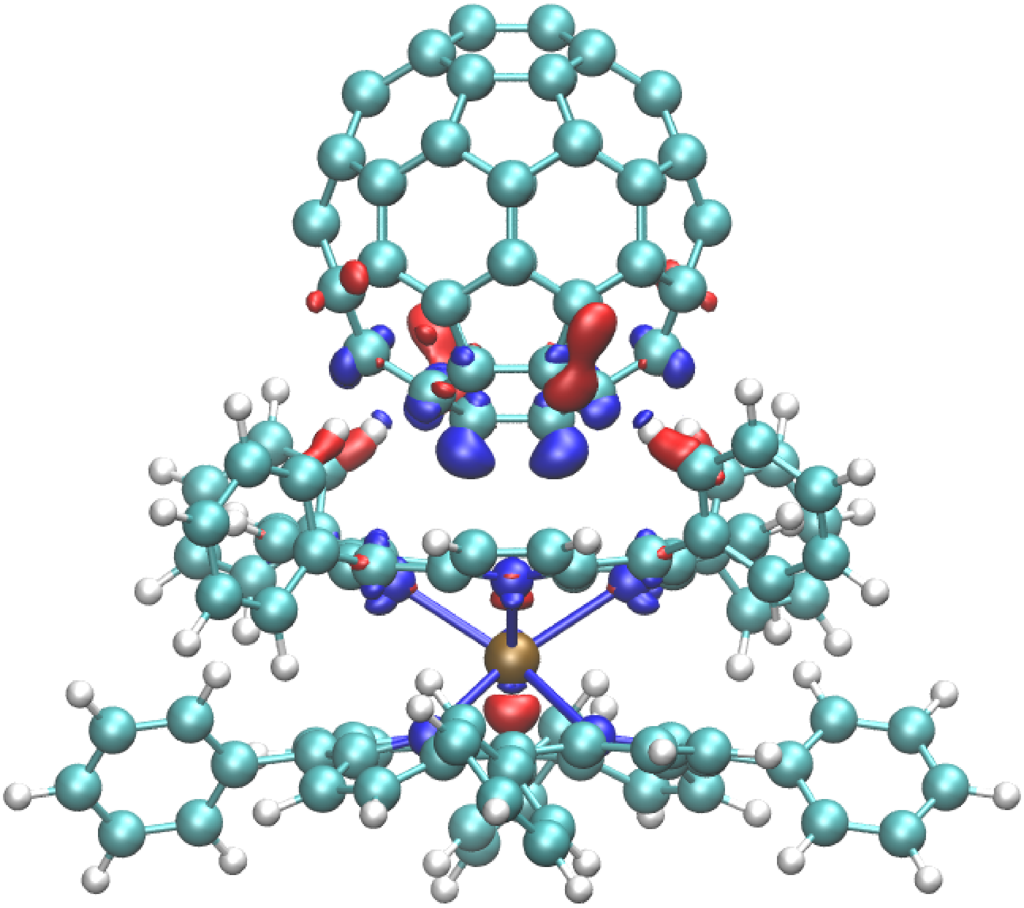

Figure 4.6: Density difference upon binding of C_{60} via 6 : 6 bond to the Ce(TPP)$_2$ complex calculated by **DFT**. Blue color represents electron deficiency and red represents electron accumulation. It should be noted that the integral over the total charge density is about three orders of magnitude larger than the integral over the absolute value of the density difference. Accordingly, polarization effects are weak and covalent interactions can be excluded and the bonding is mainly given by van der Waals forces.

4.3.2 Electronic structure of the dyad

The electronic structure of the Ce(TPP)$_2$ and C$_{60}$/Ce(TPP)$_2$ dyad was probed by **STS**. The peaks shown in the spectra (figure 4.7) reflect the main resonances that contribute to the tunneling current. Figure 4.7 compares a typical dI/dV spectrum of a C$_{60}$ on top of a double-decker complex (red curve) to reference signals recorded on an individual C$_{60}$ molecule in direct contact with the Ag(111) surface (green curve) and a bare Ce(TPP)$_2$ complex (black curve), respectively. The spectrum of the bare Ce(TPP)$_2$ unit is dominated by a strong resonance at 1.8 eV, designated as **LUMO+1** while the **LUMO** occurs at 1.1 V. The first peak in the occupied region is located around -1.2 eV, yielding an apparent gap of ~ 2.3 eV. The spectra of Ce(TPP)$_2$ obtained by the in-situ synthesis is identical to the one obtained by direct sublimation.

The reference spectrum of individual C$_{60}$ molecules on Ag(111) shows two prominent unoccupied resonances (**LUMO** at 0.5 eV and **LUMO+1** at 1.8 eV, respectively) and a **HOMO** close to -1.9 eV, exhibiting a band gap of 2.4 eV. Considering screening shifts, the energetic positions of these frontier orbitals agree well with (inverse) photoemission data of a monolayer of C$_{60}$/Ag(111) [162] and with our spectra taken on an island of C$_{60}$/Ag(111).

Addressing now the spectrum recorded above the C$_{60}$ molecule adsorbed on Ce(TPP)$_2$, drastic modifications are observed. Two specific features evidence a considerable reduction of the coupling of the fullerenes with the metallic substrate mediated by the Ce(TPP)$_2$: (*i*) A sharp spectral feature appears at 1.4 eV in the positive region and is associated with theC$_{60}$ **LUMO** (see below). However no **HOMO** signature could be detected in the accessible bias voltage range suggesting that the **HOMO** resonance is shifted below -2.5 eV. The sharpening of the **LUMO** resonance combined with the increase of the band gap to a value exceeding 3.9 eV indicates a reduced electronic coupling to the surface [208] (the electronic bandgap of a free C$_{60}$ in gas phase being 4.9 eV). [209] In this sense, the screening by image charges in the substrate is reduced, which leads to a larger on-site Hubbard energy due to a higher Coulomb repulsion resulting in an increase of the gap which is apparently not compensated by polarization screening induced in the porphyrin complex. [162] [209] We see additional sidebands separated from the main **LUMO** and **LUMO+1** resonances of the C$_{60}$ (not shown), identifying a free molecule character subject to the dynamic Jahn-Teller effect. [208] (*ii*) We find a pronounced negative differential resistance **(NDR)** regime on the high-energy side of the **LUMO** resonance (1.8 – 2.7 eV, cf. Fig. 4.7) characteristic for molecular systems exhibiting only weak interactions with the substrate. [210] [211] Thus, we tentatively consider these spectral features as a

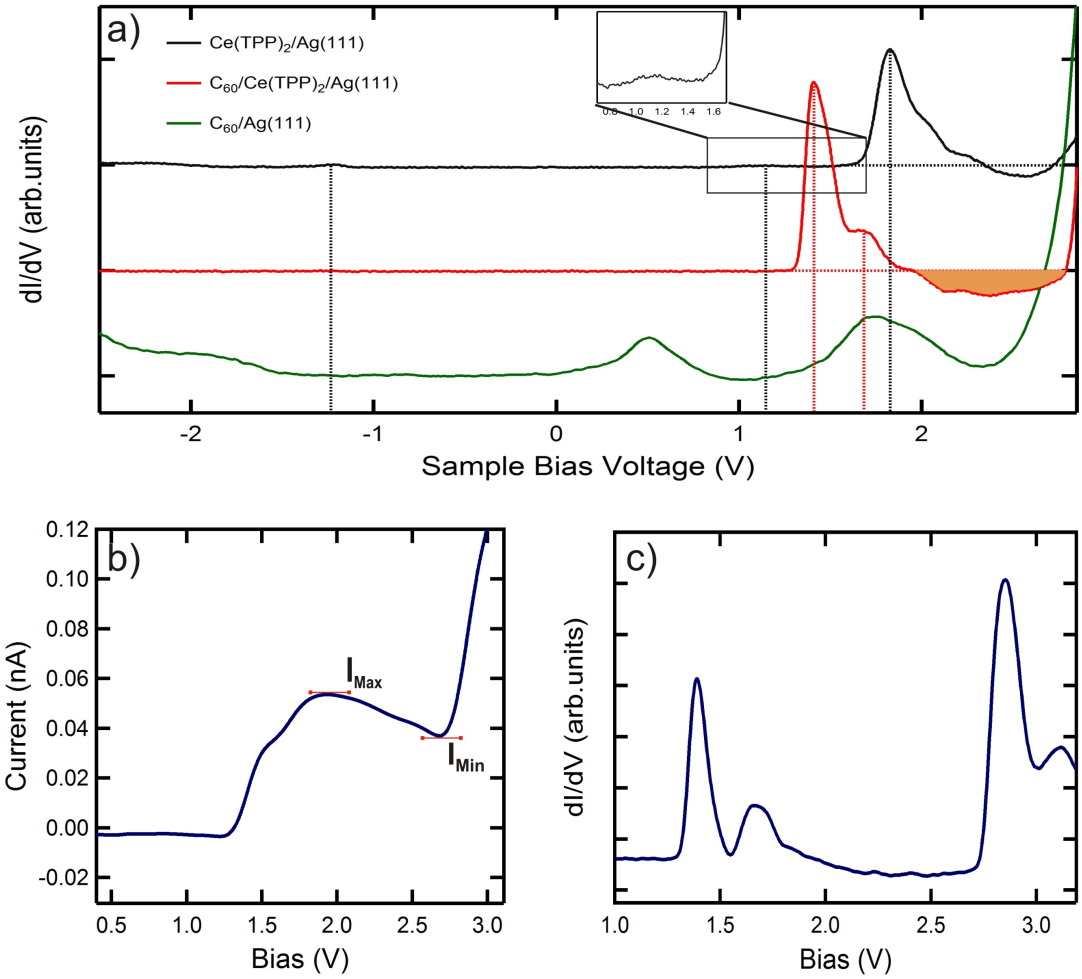

Figure 4.7: a) Electronic structure of the C$_{60}$/Ce(TPP)$_2$ dyad. Probed by **STS**, dI/dV traces recorded on a single C$_{60}$/Ag(111) (green), Ce(TPP)$_2$/Ag(111) (black) and a C$_{60}$ on a Ce(TPP)$_2$/Ag(111) (red). The latter points towards a clearly reduced coupling of the fullerene from the metal substrate, showing narrow resonances, an increase of the **HOMO-LUMO** gap, a fingerprint of the dynamic Jahn-Teller effect and a negative differential resistance regime **(NDR)** shaded in red. b) The IV characteristic of a C$_{60}$ on a Ce(TPP)$_2$ complex at a tunnel junction resistance of 0.19Ω (Tip stabilization: $V_b = 2.9$ V, $I = 0.15$ nA)The ratio of the maximum and minimum peak position gives a current drop of 1.44 c) The LUMO and LUMO+1 peaks of a C$_{60}$ molecule confined on a Ce(TPP)$_2$ complex. Both the peaks evidence side bands attributed to the Jahn-Teller effect (Tip stabilization: $V_b = 3.2$ V, $I = 0.15$ nA, $\Delta V_b = 18$ mV, $f_{Lock-in} = 969$ Hz).

fingerprint of a nearly free-molecule character. It should be noted that the STM tip was characterized before and after all dI/dV and $I(t)$ measurements to exclude the influence of tip modifications: no change in topographic images was detected, which rules out a C$_{60}$ transfer to the tip. In addition, reference spectra on Ag(111) did not reveal any modification before and after the spectra on the molecular system, thereby ensuring an unaltered electronic configuration of the tip.

Our results suggest a potential use of the **D-A** Ce(TPP)$_2$/C$_{60}$ units in photophysical devices for the following reasons: (*i*) The donor double-decker species presents an apparent energy gap of 2.3 eV (540 nm), which suggests a feasible adsorption of light in the visible range in order to generate excitons, provided the transition is dipole allowed. (*ii*) The spectra of the double-decker indicate a reduced coupling with the metallic substrate, which enhances the life-time of the excitons.

4.3.3 C$_{60}$ orientations on Ce(TPP)$_2$

High-resolution STM images reveal information on the precise orientation of the C$_{60}$ cage in space. Addressing first the reference case of C$_{60}$ /Ag(111) after dosage at 120 K, the majority of C$_{60}$ units do not appear as perfect spheres, but exhibit three characteristic lobes when the unoccupied states are probed (cf. Fig. 4.8a). This appearance is well known to represent the 3-fold symmetric shape of the **LUMO** mainly localized on the pentagonal rings when a fullerene adsorbs with a hexagon facing the substrate. [212] [213] [214] Submolecular resolved STM images probing the unoccupied states reveal specific orientations of the C$_{60}$ species centered on Ce(TPP)$_2$, differing from C$_{60}$/Ag(111). For each orientation of the top porphyrin (α or β) three different orientations of the C$_{60}$ can be distinguished (cf. Fig. 4.8b), giving a total number of six orientations represented by double-protrusions symmetric with respect to surface normal and single protrusions appearing off-center, respectively (cf. Fig. 4.8c,d). Again, these intramolecular features stem from the **LUMO** states of the fullerene mainly residing on the C$_{60}$ pentagons. [21] By comparing STM images and extended Hückel theory **(EHT)** simulations based on various orientations of an isolated C$_{60}$ cage, [194] we conclude that C$_{60}$ exposes either a C-C bond at the $6:6$ ring juncture (labeled 6:6 bond, cf. Fig. 4.8c,d top panel) or an apex atom (cf. Figure 8c,d medium and bottom panel) to the porphyrin center (and thus to vacuum). As summarized in Fig. 8, the $6-6$ bond configurations correspond to the double-protrusions in the STM images and the apex adsorption yields the off-center protrusion. The excellent agreement between the **EHT** calculation based on the **LUMO** charge density of a free C$_{60}$ with the experimental STM topographs recorded at voltages above 1.4 V confirms the identification of the unoccupied spectral feature in the C_{60}/Ce(TPP)$_2$ spectrum with the fully degenerate **LUMO** (cf. Fig. 4.7a).

Clearly, the macrocycle deformation accounting for the α or β species guides the C_{60} adsorption on the Ce(TPP)$_2$. The 6 : 6 bond is aligned with the main axis of the top porphyrin, yielding orientations differing by 90° for α and β units, respectively. Analogously, the pentagon corresponding to the apex atom can be displaced to either side of the main axis for both α and β species, resulting in four distinct configurations to be named apex α_1 (β_1) and apex α_2 (β_2) . A detailed statistical analysis shows a population of 22.8 ± 3 % for the α_1 orientation, 21.73 % for β_1, of 20.93 % for the α_2 and β_2 and of 14.3 ± 3 % for the 6 : 6 orientation (identically populated on both orientations of the double-decker). Thus, all apex configurations are equiprobable and show a slight statistical preference over the 6 : 6 orientations. In porphyrin-fullerene crystal structures a close alignment of a 6 : 6 bond with a trans **N**$\cdots$**N** vector and therefore the main axis of the porphyrin macrocycle is a well established structural motif guiding the supramolecular interactions. [172] [181] [215] For the C_{60}/Ce(TPP)$_2$ dyad, this 6 : 6 bond adsorption geometry is regularly observed but judging from the above statistics is energetically less favored than the apex configurations.

The **DFT** calculations however yield a binding energy of 1.16 eV for the 6 : 6 configuration and 1.09 eV for the apex orientation. Given the small energy difference between the two observed configurations and considering the simplification the **DFT** results are based on (exclusion of the metallic substrate, restriction to a fixed macrocycle alignement) the calculated preference for the 6:6 configuration is not conclusive. **DFT** calculations further confirms that the interaction between Ce(TPP)$_2$ and C_{60} is non-covalent. Figure 4.6 shows a density difference after the adsorption of C_{60} on the double decker. It is seen that the electron deficiency and electron accumulation is considerably small indicating a minimal charge transfer between the C_{60} and Ce(TPP)$_2$

4.3.4 Tuning the intermolecular coupling by a switching mechanism:

The reported distinct bonding configurations of C_{60} on the porphyrin double-deckers point to an interaction sensitive to the non-uniform charge distribution in both entities and reflect the symmetry and distortion of the upper porphyrin ligand. [181]

The stereochemical interaction of the C_{60} cage with the porphyrin macrocycle results in preferred geometrical alignments within the C_{60}/Ce(TPP)$_2$ dyad, i.e., the intermolecular coupling is guided by the relative orientation of the two constituents. Controlling the orientation of the C_{60} cage on the double-decker opens the opportunity to tune the coupling in the dyad. Therefore, we now address the deliberate rotation of C_{60} on Ce(TPP)$_2$ via controlled stimulation using an atomically sharp STM tip.

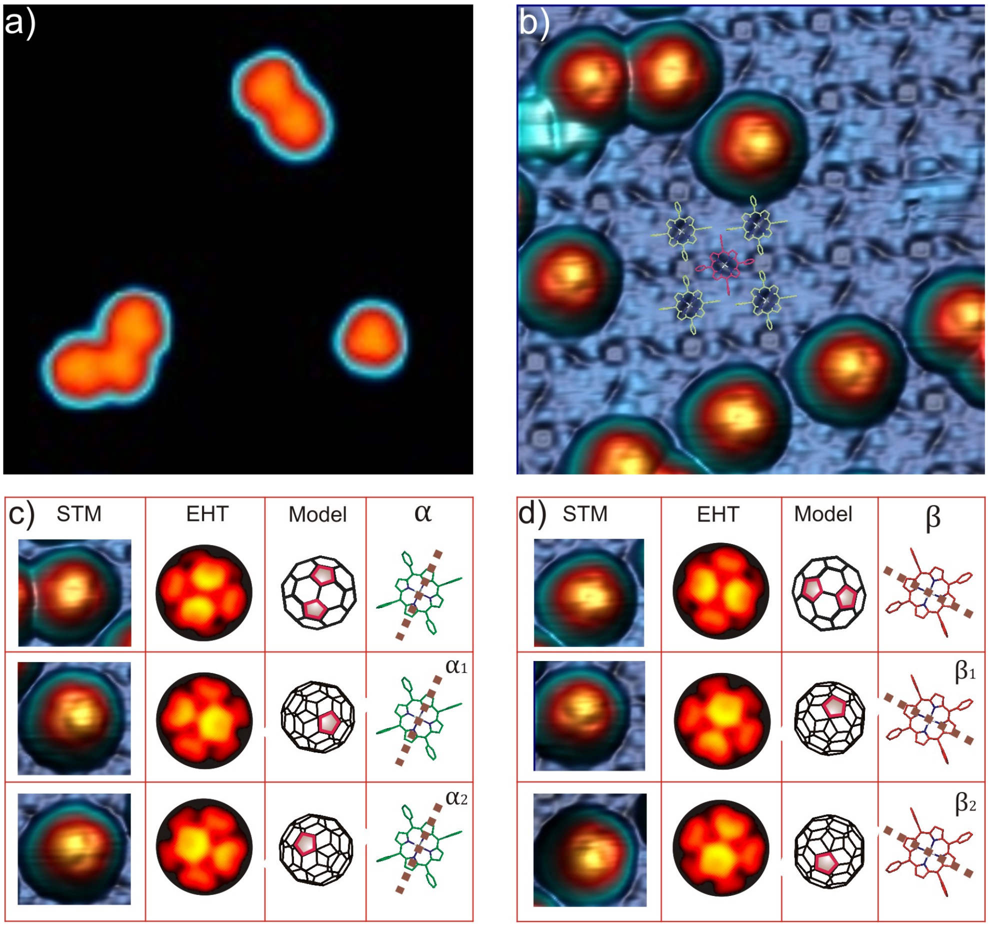

Bgraph3

Figure 4.8: C_{60} orientations on Ce(TPP)$_2$. **(a)** On Ag(111), the C_{60} molecules expose a hexagon to the substrate and are thus visualized with a three-lobe structure when the unoccupied states are probed. Image size: 110.7×110.7 Å^2, $Vb = 1.7$ V, $I = 0.1$ nA. **(b)** A pseudo 3D view of an STM image of C_{60} on Ce(TPP)$_2$ showing distinct orientations of the C_{60} units on the double-decker array. A model of the Ce(TPP)$_2$ unit cell is superimposed, depicting the α (green) and β orientation (red) of the top porphyrin moiety, respectively. Image size: 110.7×110.7 Å^2. $Vb = 1.8$ V, $I = 70$ pA. **(c)** The first column shows STM images of the three possible orientations of the C_{60} on an α-Ce(TPP)$_2$ complex. The middle column represents extended Hückel simulations of the **LUMO** of C_{60} oriented to match the STM image (see text for discussion). The third column schematically shows the C_{60} orientation according to the experimental and simulated images and relates it to the symmetry axis of the α-Ce(TPP)$_2$ (shown in the fourth column). **(d)** Analogy to **(c)**, but displaying the C_{60} on a β-Ce(TPP)$_2$ complex (rotated 90° with respect to the α-Ce(TPP)$_2$ species).

A tunneling current applying a positive sample voltage exceeding a threshold of 1.8 V drives reversible switching between any of the previously discussed C_{60} orientations. Below this bias threshold, the C_{60}/Ce(TPP)$_2$ dyad can be imaged stably, guaranteeing a reliable read-out of the C_{60} orientation. An inspection of the STM images before and after switching reveals that the rocking motion occurs without any detectable lateral [216] translation of the C_{60}, remaining confined at the center of the porphyrin for both α and β species. The dynamic process is not a simple azimuthal rotation of the C_{60} around a symmetry axis perpendicular to the surface, but involves a polar angle, i.e., a second rotation axis in the equatorial plane. This free rotation in space is exemplified in the transition from a 6 : 6 bond to an apex configuration. It can proceed via a rotation by a polar angle of $\pm 77°$ around an in-plane axis aligned with the main axis of the porphyrin macrocycle (cf. dashed lines in Fig. 4.5b and 4.8c) or by a combination of polar and azimuthal angles.

To gain further insight into the rocking process [217] we record the tunneling current I versus the time t. To this end, the tip is centered above a C_{60} and the feedback loop is opened. A typical $I(t)$ trace as displayed in Fig. 4.9b clearly reveals a switching between three well-separated current levels, representing high, medium and low conductance states. Within the time resolution of the STM experiment, the transition between the states is abrupt. The absence of such switching events on Ce(TPP)$_2$ arrays demonstrate that the effect is related to C_{60}. By comparing the initial and final current levels in the I(t) traces to STM images recorded before and after many manipulation sequences, we unambiguously can assign the current levels to specific C_{60} orientations. For each porphyrin species (α or β), the high conductance state represents the apex α_2 (β_2) orientation, the medium conductance state is attributed to the apex configuration α_1 (β_1), while the low conductance state corresponds to the 6 : 6 bond coupling. Herein, the low-conductance in the 6 : 6 configuration could originate in a topographic effect given by the central depression observed in the STM images. However, the different current levels for α_1 and α_2 (or β_1 and β_2, respectively), which represent perfectly symmetric configurations when only considering the C_{60} unit, reveal the influence of the C_{60}/Ce(TPP)$_2$ coupling. The asymmetry in the double-decker structure discussed previously, seems to influence the electric contacts and thus the coupling in the junction. Indeed, the configurations exhibiting a high and medium conductance (α_2, β_2 and α_1, β_1, respectively) are observed more frequently than the 6 : 6 state with the lowest conductance.

Thus, the C_{60} on Ce(TPP)$_2$ behaves as a tri-stable system controllable by STM manipulation. The induced rotations of the C_{60} cage in space affects the intra-dyad coupling. Consequently, these results demonstrate for the first time deliberate reversible modifications within a surface anchored van der Waals complex.

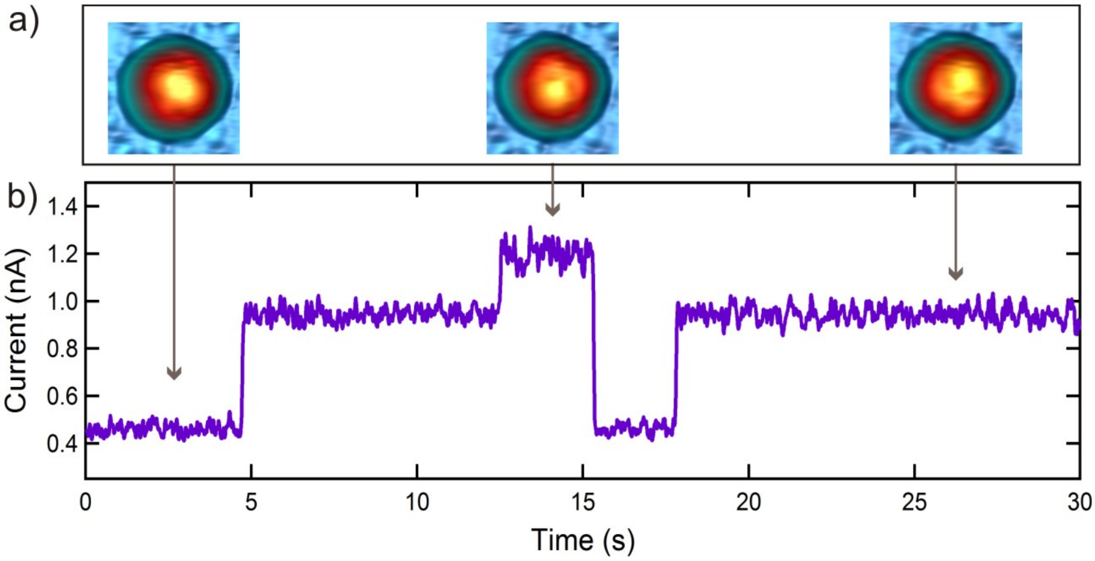

Figure 4.9: C_{60}/Ce(TPP)$_2$ dyad as an electronic tri-stable system. **(a)** Orientational switching of C_{60} adsorbed on an β-Ce(TPP)$_2$ complex. The STM images represent three configurations of the very same C_{60} molecule. **(b)** Tunneling current measured versus time above a C_{60}/Ce(TPP)$_2$ complex under open feedback loop at 2.2 V. Three different levels of conductance are distinguished: each level is attributed to one orientation of the C_{60}. The highest level of conductance is assigned to an β_2 apex orientation, the adjacent one to the β_1 apex configuration and the lowest level of conductance represents the 6 : 6 bond orientation.

4.4 Annealing the C_{60}-Ce(TPP)$_2$ arrays-phase β

4.4.1 Structural overview

The C_{60}s confined individually on the Ce(TPP)$_2$ complexes were characterized topographically and electronically. However when the sample was thermally annealed at room temperature, a new arrangement of C_{60} in well-ordered arrays was observed, designated as phase β. In this phase, the C_{60}s clustered together to form a dense packed bi-layer arrangement on top of the Ce(TPP)$_2$ island. (figure 4.10)

The agglomeration of C_{60} was observed to nucleate from individual Ce$_2$(TPP)$_3$ molecules embedded on the double decker island, resulting in large, extended islands of more than 200 Å. The position and arrangement of the C_{60}s were characterized from these extended islands. (figure 4.10).

In figure 4.10a, the red background corresponds to the dense packed Ce(TPP)$_2$ assembly. The bright islands on top of the red background correspond to the clustered C_{60} islands. The C_{60} islands have sharp edges since they strictly follow the underlying Ce(TPP)$_2$ grid. Regarding the extended C_{60} islands, only one layer of C_{60}s is visible upon initial observation. However on closer inspection, the C_{60} islands were

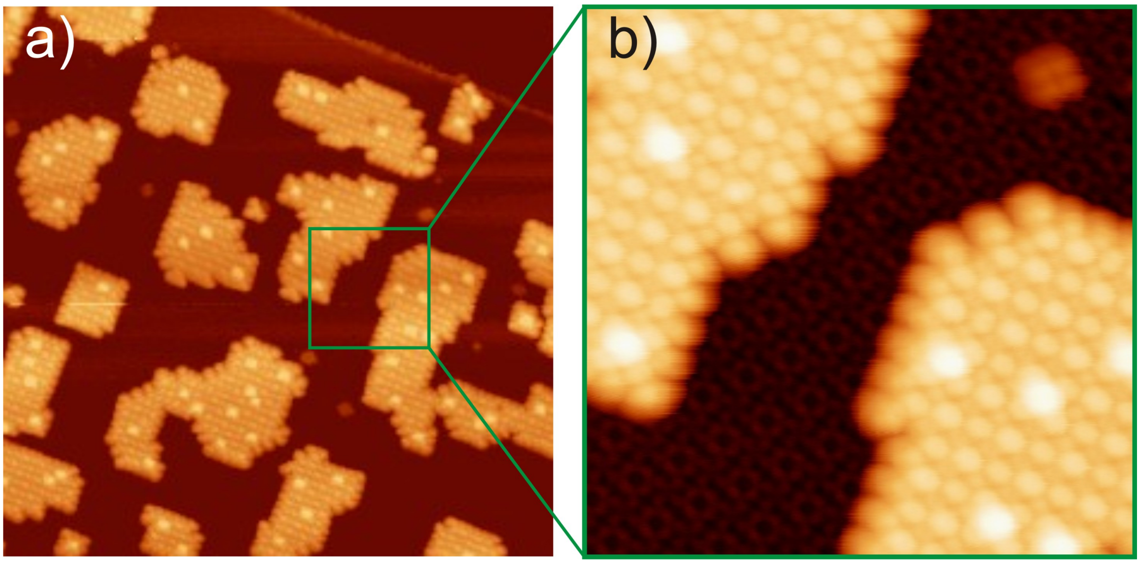

Figure 4.10: a) Long range STM image showing arrays of C_{60} (yellow patches) adsorbed on a uniform layer of Ce(TPP)$_2$ (red background layer). The nucleation of C_{60} growth starts form a Ce$_2$(TPP)$_3$ molecule embedded in a double decker island. Ordered lobes are visible on the C_{60} island, which correspond to individual C_{60}s of the second layer. The intermolecular distance of the molecules in the second layer correspond to 13.9 Å. (Parameters: 850×850 Å^2, $V_b = 2.2$ V, $I = 0.02$ nA) b) Zoom-in of C_{60} island from a). The C_{60}s in the top layer evidence a non-circular appearance. The C_{60}s in the bottom layer are visible in between the elliptical top layer C_{60}s. The orientation of the bottom layer of C_{60}s is not visible. (Parameters: 220.6×220.6 Å^2, $V_b = 2.2$ V, $I = 0.03$ nA)

seen to be composed of an interesting arrangement. The arrangement consists of two layers of C_{60} stacked on top of each other. The first layer lies close to the Ce(TPP)$_2$ complex as in the case of an individual C_{60} and forms an ordered grid. The second layer lies in the gaps formed by the first layer. This bi-layer arrangement of the C_{60}s is clarified based on the following arguments:

- In a **high resolution STM image**, a missing C_{60} in the ordered array shows both the top and bottom layers at different brightness. [Figure 4.11]
- A clear variation is **apparent height** in observed for the C_{60} in the top and bottom layers. The average apparent height of the top layer C_{60}s is ~ 9.7 Å. and the bottom layer C_{60}s is ~ 8.5 Å. [Figure 4.12]
- **STS data** reveals a difference in the positioning of the LUMO resonance for the top and bottom layer C_{60}. [figure 4.13]

The islands of C_{60} observed in (figure 4.10a,b) has certain distinct characteristics like uniform spatial separation, a non-spherical appearance and ordering in arrangement similar to bulk C_{60} crystals. Monolayer C_{60} on a metal substrate assemble into a single layer dense packed hexagonal structure with an intermolecular distance of ~ 1 nm. Multilayer C_{60}s resemble crystalline bulk or *fullerite* with an *fcc* close-packed structure with a lattice constant of 14.17 Å. [218] [219] In the present case, the islands observed on the double decker layer consisted of two layers of C_{60} stacked with different apparent heights in a zig-zag fashion (i.e. a plane passing through the centers of C_{60} on each layer would be parallel to each other with a separation less than the van der Waals diameter of a C_{60} - 1 nm). The arrangement of the first layer of the C_{60} is presumably similar to the the individually confined C_{60}s. In the bottom layer molecules, an intermolecular separation of 13.9 Å was observed which corresponds to the intermolecular distance of the Ce(TPP)$_2$ in a dense packed island. This means that each of the C_{60}s in the bottom layer is confined directly on top of the double decker compound, as in the case of an individual C_{60}. It is interesting to note that the individual C_{60}s which could not be translated by lateral manipulation with the tip, forms highly regular arrays when a soft annealing at room temperature is carried out.

The bi-layer arrangement of the C_{60} is visible in a high-resolution STM image where one C_{60} in the top layer is missing thereby revealing C_{60}s in the bottom layer. [see Figure 4.11a,b]. The second layer of C_{60} was found to be adsorbed in the gaps formed by the first layer molecules, where each C_{60} on the second layer is surrounded by four neighbors of the first (bottom) layer C_{60}s. Consequently the intermolecular distance of the second layer also amounts to 13.9 Å. [Figure4.11d]

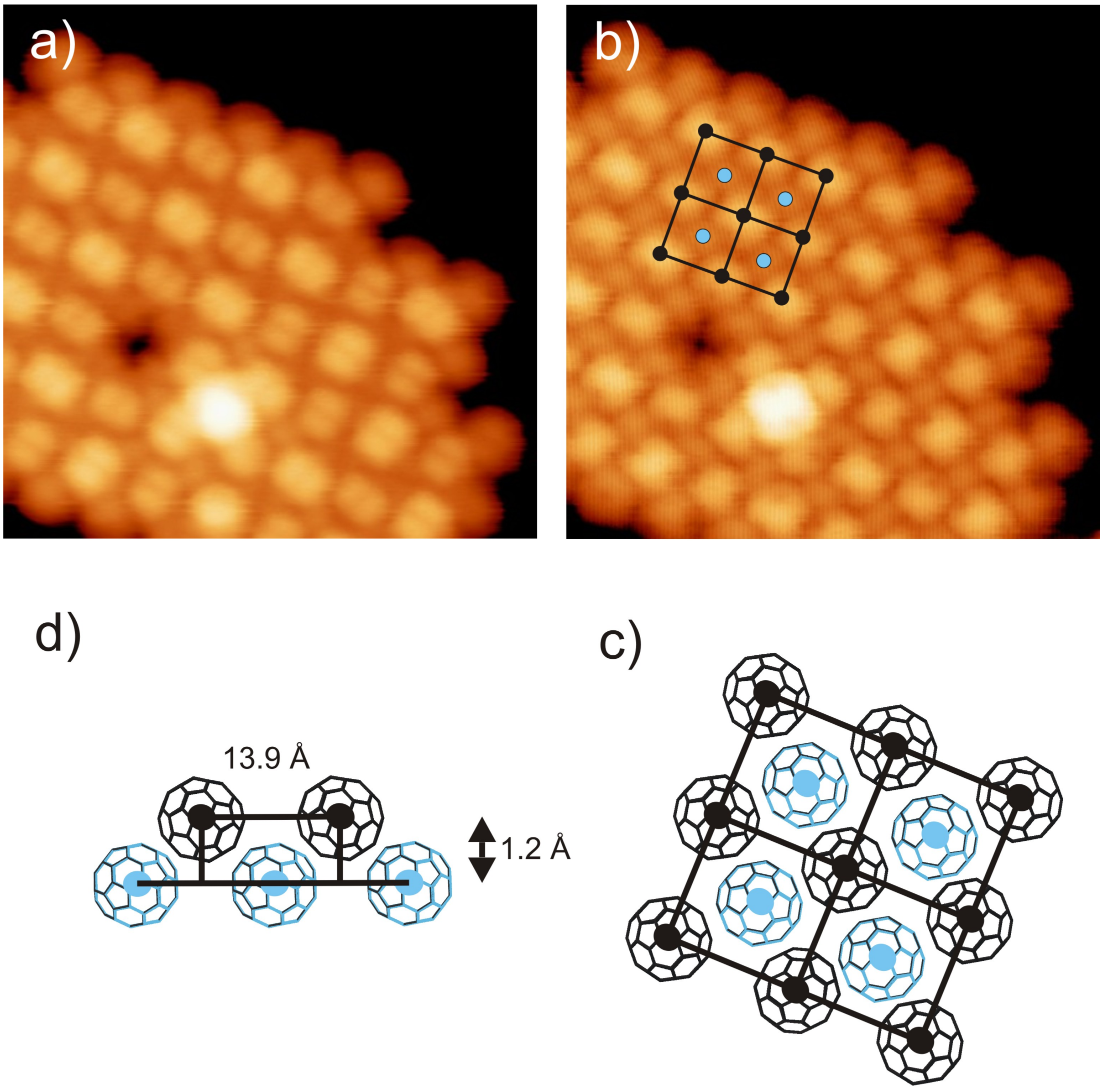

Figure 4.11: a) STM image revealing the two-fold symmetry of the C_{60}s in the top layer of phase β. The top layer molecules reveal two different contrasts, presumably due to a difference in arrangement. The hole in the island denotes a missing C_{60} from the top layer. (Parameters: 110.7×110.7 Å^2, $V_b = 2.5$ V, $I = 0.05$ nA). b) STM image similar to a) taken at a different bias voltage, where the bottom layer C_{60}s are clearly visible. The imposed grid shows the position of the top (black) and bottom (blue) C_{60}s (Parameters: 110.7×110.7 Å^2, $V_b = -3.2$ V, $I = 0.02$ nA). c) The expected arrangement of C_{60}s in the confined arrays. The black and blue C_{60}s correspond to the top and bottom layers respectively. d) A side view schematic of the bilayer C_{60} arrangement confined on the double decker islands.

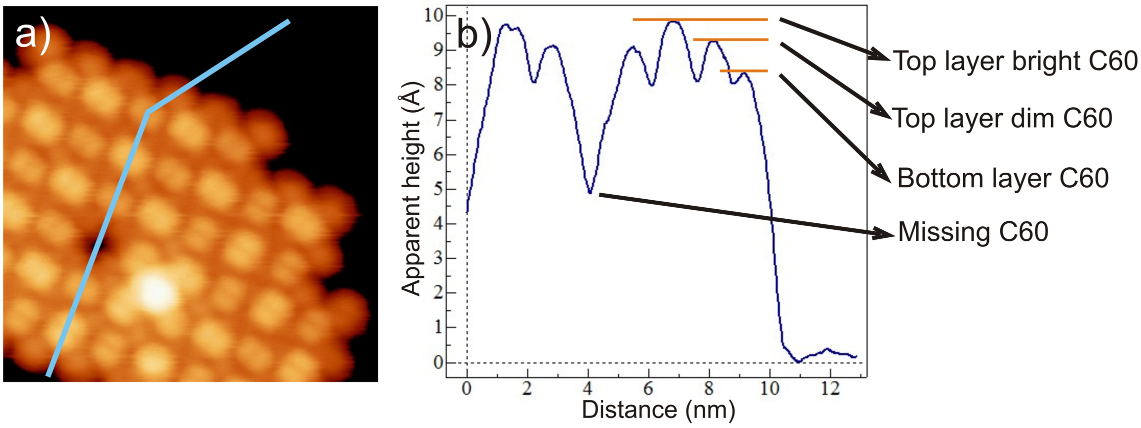

Figure 4.12: A profile of the apparent height is shown in b) corresponding to the STM image in a). The profile shows the apparent height of the top and bottom layer C_{60}s. Image parameters in a): 110.7×110.7 Å^2, $V_b = -3.2$ V, $I = 0.02$ nA

Regarding the appearance of the C_{60}s, the molecules in the top layer evidence a distinct two-fold symmetry when scanned at a bias voltage of ~ 2.5 V. [Figure 4.11a] This two-fold orientation is similar to the 6 : 6 bond orientation of the C_{60}s individually confined on the double decker complex. A similar orientation has also been noted on a metal, where the C_{60}s were adsorbed on a missing adatom position, as observed on Ag(111). [214] Even though the distribution of orientation of the two-fold symmetry is unpredictable, only two orientations are observed: two orientations perpendicular to each other. Since the top layer C_{60}s are well isolated from the Ce(TPP)$_2$ molecules, the influence of Ce(TPP)$_2$ on these orientations are expected to be minimal. The orientations occur when a 6 : 6 bond of the C_{60} faces the surface. Consequently this configuration would expose 6 : 6 bond to the vacuum, with two pentagons on either side. The two-fold contrast arises when probing the unoccupied states localized at these two pentagons. A switch in orientation as in the case of a single molecule was not observed.

Interestingly, the molecules in the top layer appear in two different contrasts: a brighter and a dimmer molecule arranged in alternate fashion. (Figure 4.11a) Even though no specific topographic difference or distortion in two-fold symmetry was observed between the two contrasts, both the bright and the dim species of the C_{60} show a slight variation in apparent height: The bright molecules had an apparent height of 9.8 Å and the dimmer ones, 9.4 Å. [Figure 4.12] The apparent height of the C_{60}s in the bottom layer was observed to be 8.5 Å and at the edge of the island to be 8.8 Å, i.e. lesser than both the bright and the dim species. No other contrast was observed apart from the two mentioned. The apparent heights were measured with respect to the double decker island.

The orientation of the molecules in the first layer adsorbed close to the Ce(TPP)$_2$ complex could not be determined.

4.4.2 Electronic structure

The electronic structure of the C_{60}s on the top and bottom layers of the C_{60} islands was probed by **STS**. Interestingly the spectra observed for the molecules embedded in both the layers evidenced huge differences. A typical spectra of the C_{60}s in the top and the bottom layer is shown in Figure 4.13 (black, blue and red spectra). When the bottom layer of the C_{60} was probed, the unoccupied regime is dominated by a large peak at 1.2 eV (red spectra). This value for the bottom layer C_{60} is lower than the resonance observed for an isolated C_{60} on the Ce(TPP)$_2$ assembly (orange dotted spectra). For an individual C_{60} adsorbed on a double decker, the first unoccupied resonance was observed at 1.4 eV. This observable energy shift of 0.2 eV could be attributed to the enhanced screening effects from to the neighboring C_{60} molecules which was absent for an individual molecule. Such screening effects have been observed before and a shift of more than 400 meV was observed between the spectra of isolated and agglomerated C_{60}s on Au(111). The number of molecular neighbors determine the amount of screening. [161] A sideband is observed at ~ 1.4 eV as in the case of an isolated C_{60}, which is attributed the to the dynamic *Jahn-Teller* effect.

The dI/dV spectrum of C_{60}s in the top layer (See black and blue spectra in Figure 4.13) showed considerable variations in comparison to the C_{60}s in the bottom layer. As mentioned before, the C_{60}s in the top layer comprises of molecules of two different contrasts. Each of the contrasts evidenced variations in the respective **LUMO** positions. The brighter species evidences a peak at 0.9 eV and the dimmer ones at 1.02 eV. This variation in energy arises presumably due to a slight difference in positioning of the bright and the dim C_{60}s. The difference in positioning could be a consequence of different orientations of the first layer C_{60}s. This difference in positioning could also be a reason for the contrast variation that we observe. When compared to an isolated C_{60} on Ce(TPP)$_2$ (orange dotted spectra), the **LUMO** resonance of the bright and dim C_{60}s is shifted by 490 meV and 390 meV respectively towards the Fermi level, from the individual C_{60}s. The bottom layer C_{60}s have a shift of 210 meV from the individual C_{60} resonance. As the number of molecular neighbors increase, it was shown that the **LUMO** resonance of the C_{60}s shifts closer towards the Fermi due to screening effects. [161] But in the present case, a variation in the pattern of screening is observed . A C_{60} in the top layer has 4 C_{60} neighbors

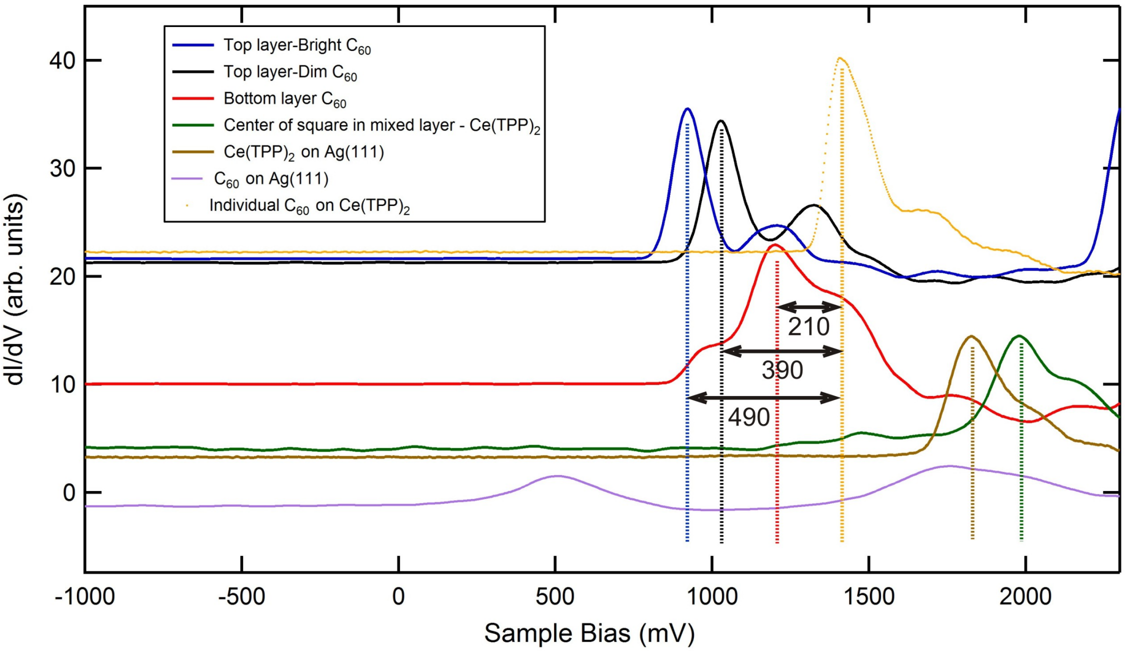

Figure 4.13: Electronic structure of the top and bottom layer C_{60}s in the dense packed C_{60} bi-layer arrangement, phase β. The bright and dim species in the island are depicted in blue and black respectively. A resonance shift is observed between the bright and dim C_{60}s in the unoccupied regime. The bright and dim species are shifted by 0.39 eV and 0.49 eV respectively from the unoccupied resonance of an individual C_{60} on Ce(TPP)$_2$ (orange dotted line). For the C_{60} in the bottom layer (red), the unoccupied region is dominated by a large peak around 1.2 eV, which is lesser than for an individual confined C_{60} (1.4 eV). The reduction in the **LUMO** values indicate higher screening charges due to a higher number of neighboring atoms. The C_{60} spectra in both layer show side bands close to the **LUMO** resonance and a **NDR** regime. Regarding phase γ, the spectra at the center of the C_{60} square (green spectra) is resembles a Ce(TPP)$_2$ spectra (brown spectra). However a shift of ~ 0.2 eV is observed between the free Ce(TPP)$_2$ spectra and the one in phase γ. A spectra of C_{60} on Ag(111) is shown for reference (violet spectra). (Tip stabilization: $V_b = 2.6$ V, $I = 0.2$ nA)

from the bottom layer. A C_{60} in the bottom layer has 4 C_{60} neighbors from the top layer and an additional Ce(TPP)$_2$ neighbor on which it is confined. Therefore a bottom layer C_{60}, which has one neighbor more than a C_{60} in the top layer should experience more screening and hence a bigger shift in the **LUMO** position. However, this is not the case in the present scenario. The top layer C_{60}s show more screening spectroscopically than the bottom one. The reason for this unexpected shift is still unclear. further, the interpretation of the spectra in phase β is not straight forward as explained in the following paragraph.

An isolated C_{60} molecule has a **HOMO-LUMO** gap of 4.9 eV in gas phase. When the fullerene is located in a molecular crystal, the molecular states overlap and the mobile charge careers in the local neighborhood screen the local charge added to or removed from the fullerene by rearranging their distribution. This screening is also largely dependent on the polarizable character of the neighborhood. The final result is a gap that is much reduced from the individual molecule case. Upon adsorption on a surface, the band gap of an isolated C_{60} is reduced still further due to the charge redistribution at the metal-molecule interface. However when the molecule is adsorbed on another host molecule like Ce(TPP)$_2$, the substrate's influence on the molecule is lessened and the screening at the metal-molecule interface is also reduced which again increases the band gap. [161] At this point when more C_{60} neighbors are introduced to the individual C_{60} (as in phase β), overlapping of molecular orbitals and screening by charge carriers occur and this reduces the band gap. Considering all this processes, we can imagine that the interpretation of the C_{60} spectra becomes complicated in the presence of more neighbors, since it is difficult to determine the magnitude of influence exerted by each neighbor. We can say that the spectra of the C_{60} in phase β is reduced from the one is phase α due to the neighbors, but the amount of reduction is difficult to conclude.

A negative differential resistance **NDR** regime is observed for the C_{60}s in both layers of phase β. This indicates that both the layers evidence a double barrier junction (which is the reason for the **NDR**) and are detached from the substrate's influence as evidenced for an isolated C_{60}. Changing the height of one of the barriers by changing the tip-sample distance did not result in any noticeable voltage drop and consequently no noticeable shift in the spectra. This would mean that the shift in the unoccupied resonances between the spectra of the two C_{60} layers could not be explained due to the variation in the barrier height.

4.5 Higher annealing - phase γ

When the sample containing C_{60}s on the double decker complexes was annealed to an even higher temperature of $\sim$ 493 K, the bi-layer structure of the C_{60} disappears and a new mixed structure of C_{60} - Ce(TPP)$_2$ is observed, named as phase γ. (figure 4.14a) The new structure evidences an intricate assembly of C_{60}s arranged around equally spaced Ce(TPP)$_2$ complexes with C_{60}s having a nearest C_{60} at a distance of 1.1 nm as observed on a metal. In this arrangement, each Ce(TPP)$_2$ complex is surrounded by 8 C_{60} molecules making a square pattern with the center being occupied by the Ce(TPP)$_2$ complex. The C_{60}s in this structure show the well known three-fold symmetrical appearance, which indicates that the C_{60}s are placed directly in contact with the substrate in contrast to the previously mentioned C_{60} array. This was further confirmed by apparent height and spectroscopic measurements. The apparent height of C_{60}s in this structure was measured to be 6.9 Å at a sample bias of $V_b = 1.8$ V.

The Ce(TPP)$_2$ molecules lie at the center of the square grid created by the 8 C_{60} molecules, [Figure 4.14c,d] also as understood by spectroscopic measurements (vide infra). The exact conformation of the double deckers lying in the center of the grid is not identified but we can identify the orientation of the double decker at certain bias voltages. Figure 4.14c clearly shows the orientation and the phenyl legs of the double decker complex at $V_b = -1.9$ V. From the in-situ prepared double deckers, the top porphyrin was observed to be rotated to $\sim \pm 45°$ in the dense packed islands and a $\sim \pm 15°$ in the isolated complexes, with respect to the bottom porphyrin. If the double deckers have the same geometry as on the dense packed layer (i.e.$\sim \pm 45°$), the C_{60}s cannot arrange into a square like pattern around a Ce(TPP)$_2$ complex due to the proximity of the C_{60} to the phenyl legs of the porphyrin. However no distortion in the square-like arrangement of C_{60}s was observed. Therefore a rotational deviation of the TPP ligands in the Ce(TPP)$_2$ complex is likely to occur in order to stabilize the structure.

The **STS** data at the center of the square created by the C_{60}s resemble closely to a double decker species, evidencing a **LUMO+1** peak at $\sim$ 2 eV. [brown and green spectra in Figure 4.13] Hence the role of any broken double decker species or free base porphyrin playing a role in inducing this square like arrangement of the C_{60}s is improbable. However for the confined double decker, a shift is observed in the dominating resonance in the unoccupied regime (green spectra), in comparison to the spectra of a double decker on the Ag(111) substrate (brown spectra). The spectra of a confined Ce(TPP)$_2$ shows a large **LUMO+1** peak at $\sim$ 2 eV while the Ce(TPP)$_2$ on Ag(111) has a similar peak at $\sim$ 1.8 eV. This shift could be attributed to the

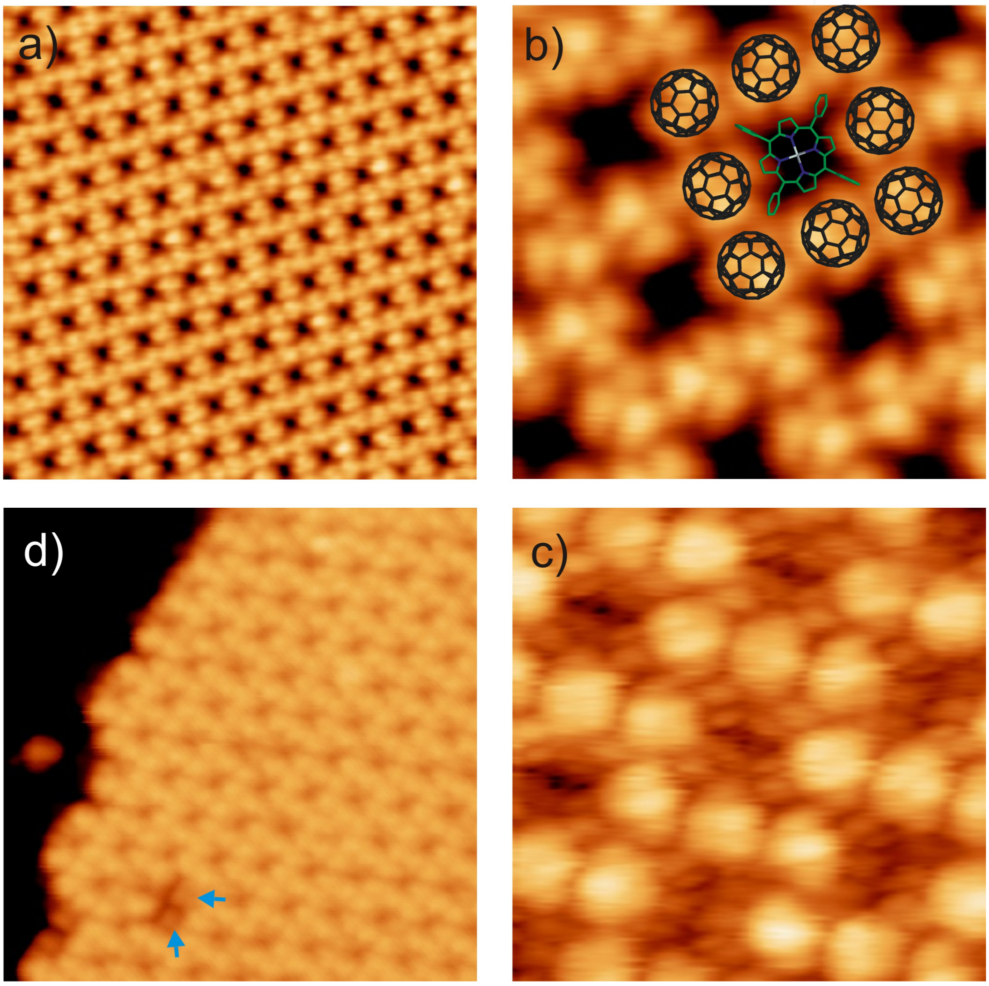

Figure 4.14: a) Highly ordered square structure created by C_{60}s after annealing the sample to 493 K. Ordered C_{60} arrays in phase β dissolves to form an extended mixed $C_{60}/Ce(TPP)_2$ arrangement. The mixed structure is mediated by $Ce(TPP)_2$ complexes which lie at the center of a square arrangement composed of 8 C_{60} molecules (Parameters: 221×221 Å^2, $V_b = 1.8$ V, $I = 0.08$ nA). b) A high-resolution STM image of the square like C_{60}-$Ce(TPP)_2$ arrangement. The C_{60}s evidence a three-fold symmetry indicating that the molecules are places directly in contact with the Ag(111) substrate. C_{60} models and the model of a top porphyrin of the $Ce(TPP)_2$ are superimposed on the STM image (Parameters: 55×55 Å^2, $V_b = 2.2$ V, $I = 0.05$ nA). c) High-resolution STM image of the mixed network where the $Ce(TPP)_2$ complex is visible. The orientation of the $Ce(TPP)_2$ complex is discernible as a darker line running through the center of the complex (Parameters: 55×55 Å^2, $V_b = -1.9$ V, $I = 0.1$ nA). d) An island of the $C_{60}/Ce(TPP)_2$ arrangement where a missing C_{60} reveals the double deckers (indicated by blue arrows) which was not visible when the C_{60}s were present (Parameters: 220×220 Å^2, $V_b = 2$ V, $I = 0.038$ nA). Spectroscopic information at the center of the square arrangement corresponds to a confined $Ce(TPP)_2$.

neighborhood of 8 C_{60} molecules surrounding the individual Ce(TPP)$_2$ complex. As it can be seen from the spectra of the C_{60} on a metal (violet spectra), the **LUMO+1** peak positions of Ce(TPP)$_2$in the dense packed islands as well as the one confined in phase γ lie within the broad **LUMO+1** resonance of C_{60} on Ag(111). The spectra of C_{60} on Ag(111) in phase γ also evidences a small variation (**LUMO** - 0.3 eV and **LUMO+1** - 1.6 eV) with respect to the C_{60} islands on Ag(111) without the Ce(TPP)$_2$ surrounding (**LUMO** - 0.5 eV and **LUMO+1** - 1.8 eV). The Ce(TPP)$_2$ molecules are extremely important in mediating the square arrangement of the C_{60}s. Hence it is also probable that the Ce(TPP)$_2$ complexes and the C_{60}s influence each other electronically.

In order to verify the role of Ce(TPP)$_2$ in mediating the square like arrangement of C_{60}s, a control experiment was performed with free base porphyrins in the place of Ce(TPP)$_2$, which is described as follows: Free base porphyrins were deposited onto the Ag(111) substrate and subsequently C_{60}s were deposited on the substrate. The sample was annealed to the same temperature for the same time, at which the mixed C_{60}-Ce(TPP)$_2$ structure was formed (493 K). However in this case, no such like arrangement of the C_{60} were observed. The C_{60}s and the free base porphyrins formed separate islands. This indicates that the Ce(TPP)$_2$ were responsible for inducing the specific arrangement of the C_{60}s.

The C_{60}s that are not incorporated into the unique square like arrangement formed extended dense packed islands with two distinct orientations: *(i)* A three-fold appearance which corresponds to a hexagon of the C_{60} facing the surface and *(ii)* A two-fold appearance corresponding to a 6 : 6 bond facing the surface. This two-fold appearance only occurs after an annealing treatment.

4.6 Conclusion

In summary, we have studied the structural characteristics and the electronic properties of non-covalent architectures of C_{60}-Ce(TPP)$_2$ on Ag(111) at a single molecule level, extended arrays and ordered C_{60} arrangement mediated by Ce(TPP)$_2$. The C_{60}-Ce(TPP)$_2$ system evidences three unique phases named α, β and γ. In phase α, the C_{60} binds site-selectively face-to-face above the center of the Ce(TPP)$_2$ complexe implying a molecular recognition process, favored by a non-planar deformation of the top porphyrin, which fits to the convex shape of C_{60}. **DFT** calculations evidence a bowl shaped top porphyrin of the Ce(TPP)$_2$ that confines the C_{60}. The C_{60} exhibits a total of three distinct orientations per double-decker species, which are identified by a comparison of STM data to extended Hückel simulations. These well-defined configurations evidence specific stereochemical interactions between the fullerene and the porphyrin guiding the intra-dyad coupling. By stimulation with the STM tip, individual C_{60} units can be switched reversibly between the three orientations, each revealing a unique level of conductance. Comparative scanning tunneling spectra show that the $Ce(TPP)_2$ strongly reduces the coupling of the C_{60} to the metallic substrate: the band gap increases and an **NDR** region emerges. This decoupling from a metallic support is a prerequisite for potential charge separation in the **D-A** complex under optical excitation. The charge separation is a very important criteria for realizing potential photovoltaic applications.

After the characterization of individually confined C_{60}s, the sample was annealed at room temperature and a new ordered array of C_{60}s designated as phase β was formed on top of the dense-packed double decker layer. This ordered architecture of the C_{60}s has a bi-layer zig-zag arrangement where a bottom layer lies close to the $Ce(TPP)_2$ molecules forming an array with an intermolecular C_{60} distance of 13.9 Å, which is also the nearest neighbor distance of the $Ce(TPP)_2$ assembly. The top layer is stacked in between the gaps created by the bottom layer thereby evidencing the same intermolecular distance. This bi-layer structure was characterized both topographically and electronically. Hence room temperature annealing of C_{60}s confined on $Ce(TPP)_2$ provides a pathway to create a well ordered templated fullerene nanostructure. This is also an extension of the individual $C_{60}/Ce(TPP)_2$ and therefore increases the scope of creating large, extended platforms for practical organic solar cell applications.

Further annealing of the sample leads to a third phase γ. this phase constitutes a mixed C_{60}-$Ce(TPP)_2$ architecture where 8 C_{60} molecules surround an individual $Ce(TPP)_2$ complex thereby creating a mixed $C_{60}/Ce(TPP)_2$ assembly. Such kind of arrangement of the double deckers with equal spacing is beneficial for creating controlled designs of supramolecular nano structures and hosts for confining individual guest species on surfaces with uniform separation, that could not be achieved with direct sublimation.

Altogether, $C_{60}/Ce(TPP)_2$ is an excellent model system for a non-covalently stacked molecular interface, where a fullerene-porphyrin coupling can be studied at a single molecule level or as ordered agglomerates and bi-molecular networks for controlled surface confinement experiments. Further, by testing various forms of fullerenes like C_{70}, $C_{56}Cl_{12}$ and [6,6]-PCBM and double deckers based on various lanthanide elements, the present study could be extended to gain a deeper insight into the charge transfer properties between donor and acceptor molecules and achieve a practical and easily addressable organic photovoltaic device with a high power conversion efficiency.

4.7 Experimental details

The Ce(TPP)$_2$ was deposited by organic molecular beam epitaxy (OMBE) from a quartz crucible held at 703 K. Ce(TPP)$_2$ was thoroughly degassed prior to any experiments resulting in a background pressure in the 10^{-10} mbar range during deposition. The Ce(TPP)$_2$ molecules were obtained from Dr. Kentaro Tashiro from NIMS, Japan with a purity of ($>$ 95 %). After dosing Ce(TPP)$_2$ at room temperature, the sample was annealed to a temperature of 493K. Subsequently, the sample was cooled down and transferred into the STM chamber, where the Ce(TPP)$_2$ array quality was checked by constant current images recorded at about 10 K. All the STM images were processed using the **WsXM** software. [220] The sample was then taken out of the STM and C$_{60}$ molecules were deposited directly onto the cold sample containing the Ce(TPP)$_2$ islands in order to achieve isolated C$_{60}$s on Ce(TPP)$_2$ islands (phase α) as well as on the Ag(111) substrate. After phase α was checked, the sample was taken out of the STM and annealed at room temperature in order to achieve ordered C$_{60}$ arrays on Ce(TPP)$_2$ islands (phase β). Phase γ was achieved by annealing the sample to a still higher temperature, 504 K for 10 minutes.

5 Fe confinement on Co-TPP arrays

5.1 Outline

The confinement and ordering of nanoscale objects as individual atoms or molecules on substrates has gained widespread attention in recent years leading to the realization of individually addressable quantum arrays. [221] [222] [223] Several molecular systems have been investigated in this regard and successful control of their physicochemical and magnetic properties have been demonstrated on a single molecule [224] or a few-atom level. [22] Specifically, nanoscale assemblies comprising single atomic spins and magnetic moments are exciting from a basic scientific point of view, [225] but also promising for the realization of potential information storage and quantum computing devices.

STM on surfaces has opened up the fascinating perspective to build tailored structures consisting of just a few individual atoms or molecules and to directly explore their electronic and magnetic properties. [4] However, this serial atomic manipulation technique only allows for the construction of specific configurations of limited extension and is not applicable for large-scale patterning of substrates, a frequent criterion for applications. Alternatively, self-assembly of adatom and cluster arrays formed via substrate-mediated interactions as strain or surface state scattering have been reported. [226] [227] [228] Obviously, the latter approach is quite limited concerning the choice of periodicity and symmetry. In addition, the direct adsorption of metals and molecules on metallic substrates commonly effect their electronic and magnetic properties. [229] [230] Consequently, we aim for a procedure that both reduces the coupling of atoms to the metallic surface and provides highly regular extended arrays. In this regard, recent studies have introduced the concept of confining metal atoms on self-assembled organic layers. [231] [232] Thereby, the site-selective adsorption of atoms is a key process. Special focus lies on transition metal atoms featuring magnetic moments induced by unpaired *d*-electrons. [233] Confining these atoms in arrays with tunable separation opens up new avenues to explore the inter-atomic magnetic coupling [234] and substrate-orbital coupling. [235] From a different perspective, a site-specific confinement of adsorbates on organic layers provides suitable model systems to explore donor-acceptor systems on a single atom level and to tailor the properties of surface-anchored supramolecular architectures by atomic doping. [230] Such dyads provide interesting potential for surface confined molecular machines, memories [236] and charge transfer systems. [237] Hence a comprehensive characterization of the electronic coupling between the metal and the supporting molecule is of significant interest.

Here we introduce a multi-technique investigation of the adsorption, spatial ordering, switching and magnetic properties of Fe on a highly regular metalloporphyrin template layer. Specifically, arrays of Co-tetraphenylporphyrins (Co-TPP) assembled on Ag(111) are exposed to an atomic beam of Fe at low-temperature. The Co center in surface-anchored porphyrins provides an active site for ligation. [238] [239] Interactions with the Ag(111) substrate result in a quenching of the magnetic moment of Co-TPP. Upon Fe deposition, individual atoms and small clusters decorate the porphyrin macrocycle and site-selectively adsorb in close proximity to the Co center, reviving the magnetic moment of Co-TPP. Similar ligation induced control and switching of the spin-state in adsorbed porphyrins was achieved by nitric oxide [240] or oxygen. [241] Our X-ray magnetic circular dichroism (XMCD) experiments evidence a ferromagnetic coupling between the Fe adsorbates and the Co center.

After the characterization of the adsorption position, the Fe atoms were reversibly switched through various distinct positions on the Co-TPP macrocycle. Due to its ability to directly address nanoscale structures with atomic resolution, STM is a very useful tool in this regard. Several STM studies have reported controlled switching of organic molecules by various triggers as bias voltage, [242] tunneling current, [243] electric field [244] or mechanical manipulation. The reversible switching of the conformation, orientation, charge and magnetic state, or proton configuration of molecules has been achieved by addressing them individually on metallic supports, [27] on insulating layers [245] or on supramolecular templates. [246] [134]

5.2 Results and discussion

5.2.1 Fe confinement and adsorption position:

Figure 5.1a shows an STM image of a Co-TPP array formed on Ag(111) after deposition at 340 K. The molecules assemble in extended dense-packed domains representing a square lattice with a periodicity of 14.05 ± 0.2 Å. In agreement with earlier reports, six different orientations of the Co-TPP domains are observed. [247] A bright central protrusion, originating from Co atomic states, dominates the appearance of Co-TPP/Ag(111) at low bias voltages (cf. Figure 5.1a). [248] At higher negative bias voltages ($V_b > -0.5$ eV), sub-molecular resolution evidences a two-fold symmetry of the Co-TPP macrocycle (cf. inset Figure 5.1a). As detailed in a previous study, this contrast represents an adsorption induced saddle-shape deformation of the Co-TPP (see Figure 5.1c). [247] The electronic structure of the Co-TPP/Ag(111) interface is well characterized in literature, the magnetic properties however are addressed in this report for the first time. We find a quenching of the Co magnetic moment due to interaction of Co-TPP with the underlying metal (vide infra).

The high structural regularity of the well characterized Co-TPP arrays on Ag(111) makes them promising templates for hosting guest species. This potential was for example highlighted by the ligation of Co-TPP with small gas molecules as carbon monoxide or nitric monoxide. [249] [250] Here, the Co-TPP arrays were exposed in-situ at 10 K to an atomic beam of Fe. A typical STM image after Fe deposition is shown in Figure 5.1b. Clearly, bright (white) protrusions in registry with the Co-TPP lattice (grey array) can be observed. At low coverage, most of these protrusions can be assigned to individual Fe atoms, while at higher coverage small Fe cluster are more prominent (vide infra).

A close-up STM image (Figure 5.1d) confirms that the bright protrusions appear at the position of the Co-TPP molecules. Importantly, atomic manipulation experiments prove that the Fe adsorbs on the Co-TPP macrocycle. Figure 5.1e shows the area represented in Figure 5.1d after controlled removal of four Fe atoms by the STM tip and reveals a complete subjacent Co-TPP array. Consequently, we conclude that the Fe is indeed confined on the porphyrin macrocycle, ruling out a possible adsorption below or between Co-TPP molecules. Any attempts to laterally transfer Fe atoms to an adjacent porphyrin failed, indicating considerable site-specific interaction between the Fe and the macrocycle. The data presented in Figure 5.1d were recorded on a Ag(111) surface not completely covered by Co-TPP, which allows us to quantify the Fe coverage (vide infra) and to directly compare the appearance of Fe atoms on Ag(111) and on Co-TPP. The line profile plotted in Figure 5.1f reveals an increased apparent height (1.8 Å at −0.5 V) of Fe atoms confined on the porphyrin compared to Fe/Ag(111) (1.4 Å), evidencing a modified electronic environment.

A careful inspection of high-resolution STM data reveals that the Fe atoms are not perfectly centered on the Co-TPP molecule, but adsorb in a bisector plane slightly displaced from the center (cf. Figure 5.2a). In total, four equivalent positions are observed for Fe on Co-TPP, which reflect the "quasi" four-fold symmetry of the saddle-shaped macrocycle (cf. Figure 5.1c). The projected distance of the Fe from the Co center extracted from STM data amounts to 1.85 ± 0.2 Å, the symmetry reduction is evidenced by a smaller separation of the projected Fe position from the α-pyr axis (1.5 ± 0.2 Å) as from the κ-pyr axis (1.0 ± 0.2 Ą) (cf. Figure 5.2b). **DFT** calculations (performed by Marie-Laure Bocqet, Lyon, France) reveal that the Fe atom indeed binds strongest in an off-center bisector position (cf. Figure 5.2d) with a binding energy of 1.87 eV. This configuration increases the binding energy by 0.29 eV as compared to a tilted on-top adsorption (described in Figure 5.6), thus corroborating the experimental observations. The Fe positions on the adsorbed porphyrin macrocycle extracted from theory (projected distance Fe - Co 1.75 Å, Fe - α-pyr 1.44 Å, Fe - κ-pyr 1.00 Å in Figure 5.2d) perfectly agrees with the experimental values. The excellent agreement between the computed apparent height in STM simulations (cf. Figure 5.2c) and the measured scan profile of Figure 5.1f should also be underlined. Both agree with an overall corrugation of $\sim$ 5 Å, with respect to the bare Ag metal surface level.

From the analysis of the most stable structure, Fe is threefold bonded to different atoms : one N from an κ-pyr group, one C from an α-pyr group and the central Co atom. The Fe-C bonds of 2.06 Å correspond to classical bonds in ferrocene ($FeCp_2$) species. [251] The short Fe-Co bond (2.45 Å) indicates a strong metallic interaction, being even slightly lower than the usual bonds encountered in bimetallic or trimetallic metal complexes ($\sim$ 2.55 Å). This multiple hapticity of Fe permits to stabilize this highly reactive metal adatom. The porphyrin-cobalt complex hence offers a very specific site for the Fe atom.

5.2.2 Switching of Fe atoms

The Fe deposited on a Co-TPP molecular layer adsorbs directly on the macrocycle in close proximity to the central Co ion. Here, the smallest unit is identified as an individual Fe atom. A close inspection reveals four distinct off-center positions for Fe adsorbed on the Co-TPP macrocycle (Figure 5.2). At regular scanning conditions

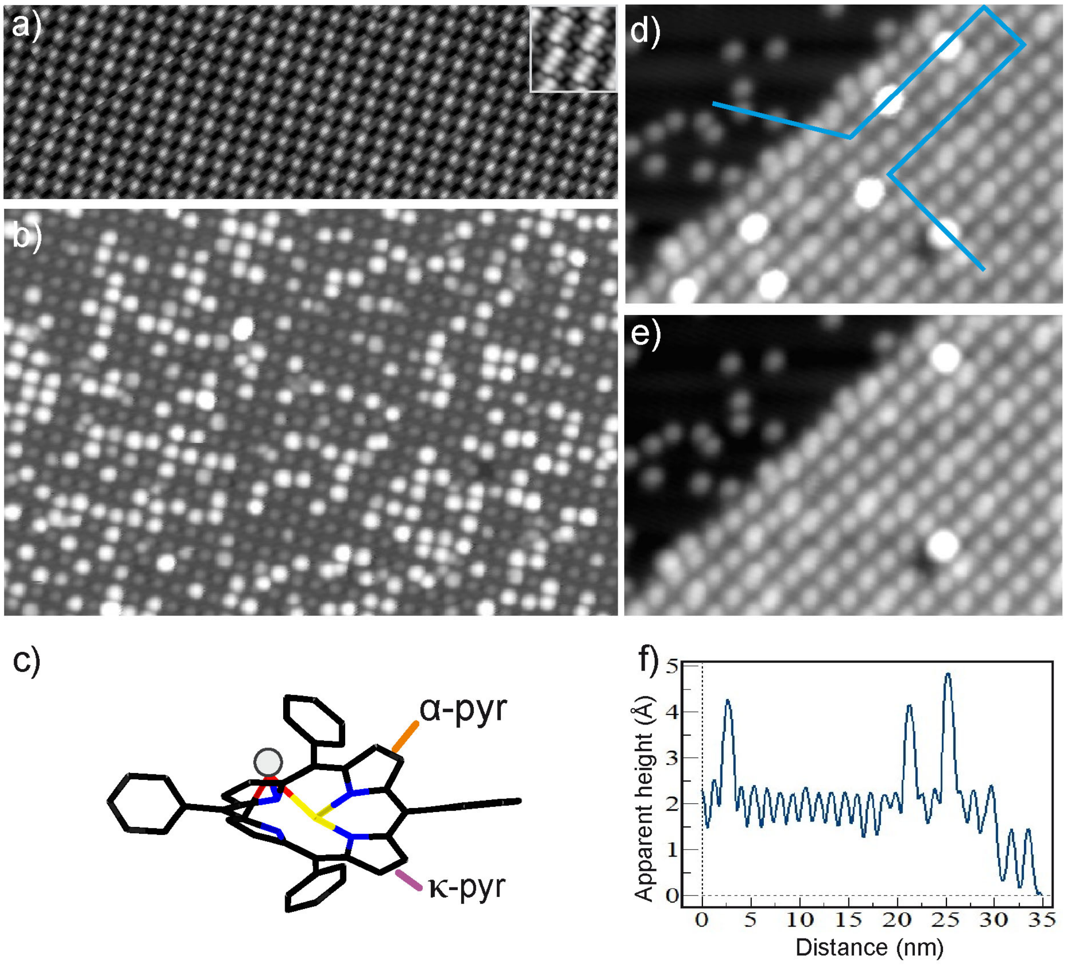

Figure 5.1: a) STM image representing a highly regular array of Co-TPP molecules on Ag(111) ($I = 0.09$ nA, $V_b = -0.4$ V, 443×221 Å^2). Inset shows a high-resolution image of a Co-TPP lattice evidencing a two-fold symmetry of the macrocycle ($I = 0.12$ nA, $V_b = -0.9$ V, 20×20 Å^2). b) Typical data after exposing the Co-TPP array (grey lattice) to an atomic beam of Fe. The Fe (white protrusions) follows the lattice of underlying Co-TPP ($I = 0.03$ nA, $V_b = -0.1$ V, 443×221 Å^2). c) Model of a Co-TPP molecule in its adsorbed geometry highlighting the saddle-shape distortion of the macrocycle and visualizing a Fe atom (white ball) trapped on the porphyrin. d) Zoom-in image representing a Ag(111) area partially covered by a Co-TPP islands. The blue line marks the height profile shown in f). e) Same area as shown in d) after the deliberate removal of Fe atoms from the Co-TPP template. Parameters for d), e): ($I = 0.1$ nA, $V_b = -0.5$ V, 419×150 Å^2) f) Height profile allowing for a direct comparison of the apparent height of Fe atoms on Co-TPP and Ag(111).

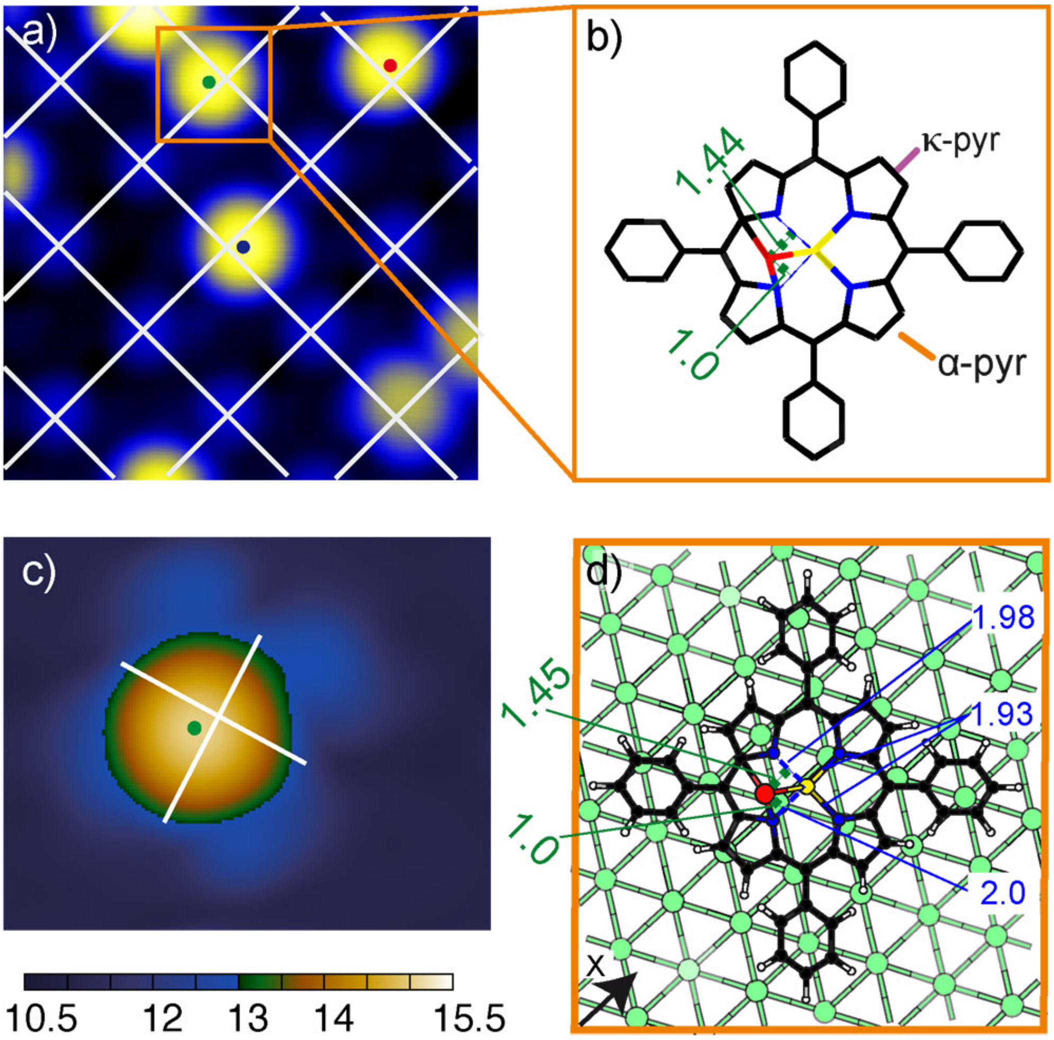

Figure 5.2: a) High-resolution STM image revealing a minute off-center adsorption of the Fe atoms on the porphyrin lattice. ($I = 0.1$ nA, $V_b = -0.1$ V, 55.4×55.4 Å^2). b) Schematic model displaying the lateral Fe (marked with a red ball) displacements from α and κ directions extracted from the STM data. c) Simulated constant-current STM image based on the structure shown in d) ($V_b = -0.2$ V, 32×25 Å^2). The given distances are relative to the bare Ag substrate and the overall corrugation amounts to 5 Å. d) DFT optimized Fe/Co-TPP complex on Ag(111) in a $11 \times 5\sqrt{3}$ cell corroborating the off-center adsorption. The projected distances are indicated on the left and perfectly match the experimental values (compare b). The four Co-N distances are quoted on the right to unveil the structural deformation upon Fe coordination. Green, black, blue, white, yellow and red balls depict Ag, C, N, H, Co and Fe atoms respectively. See text for discussion.

(typical bias voltage $V_b \approx -0.5$ V, $I \approx 30$ pA) the Fe atoms can be imaged stably without removal from the macrocycle or translation to adjacent sites, guaranteeing a reliable read-out of the atomic position. However when the tip was approached closer to the surface (typical bias voltage $V_b \approx -0.1$ V, $I \approx 100$ pA), it was possible to induce a translation of the Fe atom within the macrocycle. Figure 5.3b visualizes such a hop of one Fe atom from one off-center position to another one. During scanning, the central atom was displaced from left to right. On the time-scale of the STM experiment, this process happens immediately, thus only the initial and final positions of the Fe atoms are resolved. An analysis of a time-series of STM images recorded with scanning parameters chosen in a way to match the hopping rate with the image frequency allows us to determine all the equilibrium positions one Fe atom can occupy. As an example, Figure 5.3c shows a superposition of two STM images recorded before (red) and after (green) a switching event. From such image series, the Fe positions can be extracted with high precision. The analysis reveals that each Fe atom can be translated between four distinct sites on the supporting porphyrin. Figure 5.4 shows a complete series highlighting all four positions of the atom switch.

STM images are recorded at a bias voltage where the saddle-shape deformation of the Co-TPP is resolved, resulting in a two-fold symmetric appearance of the porphyrin (see Figure 5.1c) which unequivocally show the orientation of the Co-TPP in the dense-packed arrays. Accordingly, the four Fe positions discussed above can be directly assigned to adsorption sites on the porphyrin macrocycle. Figure 5.3 summarizes the experimental findings and reveal a switching distance of 2 ± 0.2 Å along the axis of the upward bent pyrrole rings and 3 ± 0.2 Å perpendicular to it. A DFT optimized Co-TPP molecule with an adsorbed Fe highlighting the off-center position is shown in Figure 5.2d. The experimental values for the distance of Fe from the Co ion agree closely to the DFT findings. Clearly, the two-fold macrocycle geometry is reflected in the Fe positions that do not mark a square, but rather a rectangle (see Figure 5.4).

A statistical analysis shows that the Fe translates predominantly parallel or perpendicular to the main axis of the molecule (α-pyrrole), diagonal hops were only observed very rarely and might be attributed to the limited time-resolution of the STM. Increasing the tip-sample interaction by raising the tunneling current yields higher switching rates (see Figure 5.5). Interestingly, the apparent height and the contrast of the Fe atoms in STM images are identical in all four positions on the porphyrin, indicating that the electronic interaction of the Fe with the Co-TPP is comparable, i.e. the adsorption sites are equivalent.

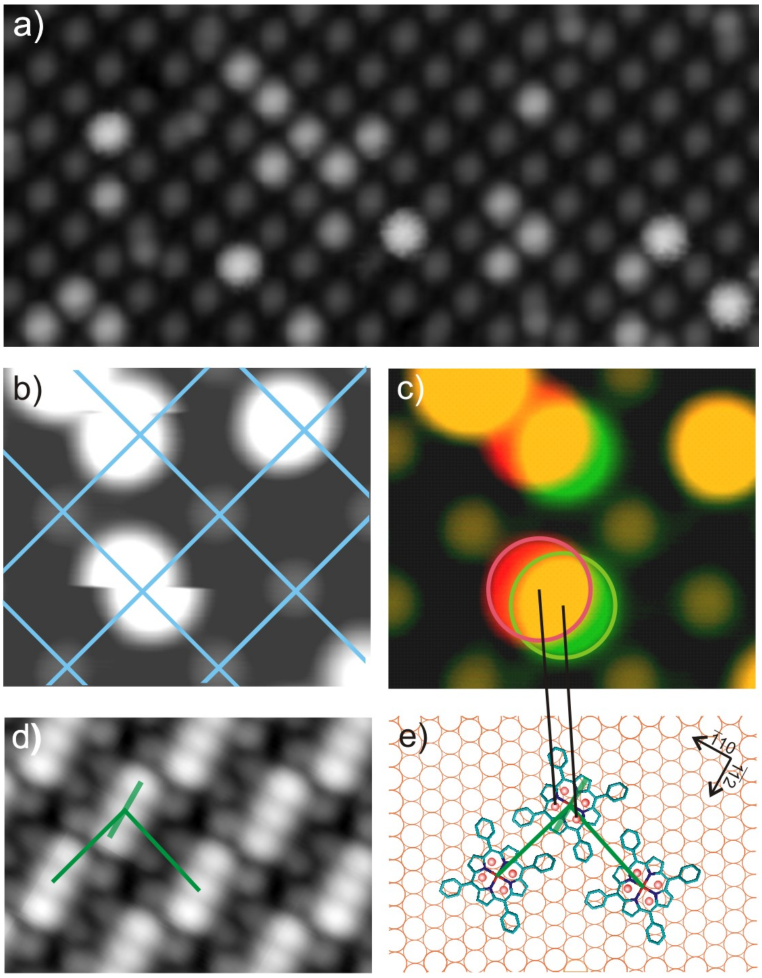

Figure 5.3: a) Typical STM image after exposing the Co-TPP array to an atomic beam of Fe. The Fe (white protrusions) follows the lattice of underlying Co-TPP (I = 30 pA, $V_b = -0.1$ V, 220 × 100 Å^2). b) Faint grey spots in the background correspond to the center of the Co-TPP, highlighted by the intersecting points on the grid while the white protrusions correspond to the confined Fe atoms. The central atom is laterally moved on the macrocycle while scanned by the tip. This hop is visualized by the abrupt movement of the Fe atom ($I = 0.1$ nA, $V_b = -0.1$ V, 46 × 40 Å^2). c) Superposition of two STM images highlighting the adsorption positions before (red) and after (green) translation ($I = 0.1$ nA, $V_b = -0.1$ V, 46×40 Å^2). During switching, the Fe atoms are confined to the macrocycle of the porphyrin. d) Close packed Co-TPP array evidencing an elongated central part ($I = 0.1$ nA, $V_b = -0.7$ V, 46 × 32 Å^2) representing the two-fold symmetric saddle-shape geometry of the macrocycle. The green lines highlight the central axis of the molecule and the square the unit cell with a side length of 14.05 Å. e) Schematic model of the porphyrins on the Ag(111) lattice. The four red dots surrounding the center of the macrocycle correspond to the 4 possible positions of the Fe atom.

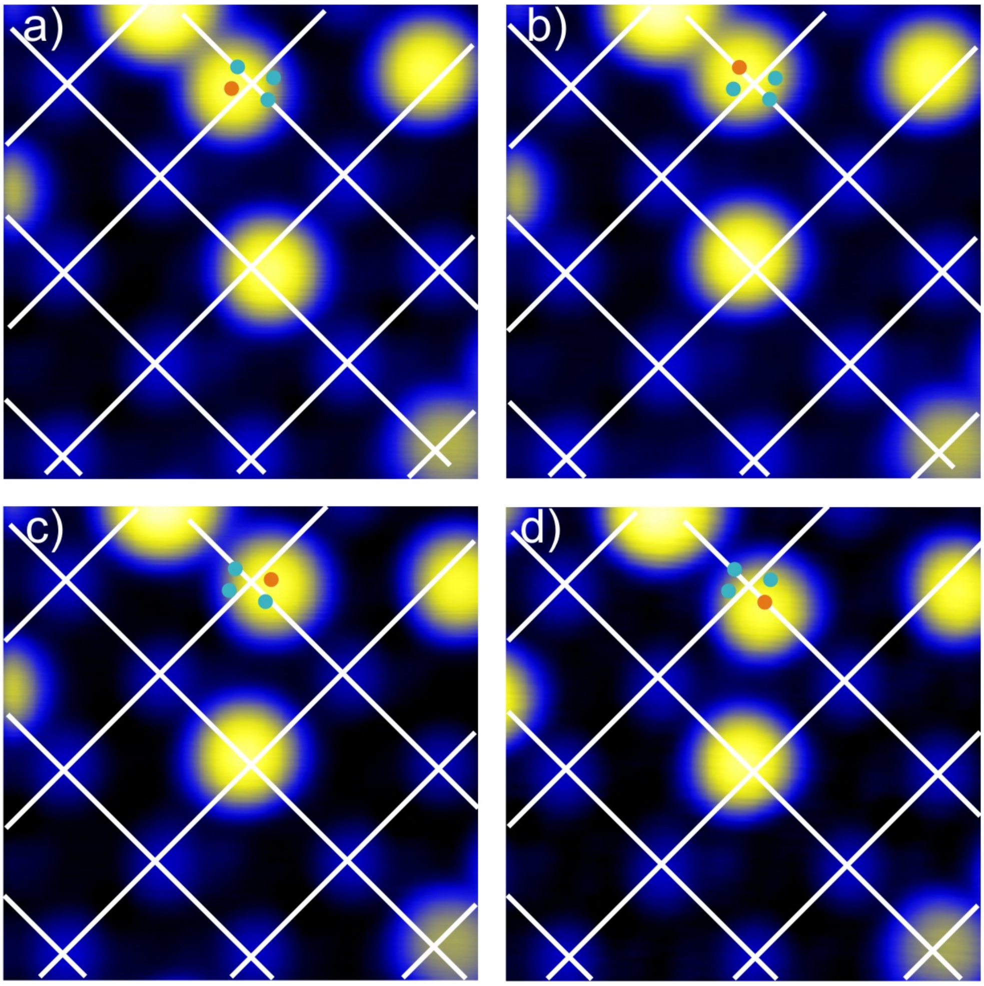

Figure 5.4: a) Yellow protrusions correspond to Fe atoms adsorbed on a dense packed Co-TPP array (blue lobes). The Fe atoms can occupy four distinct positions on the macrocycle of the porphyrin, as exemplified for the atom at the top center. The STM images in a, b, c and d highlight the four equilibrium adsorption sites. In the images, the occupied position is marked by an orange dot and the adjacent three positions by blue dots. The intersecting points of the white grid represent the center of the underlying Co-TPP molecules. The off center positions of the Fe atoms are clearly discernible (a,b,c,d: $I = 0.1$ nA, $V_b = -0.1$ V, 50×50 Å^2).

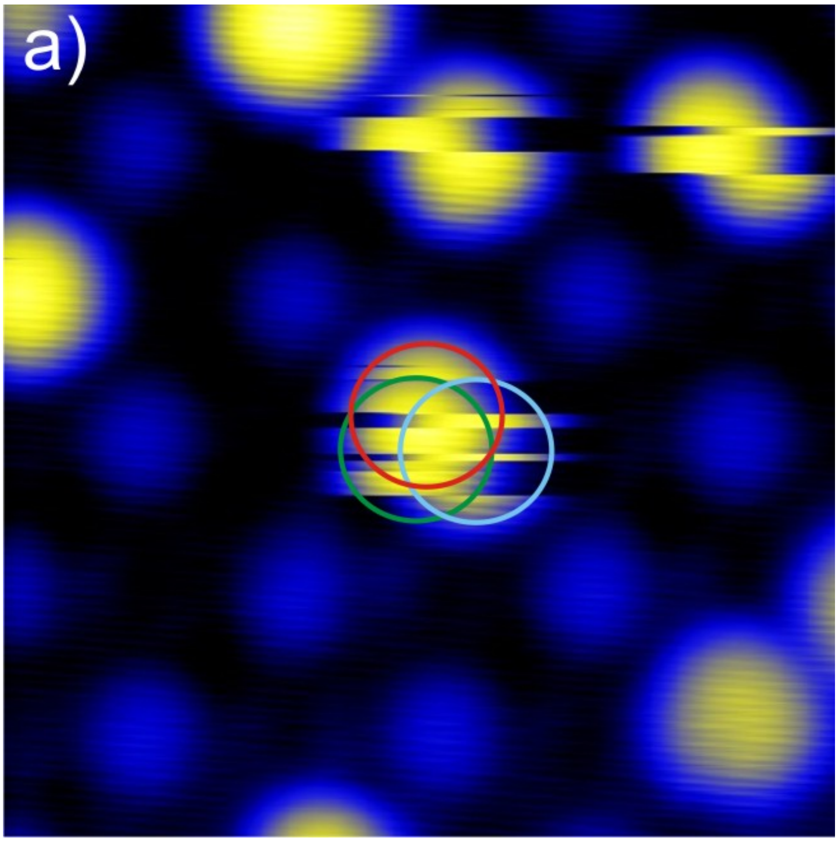

Figure 5.5: An Fe atom is seen to be switching between three of the four available positions on the Co-TPP macrocycle. The increased switching rate compared to the situation shown in Figure 5.3b, which was recorded with the same scanning speed is induced by a higher tunneling current. Colored circles (red, green, blue) mark the three positions. ($I = 1$ nA, $V_b = -0.1$ V, 55×55 Å^2)

5.2.3 Fe coverage dependence

Figure 5.6 summarizes the coverage dependent growth of Fe on the Co-TPP arrays. Already a simple visual inspection of the STM images reveals that the Fe follows the square lattice of the porphyrin template throughout the coverage range explored. As the Fe dose is augmented, both the occupation of Co-TPP and the average cluster size increases. While individual Fe atoms dominate the low-coverage situation (Figure 5.6a), cluster reaching an apparent height of 9 Å are observed at higher coverage Figure 5.6f). Interestingly, even at the highest coverage, no coalescence of clusters is observed. The Fe does not grow between the porphyrins or at the molecular boundary.

Three values are used to describe the Fe morphology on the Co-TPP template layer: (i) the occupation $\boldsymbol{O}$ of Co-TPP, where 0% corresponds to a bare Co-TPP array and 100% would correspond to a situation where every porphyrin is occupied by one or more Fe atoms. (ii) The total Fe coverage Θ in percentage of a monolayer (ML). Here, one ML is defined as one adsorbate unit per surface atom. A full Co-TPP layer would thus correspond to a coverage of 0.037 ML. (iii) The average cluster size $\boldsymbol{s}$, i.e. the average number of Fe atoms on an occupied porphyrin. These values are indicated in the caption of Figure 5.6 for every coverage.

It should be noted that a precise determination of the Fe coverage and the cluster size is not trivial. We considered Ag(111) surfaces not completely covered by Co-TPP. By measuring the density of individual Fe atoms on the bare Ag areas, the amount of Fe on the adjacent porphyrin arrays was calibrated. This procedure assumes that no Fe atoms are exchanged between Ag and Co-TPP, an assumption fully justified at the low temperature of deposition (10 K) where atomic diffusion is suppressed. [252] As a result, we conclude that the majority of the protrusions at low coverage correspond to individual Fe atoms. However, already in this situation apparent height measurements reveal the existence of dimers. At high coverage ($\Theta \approx 6$ %), this calibration procedure gets less reliable, as Fe aggregation starts on the bare Ag areas and the classification of cluster sizes on Co-TPP by measuring the apparent cluster heights turns difficult, which would result in considerable error bars for values **(i-iii)**.

To circumvent this problem, we compared our experimental data to a statistical simulation based on random adsorption in a drop-and-stick model (see Figure 5.7). The fact that the modelled values for low-coverage, where the experimental calibration is reliable, agree reasonably well with the experimental values leads us to conclude that the Fe morphology is mainly dictated by random adsorption with no indication for Fe transfer between porphyrins.

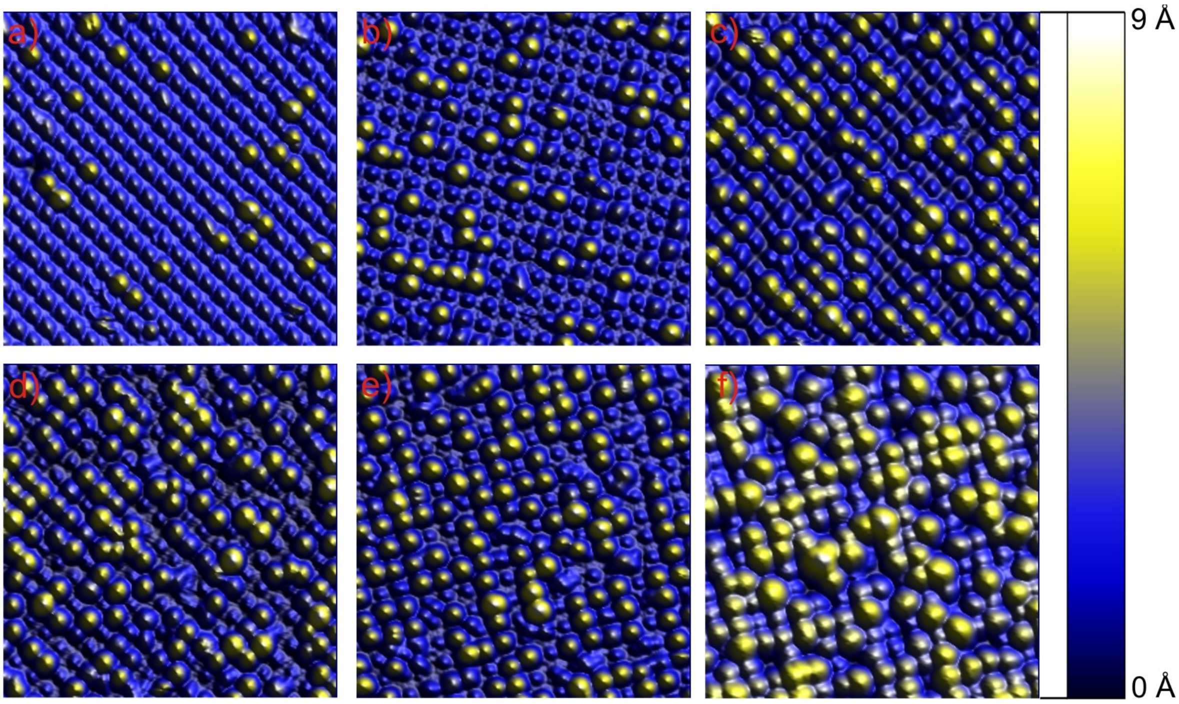

Figure 5.6: Series of STM images (a-f) representing the effect of a rising Fe coverage Θ: Both the occupation **O** of Co-TPP as well as the average cluster size ***s*** increase (Compare to simulated distributions in Figure 5.7). The color scale is adapted to highlight the Fe (yellow) on the Co-TPP array (blue). Throughout the whole coverage range, the Fe follows the square lattice of the porphyrin template (all image sizes 220 × 220 Å^2). a) $\Theta \approx 0.7\%$ ML, O $\approx$ 11 %, s $\approx$ 1.3; I = 0.16 nA, V_b = -0.5V, b) $\Theta \approx$ 1.5 % ML, O $\approx$ 25 %, s $\approx$ 1.4; I = 79 pA, V_b = -0.1V, c) $\Theta \approx$ 3 % ML, O $\approx$ 51 %, s $\approx$ 1.6; I = 67 pA, V_b = -0.5 V, d) $\Theta \approx$ 4.5 % ML, O $\approx$ 64 %, s $\approx$ 1.8; I = 0.1 nA, V_b = -0.1V, e) $\Theta \approx$ 6 % ML, O $\approx$ 71 %, s $\approx$ 2; I = 67 pA, V_b = -0.1V, f) Θ Å 10 % ML, O $\approx$ 90 %, $s \approx$ 2.9; I = 89 pA, V_b = -0.1 V.

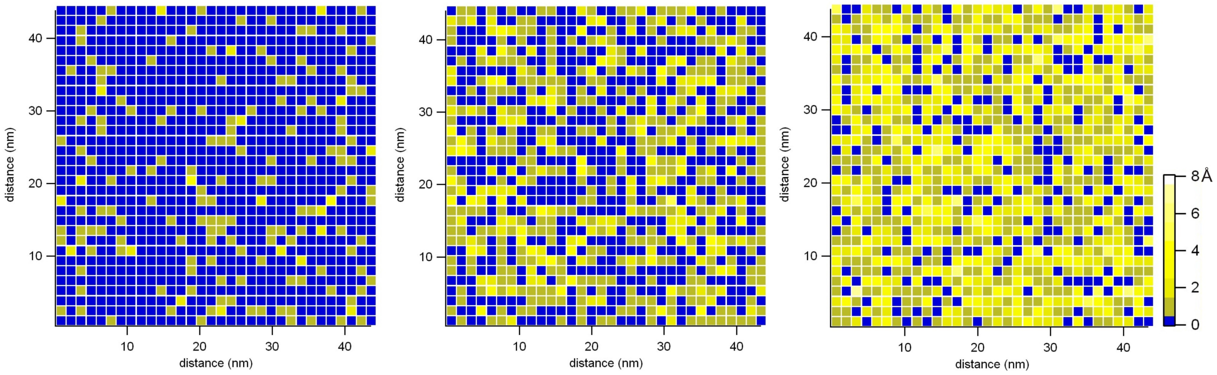

Figure 5.7: Examples of simulated particle distributions on a square lattice mimicking a Co-TPP array. A given number of particles (representing Fe atoms) is randomly adsorbed on the available area and the resulting number of particles per Co-TPP square is determined and represented by the color-coded filling of the square. Thus, each blue square corresponds to a bare Co-TPP unit while the yellow colors indicate occupation by Fe, where increasing brightness reflects larger cluster sizes. The images represent a coverage Θ of 0.7 % ML (a), 3 % ML (b) and 6 % ML (c), respectively and thus can be compared to Fig. 5.6 a), c) and e) in the article. At higher coverage, where the experimental determination of the Fe coverage is intrinsically inaccurate, these simulations are used to estimate the average cluster size **s** and to reduce the error bar of Θ. To this end, the coverage is adjusted in the simulation till the number of unoccupied Co-TPP sites fits the experimental value, which can be reliably extracted from the data

5.2.4 XMCD results

The Co-edge X-ray adsorption spectra (XAS) for circular (σ^+, σ^-) and linear (σ^v, σ^h) light polarization measured on the Co-TPP network with perpendicular and grazing incidences are shown in Figure 5.8. They show a clear fine structure in particular on the L_3 edge. On the bare network the X-ray magnetic circular dichroism (XMCD) signal reveals no sign of dichroism within the noise (Figure 5.8c). This directly translates to no net magnetization of the Co-center within the Co-TPP network. From the experimental data we can determine the magnetic moment of the Co ion to be $\leqslant 0.02$ μB. Thus the Co moment is quenched in the first layer of Co-TPP adsorbed on Ag(111). The pronounced linear dichroism (XLD) measured at grazing incidence (Figure 5.8d) reflects the inhomogeneous charge distribution within the Co 3d in- and out-of-plane orbitals.

In order to further understand the data DFT and ligand field multiplet calculations were performed. In the multiplet calculations the charge transfer and crystal fields acting on the Co center to fit the XAS data was verified. The resulting simulated XAS, XMCD and XLD spectra are plotted along with the experimental data in Figure 5.8. Very good agreement can be reached in the multiplet calculations using high crystal field parameters (10D$_q$= 2.5 eV, D$_s$= 0.38 eV, D$_t$ = 0.18 eV) and no

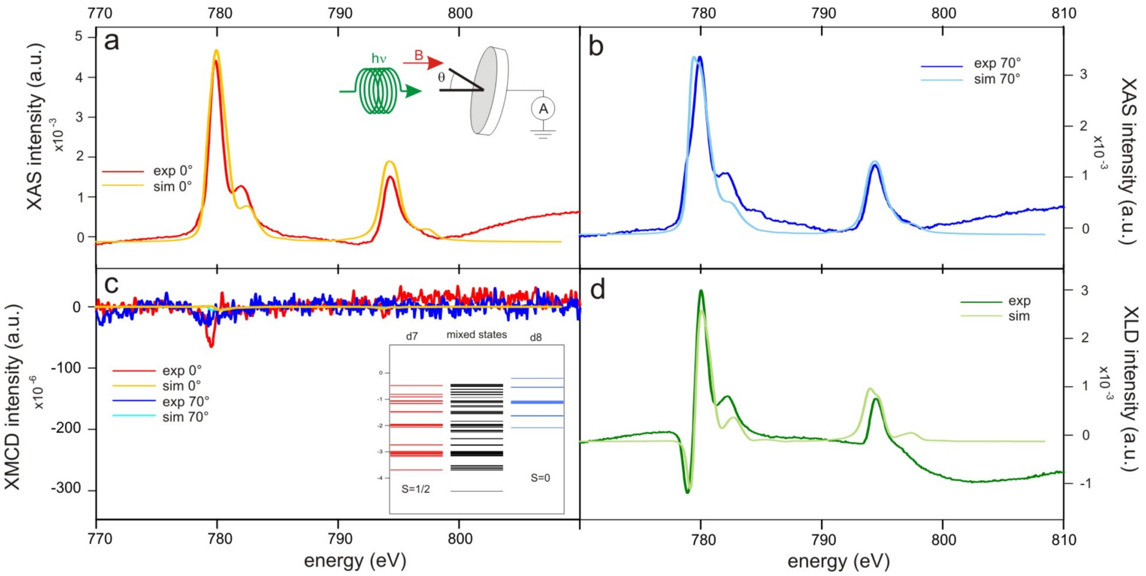

Figure 5.8: a)-d) X-ray absorption spectra measured on the bare monolayer of Co-TPP on Ag(111) together with the fits obtained by the multiplet calculation. a) XAS for σ^- for $\theta = 0°$. The inset of a) shows the measuring geometry. b) XAS for σ^- for $\theta = 70°$. c) vanishing XMCD (σ^+, σ^-) for $\theta = 0°$ and 70°. The inset of c) contains the energy level diagram derived from the multiplet calculations. d) XLD (σ^v, σ^h) for $\theta = 70°$. All spectra were measured at T = 8K for a)-c) B = 5T, for d) B = 0.2 T

or small charge transfers between the Co center and its ligands. However electron transfer from the substrate via the $d_z{}^2$-orbital has to be included to get the above shown agreement. Without hybridization to the substrate the Co-center has a d^7-ground state and the crystal fields bring the Co in a low spin configuration (S= $\frac{1}{2}$). Including charge transfer from the substrate results in a new $d^7 + d^8$ ground state (with a total of 7.25 electrons). The finite mixing with the d^8-states having S=0 forces singlet formation also in the d^7 configuration and result in a total quenching of the magnetic moment in close analogy to the case of Co-phthalocyanine [253] (see also level diagram in the insert of Figure 5.8c). This is in agreement to the experimental data where no XMCD signal is present.

5.2.5 Theoretical explanation of the XMCD results

Comparing the XMCD data for the bare Co-TPP to the DFT calculations, a very good overall agreement is observed. DFT also predicts the Co-TPP to have no magnetic moment as found in the experiment.

The X-ray adsorption measured on the Co-edge also shows a distinct XMCD peak after Fe-deposition (Figure 5.9c). This is a clear manifestation of the hybridization of the Co-center to the Fe-cluster. Since the Fe-cluster has large magnetic moments, the

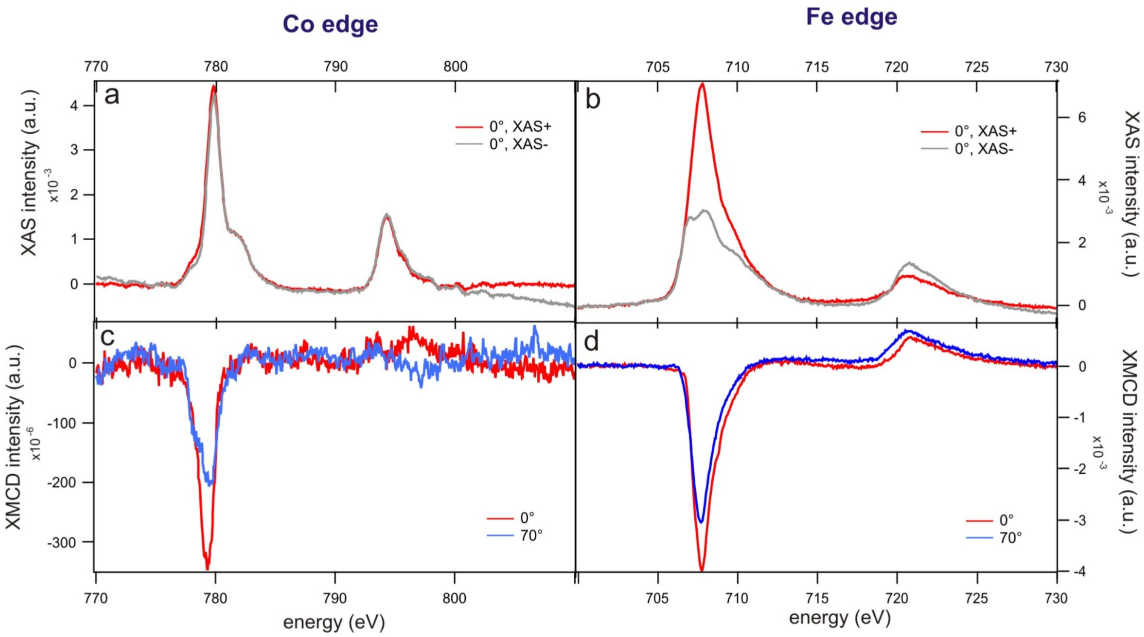

Figure 5.9: a) and c) show the XAS for σ^+ and σ^+ and XMCD data taken at the Co edge of the Fe covered Co-TPP network. b) and d) present the same measurements for the Fe edge. B = 5T, T = 8K. On first glance the X-ray adsorption spectra of Co (a)) are only little influenced by the adsorption of Fe. The main difference is that the shoulder in the L3 edge shifts towards the main peak. The X-ray adsorption spectra of the Fe-edge (b)) show broad peaks expected for larger Fe clusters. The XMCD in the Fe (depicted in d)) is strong.

hybridization induces finite magnetic moments also into the Co-center below.

The finite magnetic moments in both Fe and Co allow tracing the individual magnetization curves of the two elements. Both curves reach saturation for 0° implying an easy axis to be out-of plane. As visible in Figure 5.10, the magnetization curves of Fe and Co have a similar shape. From the additional knowledge of the very different size of the magnetic moments in Fe and Co we conclude that both magnetic moments are ferromagnetic coupled with a strength larger then the thermal fluctuations at T = 8 K $\approx$ 7 meV. To the best of our knowledge this is the first study that shows the effect of magnetic clusters adsorbed on a metal organic surface layer to steer not only the magnetic properties of the cluster, but to also induce an otherwise quenched moment of a metal organic layer. The spin-polarized DFT calculations conducted on the extensive system (the Fe/Co-TPP complex adsorbed on Ag(111) in the large rectangular cell adopted in the calculations) reveal that the adsorbed system holds a significant magnetization of 2.7 unpaired electrons, while in the absence of Fe no magnetization is seen for Co-TPP on Ag(111).

Spin-polarized **DFT** calculations conducted of the large-scale adsorbed systems have revealed two possible Fe adsorption sites : an energetically unfavorable one called Fe

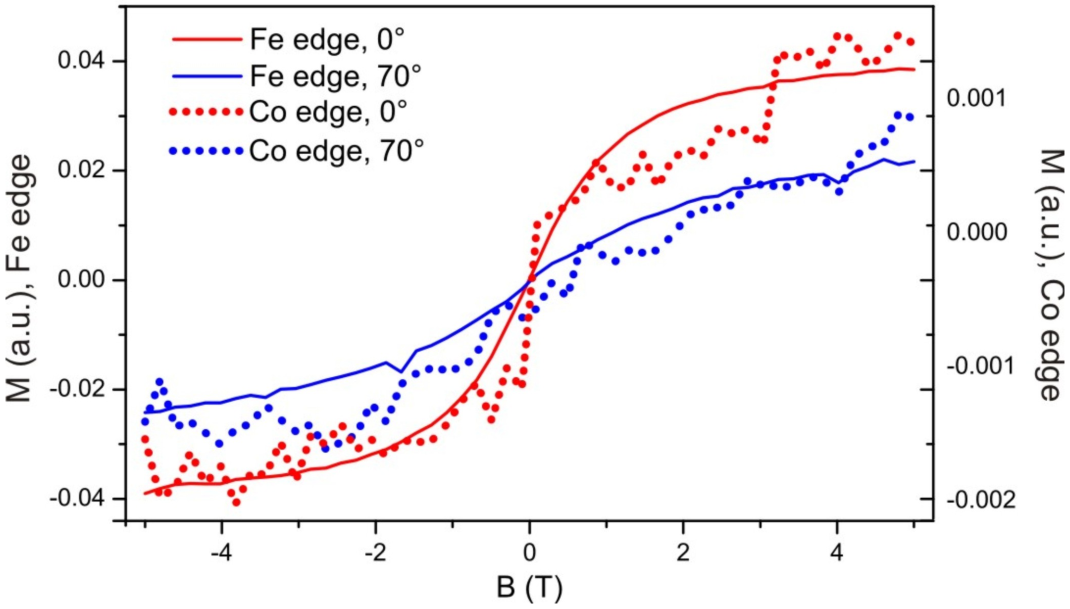

Figure 5.10: Magnetization curve of the Co and Fe obtained by measuring the XMCD at the L3 peak energy.

top (cf. Figure 5.11-upper panel) and a stable one called Fe bisector (cf. Figure 5.11-lower panel). Both configurations yield different structural, imaging and magnetic signatures which enable us to confirm that Fe bisector state is the one measured experimentally.

From a structural point of view, Fe in bisector position is shifted away from the two symmetric axis imposed by the *pyr* groups, while Fe in atop position is slightly displaced from the central position but remain in one the *pyr* axis. (c.f. Figure 5.11) And this lateral localization is quantitatively evidenced by STM imaging and STM simulations of the bisector case (see Figure 5.2). From a magnetization point of view, the Fe top preserves more magnetization than the bisector one, which is consistent with the reduction of coordination bonds (from three to one). The total magnetization amounts to 4.4 unpaired electrons. However spin density maps (not shown) are similar to the Fe bisector with an asymmetric repartition of spin between Fe and Co centers.

The Fe adsorption induces minor changes of the adsorption structure. Neither the interaction distance with the substrate, nor the altitude of the Co cation and the saddling conformation of the Co-TPP are modified. Hence no trans labilizing effect is visible as it has been evidenced for NO ligation onto CoTPP/Ag. The sole effect resides in the lengthening of some Co-N bonds in the bisector case in order to accommodate Fe. Without Fe, the Co-N bonds are 1.94 Å.

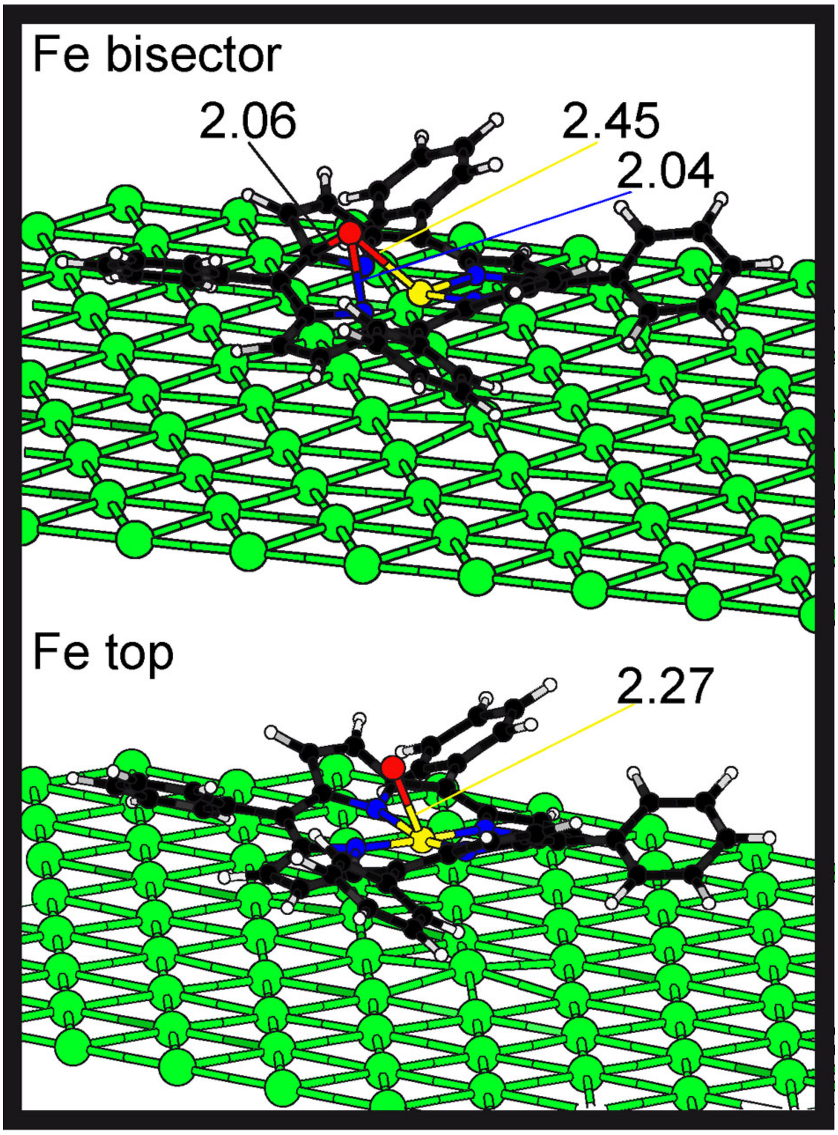

Figure 5.11: a)DFT optimized Fe/Co-TPP complex on Ag(111) in a $11 \times 5\sqrt{3}$ cell with two possible adsorption configuration : the so-called bisector position with BE (Fe) $= -1.87$ eV and the top position with BE (Fe) $= -1.58$ eV. In both structures the binding distance of the Co central atom to the Ag substrate is the same, close to 3.3 Å. In the bisector position the Fe is three-fold coordinated to the porphyrin core while in the top position Fe is mono-coordinated to Co, albeit a slight tilt in the direction of a N atom belonging to one κ-pyr group. But the Fe-N$_\kappa$ can only be considered as a loose bond of 2.2 Å.

5.3 Conclusions

In this chapter, Co-TPP molecules were used as a platform for confining individual and clustered Fe atoms. Fe was deposited in-situ on dense packed arrays of Co-TPP. The Fe atoms were seen to occupy four unique positions on the Co-TPP macrocycle, away from the central Co ion. The four adsorption sites of Fe on the macrocycle deviate from a perfect square, due to a saddle shape deformation of the Co-TPP molecule on Ag(111). Individual Fe atoms were switched between these four specific positions within the macrocycle area by manipulation with an STM tip, thus creating an atomic switch. Various coverage of Fe on the Co-TPP islands were studied. Simulations were performed mimicking the occupancy of Fe on the molecular array to determine the average cluster size **s** of Fe on Co-TPP. XMCD measurements were done on the system to understand the magnetic interaction between Fe and the Co ion of Co-TPP. The magnetic moment of Co which was quenched on Ag(111) was revived after Fe deposition. XMCD also reveals a ferromagnetic coupling between the Fe and the Co. DFT calculations complimented the STM and XMCD measurements in finding the position of Fe on the Co-TPP macrocycle and the magnetic coupling Fe and Co.

5.4 Experimental and theoretical details

STM:

Co-TPP molecules were deposited by organic molecular beam epitaxy (OMBE) from a quartz crucible held at 625 K. Co-TPP was thoroughly degassed prior to any experiments resulting in a background pressure in the 10^{-10} mbar range during deposition. In our experiments we used Co-TPP acquired from a commercial supplier (Sigma-Aldrich) at 99.7% purity. After dosing Co-TPP at room temperature, the sample was cooled down and transferred into the STM chamber, where the Co-TPP array quality was checked by constant current images recorded at about 10 K using electrochemically etched tungsten tips. In the figure captions V_b refers to the bias voltage applied to the sample and I to the tunneling current. All the STM images were processed using the WsXM software. [32] Subsequently, Fe atoms were deposited in-situ, directly onto the cold sample, by thermal evaporation from a home-built water-cooled cell. Throughout the experiments, the evaporator was run at constant power while the Fe dose was augmented by increasing the deposition time.

XMCD

The XMCD measurements were preformed at the ID08 beam line at the European Synchrotron facility in Grenoble. The Ag(111) crystals have been cleaned by cycles of Ar-sputtering and annealing to 730K. For the Co-TPP, a multilayer of the metal organic complexes have been directly deposited on the sample at 300K. Annealing the sample to 525K leads to desorption of the multilayer leaving one complete monolayer on the sample surface It is important to note that this procedure ensures a full coverage of the Ag(111) one monolayer of a highly ordered Co-TPP network. Before the sample was transferred in-situ into the X-ray chamber, the sample quality was checked in-situ with an STM at room temperature. The X-ray adsorption measurements were performed at T= 8K with the measuring geometry sketched in the inset of Figure 5.8 a). First for every sample the X-ray absorption of the bare Co-TPP was measured and then Fe was deposited in-situ with the sample kept at 8K. For the measurement presented here the Fe coverage was $8\% \pm 2\%$ of a ML (with respect to the underlying Ag(111)). From the STM data we can estimate that every Co-center in the Co-TPP network is covered with an Fe-cluster having a mean size of 2 atoms per Co-TPP.

Computational methods (DFT + STM):

All calculations were performed using density functional theory as implemented in the VIENNA AB INITIO SIMULATION PACKAGE. [254] The VASP program uses a plane-wave basis set and a projector-augmented wave method to account for electron-ion interactions. The generalized-gradient approximation exchange-correlation functional parameterized by Perdew et al. [255] was employed and to consider long range interactions we used the semiempirical dispersion correction by Grimme [256] as it is implemented in VASP. The calculations were performed with spin polarization at a 300 eV energy cutoff. We considered a periodic slab of a Ag(111) surface with a size of $11 \times 5\sqrt{3}$ unit cells in lateral dimensions and a vacuum region of 19.3 Å which corresponds to approximately 6.5 unit cells. Only the top layer was relaxed to allow for interactions with the adsorbed molecule on one side of the slab. Because of the lateral size of the periodic cell, the k-point sampling was restricted to the Γ-point. The adsorption site for the Co-TPP molecule was determined prior Fe deposition to be a bridge site (BE (Co-TPP) = -4.6 eV and -2.8 eV for **HOMO** and **LUMO** with respect to vacuum) where the κ-pyr axis aligning with the closed-packed directions of the Ag lattice. Finally constant current STM images at - 0.2 V were calculated using Tersoff-Hamann theory [34] with a specific improvement of the wavefunction decay in the vacuum region. [257]

6 | Conclusion and perspectives

This thesis presented an in-depth study on three separate molecular systems that were used as platforms for the adsorption of molecules and atoms. Each of the platform served different purposes and was instrumental in advancing our understanding of atomic and molecular confinement experiments. Confinement of molecules were achieved through porous networks as well as using host platforms. A dense packed molecular layer is used for atomic confinement as well. Such confinement of nanoscale objects helps us to address the respective species on a single atom/molecule level. This becomes important when we want to understand the electronic properties of the isolated species and their response to external impulses.

Apart from the science of molecule-molecule and metal-molecule interactions, the experiments also served as an initial step towards the realization of potential applications like molecular rotor confinement, organic photovoltaic devices and magnetic arrays for information storage. An extension and improvisation of contemporary scientific knowledge is important in order to (*i*) enhance our understanding of the principles that govern the investigated system and (*ii*) exploiting those systems to achieve useful applications. [258] The topics presented motivate both these aspirations. Present day nanotechnology research, however, has become highly interdisciplinary and no single study is capable of providing all the information about a system. In this thesis too, our collaborators have provided noteworthy theoretical support and synchrotron experiment results to corroborate the main STM experiments. A brief summary of the three systems examined in this thesis and the respective perspectives is as follows:

- In the first study, a three-fold symmetric molecule with pyridyl substituents was studied on Ag(111) and Cu(111) surfaces. Extensive STM measurements were made on both surfaces with various molecular coverages. On Ag(111), it was observed that the molecule forms various interesting phases described as follows. Initially a close-packed network was observed that was stabilized solely by pyridyl-pyridyl interactions. Cu adatoms were deposited on the Ag surface to study the capability of the molecule to form metal-organic bonds. With increasing Cu adatom coverage, the molecule evidenced a coexistence of various patterns of extended metal-organic porous architectures on the Ag(111) surface. One interesting feature was that the molecule exhibited a combination of Cu-pyridyl and pyridyl-pyridyl interactions in almost all the phases except for one phase where only metal-organic interactions stabilized the porous network. Surprisingly, the molecule that appeared rigid on Ag(111) was observed to be flexible on Cu(111). This flexibility gave rise to certain interesting phenomenon. Porous networks were formed on Cu(111) that demonstrated also a simultaneous expression of Cu-pyridyl and pyridyl-pyridyl interactions. The networks on Cu(111) were seen to evidence short-range disordered networks, named as 2D short-range orientational and distortional disordered crystalline networks. Owing to the inherent flexibility (a distortion form the three-fold geometry) of the molecules, these pores also appeared flexible. This flexibility of the pores is an important criteria to confine molecular guests inside the pores, where the pores would adapt in size to fit the size of the guest species. As a proof of concept, a double decker complex was hosted in the pores created on the Cu(111) substrate.

The aspect of molecular flexibility could be put to good use when large organic molecules have to be confined and mechanically manipulated without being laterally translated on the surface. The confined molecular species could themselves be used as an individual podium to host a third molecule that is to be addressed individually. Thus a series of selective confinement of atomic or molecular species could be achieved with intelligent design of porous networks. On metal surfaces, porous networks have also been used to confine electron waves and the electronic coupling between the pores have been studied. [259] [260] The pattern of these confined waves could differ due to the shape of the pore, nature of the molecule used to form the porous network and the interactions that stabilize the network (metal-organic, van der Waals etc.). The influence of the confined electrons on the electronic structure of any guest molecule that is adsorbed within the pore is another interesting line of study.

- In the second study, $Ce(TPP)_2$ double decker complexes were deposited on an Ag(111) substrate and characterized topographically and electronically. The $Ce(TPP)_2$ forms dense packed islands that were used as a platform for confining C_{60} molecules. Depending on the annealing conditions, three different phases of $C_{60}/Ce(TPP)_2$ named α, β and γ were observed. Low temperature deposition of C_{60} lead to phase α, where isolated C_{60} molecules were found to be positioned on top of the double decker complex. The C_{60}s were addressed at a single molecule level in an attempt to understand their geometric and electronic structure. The confined C_{60}s were also manipulated mechanically to make a molecular switch. The Ag(111) sample which supported the phase α was annealed at room temperature to give phase β, which constituted an array of C_{60} molecules arranged on top of the double decker network. The arrays were composed of a corrugated arrangement of C_{60}s which evidenced interesting spectroscopic data. Annealing the sample containing phase β at 505 K gave rise to phase γ, which was a mixed architecture of C_{60} and $Ce(TPP)_2$. In phase γ, the C_{60}s as well as the $Ce(TPP)_2$ was in direct contact with the Ag(111) substrate. In this phase 8 C_{60} molecules surround a $Ce(TPP)_2$ complex and in this process, the $Ce(TPP)_2$ presumably undergoes an azimuthal rotation thereby facilitating a square like arrangement composed of 8 C_{60} neighbors.

This study offers diverse scope for further research, a few of which are described as follows.

(*i*) The principal idea of using an electron rich porphyrin based $Ce(TPP)_2$ and an electron accepting C_{60} is the realization of a potential organic photovoltaic system. In order to achieve this, the **LUMO** of the acceptor molecule has to be lower than that of the donor molecule. In this way it is energetically favorable to separate a photo generated exciton at the donor-acceptor interface so that the positive polaron goes the acceptor and the negative polaron to the donor. [261] Unfortunately this was not the case in the system presented in this thesis. The **LUMO** of the C_{60} on $Ce(TPP)_2$ was higher than that of the $Ce(TPP)_2$ complex. Even if charge separation takes place at the donor-acceptor interface, sufficient pathways must be established for the movement of positive and negative charges into the acceptor and donor molecules. This pathway is achieved through a charge transfer or in other words overlapping of molecular orbitals between the donor and acceptor. However **DFT** calculations reveal that the charge transfer between an individual C_{60} and a $Ce(TPP)_2$ complex is very negligible, which doesn't support the idea of efficient exciton movement. Considering the above issues, future directions to achieve a practical photovoltaic device that could be understood at a single molecule level would be to try various kinds of fullerene molecules (doped or extended) that would evidence a **LUMO** lower than the double decker complex and various lanthanide elements and the use of molecules other than porphyrins to build double deckers so that sufficient charge transfer could be established between the donor and acceptor.

(*ii*) Individual C_{60}s in phase α were probed with the STM tip to create a molecular switch. The mechanism of the switching phenomenon is still an unexplored area. For example the influence of the field created by the potential difference between the tip and the sample might influence the switching event more than the electrons injected into the C_{60} molecule. This could be clarified by making a thorough investigation of the influence of z dependence and influence of sample bias and tunneling current on the rate of switching.

(iii) In phase β, the bilayer C_{60} structure, the spectra evidences unexpected shifts in the position of unoccupied resonances. The effect of the neighbors on C_{60}s that are isolated from the substrate's influence and the effect of various double barrier heights on the spectra are interesting lines of study in this case.

(iv) Regarding phase γ, influence of the C_{60}s on the geometry of the $Ce(TPP)_2$ complex would be important to know, since the inherent flexibility of the $Ce(TPP)_2$ complex is made use of in this phase. Consequently, it would be intriguing to know the effect of the surrounding C_{60}s and also the $Ce(TPP)_2$ geometry on the electronic structure of the $Ce(TPP)_2$ complex. This might be understood with the help of additional **DFT** studies.

- In the third study, dense packed arrays of Co-TPP were anchored on an Ag(111) substrate and used as a receptor for capturing Fe atoms that were deposited in-situ at low temperatures. The Fe atoms were seen to be adsorbed on the macrocycle of the Co-TPP molecule. Topographic studies were performed on this system and the Fe was seen to occupy four distinct positions on the Co-TPP macrocycle. It was possible to switch the Fe between these four positions by manipulation with the STM tip thus exhibiting an atomic switch. Fe was studied on Co-TPP at various coverages. In order to study the influence of Fe on the magnetic properties of the Co ion of the Co-TPP, XMCD measurements were performed. The measurements revealed that the magnetization of the Co ion that was quenched upon adsorption on the surface, was revived after the deposition of Fe.

  The arrays of magnetic atoms conveniently arranged on the surface for individual addressing is achieved through this study. This uniform ordering of atoms is greatly assisted with the use of Co-TPP platforms. This is an initial step in tuning properties of atoms like oxidation states and spin density which might lead to an understanding of information storage systems. Future lines of research in this direction could include adsorption of magnetic atoms on double decker arrays, a combination of two different magnetic atoms and their interaction with one another, Kondo effect and the presence of gas molecules on magnetic atoms confined on metalloporphyrins.

In summary, we have investigated the three above mentioned bi-component systems in great detail for their interesting architecture, electronic properties and technological prospects. Extending these studies to include various atomic and molecular species would enhance the horizons of our scientific understanding regarding molecular confinement on surfaces and the nature of the interfaces and related properties therein.

Acknowledgements

First of all I would like to thank Prof. Dr. Johannes Barth for giving me the opportunity to pursue my work at the E20 in a wide range of interesting topics and for his ideas and guidance throughout my stay. Many thanks to Dr. Willi Auwärter who has been an invaluable supervisor for me, directing my research work correcting my mistakes and help me improve my skills in writing papers and in general all aspects of my scientific understanding. His impressive range of scientific ideas, creativity and in-depth understanding of the subject has been of great inspiration. I am extremely thankful to Dr. David Écija who has been a wonderful friend, mentor and scientific guide. David, you have played an irreplaceable role in the successful completion of all the experiments I have performed. Thanks for helping me with all the data analysis, patiently bearing all the mistakes and correcting me again and again. Thanks again for bringing a lively atmosphere to the office and sharing all the spanish stories!

I would like to thank all the members of the LT-STM lab, Knud Seufert, Sushobhan Joshi, Pepe Nacho, Alissa Wiengarten, Tobias Kaposi, Felix Bischoff and Julius Rombach. Thanks Sushobhan for showing me all the markets and shops and helping me settle down in Munich. Thanks Knud for the constant support and availability and helping with the scientific discussions. All the members together created a very exciting atmosphere in the lab where it was a constant pleasure to work.

Furthermore, special thanks goes to Ari P. Seitsonen who performed DFT calculation of the C_{60}/Ce(TPP)$_2$ system, Marie-Laure Bocquet and Torsten Houwaart who performed DFT calculations of the Fe/Co-TPP system and Pawel Szabelski, who performed Monte Carlo and Molecular Dynamics simulations of the threefold symmetric molecule. Their calculations helped inordinately to understand the behavior of these molecular systems.

Also many thanks to Uta Schlickum, Markus Etzkorn, Stefano Rusponi, Sebastian Stepanow and Harald Brune who along with Willi and Knud, performed the XMCD experiments of the Fe/Co-TPP system.

I am very thankful to our secretaries Kamila Wilson and Viktoria Blaschek for efficiently handling all the paper work and making my stay officially easy and comfortable. Thanks a lot to Max Glanz, Karl Eberle, Karl Kölbl and Reinhold Schneider who were always ready to help with any technical or administrative problem.

It was a pleasure to share the office with Sybille Fischer who made the office more fun and friendly. Thanks Sybille for sharing all the great travel stories, the million pictures and specially for the wonderful Käsespätzle that you always make and share.

Another special thanks goes to Peter Weber and Raphael Hellwig for welcoming me into their office in all the sunny and rainy afternoons and for the stimulating philosophical and humorous conversations. A personal thanks and appreciation to Andreas Kim, Nenad Kepčija, and Carlos-Andres Palma who have been very understanding friends whenever I needed to talk. This thanks also extends to all the E20 members for the support and the great intellectual atmosphere and making my years here a great experience!

Finally, the most important and special thanks goes to my parents S.S.Vijayaraghavan and V.Vijayalakshmi for always encouraging and supporting my education, hobbies and all my endeavors. Many many thanks also to my grandparents, brother and sister who were a constant source of support. Without their care, I would not have been able to get where I am today.

List of publications

- Petra Fesser, Cristian Iacovita, Christian Wäckerlin, Saranyan Vijayaraghavan, Nirmalya Ballav, Kara Howes, Jean-Paul Gisselbrecht, Maura Crobu, Corinne Boudon, Meike Stöhr, Thomas A. Jung, François Diederich. *Visualizing the Product of a Formal Cycloaddition of 7,7,8,8-Tetracyano-p-quinodimethane (TCNQ) to an Acetylene-Appended Porphyrin by Scanning Tunneling Microscopy on Au(111).* Chemistry - A European Journal , 17 (19) 5246-5250 (2011).

- David Écija, Willi Auwärter, Saranyan Vijayaraghavan, Knud Seufert, Felix Bischoff, Kentaro Tashiro, Johannes V. Barth. *Assembly and Manipulation of Rotatable Cerium Porphyrinato Sandwich Complexes on a Surface.* Angewandte Chemie International Edition, 50 (17), 3872-3877 (2011).

- Willi Auwärter, Knud Seufert, Felix Bischoff, David Écija, Saranyan Vijayaraghavan, Sushobhan Joshi, Florian Klappenberger, Niveditha Samudrala, Johannes V. Barth. *A surface-anchored molecular four-level conductance switch based on single proton transfer.* Nature Nanotechnology, 7, 41-46 (2011).

- David Écija, Saranyan Vijayaraghavan, Willi Auwärter, Sushobhan Joshi, Knud Seufert, Claudia Aurisicchio, Davide Bonifazi, and Johannes V. Barth. *Two-Dimensional Short-Range Disordered Crystalline Networks from Flexible Molecular Modules.* ACS Nano, 6 (5), pp 4258-4265 (2012).

- Saranyan Vijayaraghavan, David Écija, Willi Auwärter, Sushobhan Joshi, Knud Seufert, Ari P. Seitsonen, Kentaro Tashiro, and Johannes V. Barth. *Selective Supramolecular Fullerene-Porphyrin Interactions and Switching in Surface-Confined C_{60}-Ce(TPP)$_2$ Dyads.* Nano Lett., 12 (8), pp 4077-4083 (2012).

- Cristian Iacovita, Petra Fesser, Saranyan Vijayaraghavan, Mihaela Enache, Meike Stöhr, François Diederich, Thomas A. Jung. *Controlling the Dimensionality and Structure of Supramolecular Porphyrin Assemblies by their Functional Substituents: Dimers, Chains, and Close-Packed 2D Assemblies.* Chemistry - A European Journal, 18 (46), 14610-14613 (2012).

- Sushobhan Joshi, David Écija, Ralph Koitz, Marcella Iannuzzi, Ari P. Seitsonen, Jürg Hutter, Hermann Sachdev, Saranyan Vijayaraghavan, Felix Bischoff, Knud Seufert, Johannes V. Barth, Willi Auwärter. *Boron Nitride on Cu(111): An Electronically Corrugated Monolayer.* Nano Lett., 12 (11), pp 5821-5828 (2012).

- Felix Bischoff, Knud Seufert, Willi Auwärter, Sushobhan Joshi, Saranyan Vijayaraghavan, David Écija, Katharina Diller, Anthoula C. Papageorgiou, Sybille Fischer, Francesco Allegretti, David A. Duncan, Florian Klappenberger, Florian Blobner, Runyuan Han, Johannes V. Barth. *How Surface Bonding and Repulsive Interactions Cause Phase Transformations: Ordering of a Prototype Macrocyclic Compound on Ag(111).* ACS Nano, 7 (4), pp 3139-3149 (2013).

- David Écija, José I. Urgel, Anthoula C. Papageorgiou, Sushobhan Joshia, Willi Auwärter, Ari P. Seitsonenb, Svetlana Klyatskaya, Mario Ruben, Sybille Fischer, Saranyan Vijayaraghavan, Joachim Reicher, Johannes V. Barth. *Five-vertex Archimedean surface tessellation by lanthanide-directed molecular self-assembly.* PNAS, 110 (17), pp 6678-6681 (2013)

- Anthoula C. Papageorgiou, Sybille Fischer, Seung Cheol Oh, Özge Sağlam, Joachim Reichert, Alissa Wiengarten, Knud Seufert, Saranyan Vijayaraghavan, David Écija, Willi Auwärter, Francesco Allegretti, Robert G. Acres, Kevin C. Prince, Katharina Diller, Florian Klappenberger, and Johannes V. Barth. *Self-Terminating Protocol for an Interfacial Complexation Reaction in Vacuo by Metal-Organic Chemical Vapor Deposition.* ACS Nano, 7 (5), pp 4520-4526 (2013)

- Saranyan Vijayaraghavan, David Écija, Willi Auwärter, Sushobhan Joshi, Knud Seufert, Mateusz Drach, Damian Nieckarz, Pawel Szabelski, Claudia Aurisicchio, Davide Bonifaz and Johannes V. Barth. *2D interfacial nanoporous networks based on competing supramolecular interactions.* (Submitted to Chemistry: A European Journal)

- Knud Seufert, Willi Auwr̈ter, David Écija, Saranyan Vijayaraghavan, Sushobhan Joshi, F.J. Garcia de Abajo and Johannes V. Barth. *Controlled interaction of surface quantum-well electronic states.* (submitted to Physical Review Letters)

- Saranyan Vijayaraghavan, Willi Auwärter, David Écija, Knud Seufert, Uta Schlickum, Markus Etzkorn, Stefano Rusponi, Sebastian Stepanow, Torsten Houwaart, Philippe Sautet, Marie-Laure Bocquet, H. Brune, Johannes V. Barth. *Changing the magnetic moment of a Metalloporphyrin by site-selective positioning of Fe atoms* (In preparation)

- Torsten Houwaart, Marie-Laure Bocquet, Willi Auwärter, Saranyan Vijayaraghavan, David Écija, Knud Seufert and Johannes V. Barth. *Reversible atom switching in a surface anchored Fe/porphyrin dyad.* (In preparation)

Bibliography

[1] Feynman R.P. There's planety of room at the bottom. http://www.zyvex.com/nanotech/feynman.html.

[2] G. Binnig, H. Rohrer, C. Gerber, and E. Weibel. Surface studies by scanning tunneling microscopy. *Physical Review Letters*, 49(1):57–61, 1982.

[3] Donald M Eigler and Erhard K Schweizer. Positioning single atoms with a scanning tunnelling microscope. *Nature*, 344(6266):524–526, 1990.

[4] M.F. Crommie, C.P. Lutz, D.M. Eigler, et al. Confinement of electrons to quantum corrals on a metal surface. *Science*, 262(5131):218–220, 1993.

[5] http://www-03.ibm.com/press/us/en/pressrelease/40970.wss.

[6] Christopher R Moon, Laila S Mattos, Brian K Foster, Gabriel Zeltzer, and Hari C Manoharan. Quantum holographic encoding in a two-dimensional electron gas. *Nature nanotechnology*, 4(3):167–172, 2009.

[7] Arieh Aviram and Mark A Ratner. Molecular rectifiers. *Chemical Physics Letters*, 29(2):277–283, 1974.

[8] Mark A Reed, C Zhou, CJ Muller, TP Burgin, and JM Tour. Conductance of a molecular junction. *Science*, 278(5336):252–254, 1997.

[9] Kasper Moth-Poulsen and Thomas Bjørnholm. Molecular electronics with single molecules in solid-state devices. *Nature nanotechnology*, 4(9):551–556, 2009.

[10] LJ Lauhon and W Ho. Direct observation of the quantum tunneling of single hydrogen atoms with a scanning tunneling microscope. *Physical Review Letters*, 85(21):4566–4569, 2000.

[11] Leo Merz, Manfred Parschau, Laura Zoppi, Kim K Baldridge, Jay S Siegel, and Karl-Heinz Ernst. Reversible phase transitions in a buckybowl monolayer. *Angewandte Chemie International Edition*, 48(11):1966–1969, 2009.

[12] Tadahiro Komeda, Hironari Isshiki, Jie Liu, Yan-Feng Zhang, Nicolás Lorente, Keiichi Katoh, Brian K Breedlove, and Masahiro Yamashita. Observation and electric current control of a local spin in a single-molecule magnet. *Nature communications*, 2:217, January 2011.

[13] K Oura, VG Lifshits, AA Saranin, AV Zotov, M Katayama, and John T Yates. Surface science: An introduction. *Physics Today*, 57(10):79–80, 2004.

[14] *SPS-createc GmbH, Magnusstr. 11, 12489 Berlin, Germany, www.lt-stm.com.*

[15] http://www.avtservices.com.au/avt/turbo-molecular-pumps.

[16] S Chikkamaranahalli, R Ryan Vallance, Bradley N Damazo, Richard M Silver, and James D Gilsinn. Dynamic modeling and vibration analysis of a uhv scanning tunneling microscope. In *Proceedings of the Annual conference of the American Society for Precision Engineering (ASPE)*, 2005.

[17] G Binnig, H Rohrer, Ch Gerber, and E Weibel. 7× 7 reconstruction on si (111) resolved in real space. *Physical Review Letters*, 50(2):120–123, 1983.

[18] J.W.G. Wildoer, L.C. Venema, A.G. Rinzler, R.E. Smalley, and C. Dekker. Electronic structure of atomically resolved carbon nanotubes. *Nature*, 391(6662):59–62, 1998.

[19] JV Barth, H Brune, G Ertl, and RJ Behm. Scanning tunneling microscopy observations on the reconstructed au (111) surface: Atomic structure, long-range superstructure, rotational domains, and surface defects. *Physical Review B*, 42(15):9307, 1990.

[20] Régis Decker, Yang Wang, Victor W Brar, William Regan, Hsin-Zon Tsai, Qiong Wu, William Gannett, Alex Zettl, and Michael F Crommie. Local electronic properties of graphene on a bn substrate via scanning tunneling microscopy. *Nano letters*, 11(6):2291–2295, 2011.

[21] Xinghua Lu, M. Grobis, K. Khoo, Steven Louie, and M. Crommie. Spatially Mapping the Spectral Density of a Single C60 Molecule. *Physical Review Letters*, 90(9):7–10, March 2003.

[22] Sebastian Loth, Susanne Baumann, Christopher P Lutz, D M Eigler, and Andreas J Heinrich. Bistability in atomic-scale antiferromagnets. *Science (New York, N.Y.)*, 335(6065):196–9, January 2012.

[23] Michael Vershinin, Shashank Misra, S Ono, Y Abe, Yoichi Ando, and Ali Yazdani. Local ordering in the pseudogap state of the high-tc superconductor bi2sr2cacu2o8+ δ. *Science*, 303(5666):1995, 2004.

[24] Saw-Wai Hla, Kai-Felix Braun, Bernhard Wassermann, and Karl-Heinz Rieder. Controlled low-temperature molecular manipulation of sexiphenyl molecules on ag (111) using scanning tunneling microscopy. *Physical Review Letters*, 93(20):208302, 2004.

[25] Willi Auwärter, Knud Seufert, Felix Bischoff, David Ecija, Saranyan Vijayaraghavan, Sushobhan Joshi, Florian Klappenberger, Niveditha Samudrala, and Johannes V Barth. A surface-anchored molecular four-level conductance switch based on single proton transfer. *Nature nanotechnology*, 7(1):41–6, January 2012.

[26] L Niebergall, G Rodary, HF Ding, D Sander, VS Stepanyuk, P Bruno, and J Kirschner. Electron confinement in hexagonal vacancy islands: Theory and experiment. *Physical Review B*, 74(19):195436, 2006.

[27] Violeta Iancu, Aparna Deshpande, and Saw-Wai Hla. Manipulating kondo temperature via single molecule switching. *Nano letters*, 6(4):820–823, 2006.

[28] S Heinze, M Bode, A Kubetzka, O Pietzsch, X Nie, S Blügel, and R Wiesendanger. Real-space imaging of two-dimensional antiferromagnetism on the atomic scale. *Science*, 288(5472):1805–1808, 2000.

[29] C.J. Chen. *Introduction to Scanning Tunneling Microscopy*, volume 4. Oxford University Press, USA, 1993.

[30] J. Bardeen. Tunnelling from a many-particle point of view. *Phys. Rev. Lett.*, 6:57–59, Jan 1961.

[31] F. Besenbacher. Scanning tunnelling microscopy studies of metal surfaces. *Reports on Progress in Physics*, 59(12):1737, 1999.

[32] H. Lin, J.M.C. Rauba, K.S. Thygesen, K.W. Jacobsen, M.Y. Simmons, and W.A. Hofer. First-principles modelling of scanning tunneling microscopy using non-equilibrium green's functions. *Frontiers of Physics in China*, 5(4):369–379, 2010.

[33] E. Meyer, H.J. Hug, and R. Bennewitz. *Scanning probe microscopy: the lab on a tip.* Number 2674. Springer, 2003.

[34] J Tersoff and DR Hamann. Theory of the scanning tunneling microscope. *Physical Review B*, 31(2), 1985.

[35] Y Hasegawa and Ph Avouris. Direct observation of standing wave formation at surface steps using scanning tunneling spectroscopy. *Physical Review Letters*, 71(7):1071–1074, 1993.

[36] Carlos Javier Villagomez, Tomaso Zambelli, Sébastien Gauthier, André Gourdon, Sladjana Stojkovic, and Christian Joachim. Stm images of a large organic molecule adsorbed on a bare metal substrate or on a thin insulating layer: Visualization of homo and lumo. *Surface Science*, 603(10):1526–1532, 2009.

[37] Jascha Repp, Gerhard Meyer, Sladjana M Stojković, André Gourdon, and Christian Joachim. Molecules on insulating films: Scanning-tunneling microscopy imaging of individual molecular orbitals. *Physical Review Letters*, 94(2):26803, 2005.

[38] Marie-Christine Blüm. *Supramolecular assembly, chirality, and electronic properties of rubrene studied by STM and STS.* PhD thesis, EPFL, Lausanne, 2006.

[39] Franz J. Giessibl. Advances in atomic force microscopy. *Reviews of Modern Physics*, 75:949–983, Jul 2003.

[40] Gerhard Meyer, Sven Zöphel, and Karl-Heinz Rieder. Scanning tunneling microscopy manipulation of native substrate atoms: A new way to obtain registry information on foreign adsorbates. *Physical Review Letters*, 77:2113–2116, Sep 1996.

[41] K. Besocke. An easily operable scanning tunneling microscope. *Surface Science*, 181(1):145–153, 1987.

[42] Alexander Weber Bargioni. *Supramolecular organization, conformation and electronic properties of porphyrin molecules on metal substrates.* PhD thesis, University of British Columbia, 2007.

[43] Philip Willmott. *An introduction to synchrotron radiation: techniques and applications.* Wiley, 2011.

[44] Junko Yano and Vittal K Yachandra. X-ray absorption spectroscopy. *Photosynthesis Research*, 102(2-3):241–254, 2009.

[45] J Stöhr. X-ray magnetic circular dichroism spectroscopy of transition metal thin films. *Journal of Electron Spectroscopy and Related Phenomena*, 75:253–272, 1995.

[46] HyperChem(TM) Professional 7.51, Hypercube, Inc., 1115 NW 4th Street, Gainesville, Florida 32601, USA.

[47] Roald Hoffmann. An extended hückel theory. i. hydrocarbons. *The Journal of Chemical Physics*, 39:1397, 1963.

[48] Diego Kienle, Jorge I Cerda, and Avik W Ghosh. Extended hückel theory for band structure, chemistry, and transport. i. carbon nanotubes. *Journal of Applied Physics*, 100(4):043714–043714, 2006.

[49] O. Gröning and R. Fasel. *STM generator software, EMPA Material Science and Technology, Switzerland (2004).*

[50] Fabio Cicoira, Clara Santato, and Federico Rosei. Two-dimensional nanotemplates as surface cues for the controlled assembly of organic molecules. In *STM and AFM Studies on (Bio) molecular Systems: Unravelling the Nanoworld*, pages 203–267. Springer, 2008.

[51] Xibin Zhou, Guande Liu, Kazuhiro Yamato, Yi Shen, Ruixian Cheng, Xiaoxi Wei, Wanli Bai, Yi Gao, Hui Li, Yi Liu, et al. Self-assembling subnanometer pores with unusual mass-transport properties. *Nature Communications*, 3:949, 2012.

[52] A Vallés Lluch, A Campillo Fernández, G Gallego Ferrer, and M Monleón Pradas. Bioactive scaffolds mimicking natural dentin structure. *Journal of Biomedical Materials Research Part B: Applied Biomaterials*, 90(1):182–194, 2008.

[53] Simon Scheuring, James N Sturgis, Valerie Prima, Alain Bernadac, Daniel Lévy, and Jean-Louis Rigaud. Watching the photosynthetic apparatus in native membranes. *Proceedings of the National Academy of Sciences of the United States of America*, 101(31):11293–11297, 2004.

[54] http://coral.aims.gov.au.

[55] Matthias Michalek, Frank D Sönnichsen, Rainer Wechselberger, Andrew J Dingley, Chien-Wen Hung, Annika Kopp, Hans Wienk, Maren Simanski, Rosa Herbst, Inken Lorenzen, et al. Structure and function of a unique pore-forming protein from a pathogenic acanthamoeba. *Nature Chemical Biology*, 2012.

[56] Ying Wan, Haifeng Yang, and Dongyuan Zhao. "host-guest" chemistry in the synthesis of ordered nonsiliceous mesoporous materials. *Accounts of Chemical Research*, 39(7):423–432, 2006.

[57] Christer B Aakeröy, Alicia M Beatty, and Destin S Leinen. A versatile route to porous solids: organic–inorganic hybrid materials assembled through hydrogen bonds. *Angewandte Chemie International Edition*, 38(12):1815–1819, 1999.

[58] Rongmin Yu, Xiao-Fei Kuang, Xiao-Yuan Wu, Can-Zhong Lu, and James P Donahue. Stabilization and immobilization of polyoxometalates in porous coordination polymers through host–guest interactions. *Coordination Chemistry Reviews*, 253(23):2872–2890, 2009.

[59] Myunghyun Paik Suh, Young Eun Cheon, and Eun Young Lee. Syntheses and functions of porous metallosupramolecular networks. *Coordination Chemistry Reviews*, 252(8):1007–1026, 2008.

[60] Carlos-Andres Palma, Massimo Bonini, Anna Llanes-Pallas, Thomas Breiner, Maurizio Prato, Davide Bonifazi, and Paolo Samorì. Pre-programmed bicomponent porous networks at the solid–liquid interface: the low concentration regime. *Chemical Communications*, (42):5289–5291, 2008.

[61] Stephan Hermes, Marie-Katrin Schröter, Rochus Schmid, Lamma Khodeir, Martin Muhler, Arno Tissler, Richard W Fischer, and Roland A Fischer. Metal@ mof: Loading of highly porous coordination polymers host lattices by metal organic chemical vapor deposition. *Angewandte Chemie International Edition*, 44(38):6237–6241, 2005.

[62] Alicia M Beatty. Open-framework coordination complexes from hydrogen-bonded networks: toward host/guest complexes. *Coordination Chemistry Reviews*, 246(1):131–143, 2003.

[63] Matthias Böhringer, Karina Morgenstern, Wolf-Dieter Schneider, Richard Berndt, Francesco Mauri, Alessandro De Vita, and Roberto Car. Two-dimensional self-assembly of supramolecular clusters and chains. *Physical Review Letters*, 83(2):324–327, 1999.

[64] Satoshi Yasuda, Koji Miyake, Jun Sumaoka, Makoto Komiyama, and Hidemi Shigekawa. Effect of the dipole-dipole interaction on the self-assembly of cyclodextrin inclusion complexes. *Japanese Journal of Applied Physics*, 38(part 1):3888–3891, 1999.

[65] Mohamed Eddaoudi, David B Moler, Hailian Li, Banglin Chen, Theresa M Reineke, Michael O'keeffe, and Omar M Yaghi. Modular chemistry: secondary building units as a basis for the design of highly porous and robust metal-organic carboxylate frameworks. *Accounts of Chemical Research*, 34(4):319–330, 2001.

[66] Hailin Liang, Yang He, Yingchun Ye, Xiaoguang Xu, Fang Cheng, Wei Sun, Xiang Shao, Yongfeng Wang, Jianlong Li, and Kai Wu. Two-dimensional molecular porous networks constructed by surface assembling. *Coordination Chemistry Reviews*, 253(23):2959–2979, 2009.

[67] Johannes V Barth. Molecular architectonic on metal surfaces. *Annual Review of Physical Chemistry*, 58:375–407, January 2007.

[68] RE Palmer and PJ Rous. Resonances in electron scattering by molecules on surfaces. *Reviews of Modern Physics*, 64(2):383, 1992.

[69] Wesley R Browne and Ben L Feringa. Light switching of molecules on surfaces. *Annual Review of Physical Chemistry*, 60:407–428, 2009.

[70] PD Johnson and SL Hulbert. Inverse-photoemission studies of adsorbed diatomic molecules. *Physical Review B*, 35(18):9427, 1987.

[71] Shengbin Lei, Kazukuni Tahara, Xinliang Feng, Shuhei Furukawa, Frans C De Schryver, Klaus Müllen, Yoshito Tobe, and Steven De Feyter. Molecular clusters in two-dimensional surface-confined nanoporous molecular networks: Structure, rigidity, and dynamics. *Journal of the American Chemical Society*, 130(22):7119–7129, 2008.

[72] http://www.freegreatpicture.com/animal-collection/bees-and-honeycomb-21462.

[73] David Ecija, Saranyan Vijayaraghavan, Willi Auwärter, Sushobhan Joshi, Knud Seufert, Claudia Aurisicchio, Davide Bonifazi, and Johannes V Barth. Two-dimensional short-range disordered crystalline networks from flexible molecular modules. *ACS nano*, 6(5):4258–4265, 2012.

[74] S.L. Tait, a. Langner, N. Lin, S. Stepanow, C. Rajadurai, M. Ruben, and K. Kern. One-Dimensional Self-Assembled Molecular Chains on Cu(100): Interplay between Surface-Assisted Coordination Chemistry and Substrate Commensurability. *Journal of Physical Chemistry C*, 111(29):10982–10987, July 2007.

[75] M Eichberger, M Marschall, J Reichert, a Weber-Bargioni, W Auwärter, R L C Wang, H J Kreuzer, Y Pennec, a Schiffrin, and J V Barth. Dimerization boosts one-dimensional mobility of conformationally adapted porphyrins on a hexagonal surface atomic lattice. *Nano letters*, 8(12):4608–13, December 2008.

[76] Daniel Heim, Knud Seufert, Willi Auwärter, Claudia Aurisicchio, Chiara Fabbro, Davide Bonifazi, and Johannes V Barth. Surface-assisted assembly of discrete porphyrin-based cyclic supramolecules. *Nano letters*, 10(1):122–128, 2009.

[77] Daniel Heim, David Ecija, Knud Seufert, Willi Auwärter, Claudia Aurisicchio, Chiara Fabbro, Davide Bonifazi, and Johannes V Barth. Self-assembly of flexible one-dimensional coordination polymers on metal surfaces. *Journal of the American Chemical Society*, 132(19):6783–90, May 2010.

[78] Ziliang Shi, Jun Liu, Tao Lin, Fei Xia, Pei Nian Liu, and Nian Lin. Thermodynamics and selectivity of two-dimensional metallo-supramolecular self-assembly resolved at molecular scale. *J. Am. Chem. Soc*, 133(16):6150–6153, 2011.

[79] Jun Liu, Tao Lin, Ziliang Shi, Fei Xia, Lei Dong, Pei Nian Liu, and Nian Lin. Structural transformation of two-dimensional metal-organic coordination networks driven by intrinsic in-plane compression. *Journal of the American Chemical Society*, 133(46):18760–6, November 2011.

[80] Yang Li, Jie Xiao, Tatyana E Shubina, Min Chen, Ziliang Shi, Martin Schmid, Hans-Peter Steinr§ck, J Michael Gottfried, and Nian Lin. Coordination and metalation bifunctionality of cu with 5, 10, 15, 20-tetra (4-pyridyl) porphyrin: Toward a mixed-valence two-dimensional coordination network. *Journal of the American Chemical Society*, 134(14):6401, 2012.

[81] Xu Zhang, Ting Chen, Hui-Juan Yan, Dong Wang, Qing-Hua Fan, Li-Jun Wan, Koushik Ghosh, Hai-Bo Yang, and Peter J Stang. Engineering of linear molecular nanostructures by a hydrogen-bond-mediated modular and flexible host- guest assembly. *ACS nano*, 4(10):5685–5692, 2010.

[82] Nenad Kepčija, Yi-Qi Zhang, Martin Kleinschrodt, Jonas Björk, Svetlana Klyatskaya, Florian Klappenberger, Mario Ruben, and Johannes V Barth. Steering on-surface self-assembly of high-quality hydrocarbon networks with terminal alkynes. *The Journal of Physical Chemistry C*, 2013.

[83] Carlos-Andres Palma, Marco Cecchini, and Paolo Samorì. Predicting

self-assembly: from empirism to determinism. *Chemical Society Reviews*, 41(10):3713–3730, 2012.

[84] Thomas Classen, Guido Fratesi, Giovanni Costantini, Stefano Fabris, Frank Louis Stadler, Cheolkyu Kim, Stefano de Gironcoli, Stefano Baroni, and Klaus Kern. Templated growth of metal–organic coordination chains at surfaces. *Angewandte Chemie*, 117(38):6298–6301, 2005.

[85] Tibor Kudernac, Shengbin Lei, Johannes a a W Elemans, and Steven De Feyter. Two-dimensional supramolecular self-assembly: nanoporous networks on surfaces. *Chemical Society Reviews*, 38(2):402–21, February 2009.

[86] Christoph Meier, Ulrich Ziener, Katharina Landfester, and Petra Weihrich. Weak hydrogen bonds as a structural motif for two-dimensional assemblies of oligopyridines on highly oriented pyrolytic graphite: An stm investigation. *The Journal of Physical Chemistry B*, 109(44):21015–21027, 2005.

[87] Yang Li and Nian Lin. Combined scanning tunneling microscopy and kinetic monte carlo study on kinetics of cu-coordinated pyridyl-porphyrin supramolecular self-assembly on a au(111) surface. *Phys. Rev. B*, 84:125418, Sep 2011.

[88] David Van Der Spoel, Erik Lindahl, Berk Hess, Gerrit Groenhof, Alan E Mark, and Herman JC Berendsen. Gromacs: fast, flexible, and free. *Journal of Computational Chemistry*, 26(16):1701–1718, 2005.

[89] Berk Hess, Carsten Kutzner, David van der Spoel, and Erik Lindahl. Gromacs 4: Algorithms for highly efficient, load-balanced, and scalable molecular simulation. *Journal of chemical theory and computation*, 4(3):435–447, 2008.

[90] F Iori, R Di Felice, E Molinari, and S Corni. Golp: An atomistic force-field to describe the interaction of proteins with au (111) surfaces in water. *Journal of Computational Chemistry*, 30(9):1465–1476, 2008.

[91] Vincenzo Barone, Maurizio Casarin, Daniel Forrer, Susanna Monti, and Giacomo Prampolini. Molecular dynamics simulations of the self-assembly of tetraphenylporphyrin-based monolayers and bilayers at a silver interface. *The Journal of Physical Chemistry C*, 115(38):18434–18444, 2011.

[92] Paweł Szabelski, Steven De Feyter, Mateusz Drach, and Shengbin Lei. Computer simulation of chiral nanoporous networks on solid surfaces. *Langmuir : The ACS Journal of Surfaces and Colloids*, 26(12):9506–15, June 2010.

[93] P Szabelski and Steven De Feyter. Chiral occlusion in two-dimensional binary supramolecular networks studied by the Monte Carlo method. *CrystEngComm*, 13(18), 2011.

[94] C Austen Angell. Formation of glasses from liquids and biopolymers. *Science*, 267(5206):1924–1935, 1995.

[95] Pablo G Debenedetti, Frank H Stillinger, et al. Supercooled liquids and the glass transition. *Nature*, 410(6825):259–267, 2001.

[96] David Chandler. Liquids: Condensed, disordered, and sometimes complex. *Proceedings of the National Academy of Sciences*, 106(36):15111–15112, 2009.

[97] D Shechtman, Ilan Blech, Denis Gratias, and John W Cahn. Metallic phase with long-range orientational order and no translational symmetry. *Physical*

Review Letters, 53(20):1951–1953, 1984.

[98] Andrea Ilari and Carmelinda Savino. Protein structure determination by x-ray crystallography. *METHODS IN MOLECULAR BIOLOGY-CLIFTON THEN TOTOWA-*, 452:63, 2008.

[99] Elizabeth E Fry, Jonathan Grimes, and David I Stuart. Virus crystallography. *Molecular Biotechnology*, 12(1):13–23, 1999.

[100] Walter Steurer and Sofia Deloudi. Fascinating quasicrystals. *Acta Crystallographica Section A: Foundations of Crystallography*, 64(1):1–11, 2007.

[101] Richard Zallen and John Wiley. *The physics of amorphous solids*, volume 26. Wiley Online Library, 1983.

[102] Keiichiro Adachi, Hiroshi Suga, and Syûzô Seki. Phase changes in crystalline and glassy-crystalline cyclohexanol. *Bulletin of the Chemical Society of Japan*, 41(5):1073–1087, 1968.

[103] M Foulon, JP Amoureux, JL Sauvajol, J Lefebvre, and M Descamps. Evidence of a'glassy crystal'phase obtained by the quenching of the plastic phase of the cyanoadamantane. *Journal of Physics C Solid State Physics*, 16:L265–L269, 1983.

[104] K Pathmanathan and GP Johari. Molecular relaxations in a rigid molecular glassy crystal. *Journal of Physics. C. Solid State Physics*, 18(35):6535–6545, 1985.

[105] J Lefebvre, JP Rolland, JL Sauvajol, and B Hennion. Coherent neutron scattering on the'glassy crystal'of cyanoadamantane. *Journal of Physics C Solid State Physics*, 18:241–255, 1985.

[106] M Descamps, JF Willart, and O Delcourt. Molecular and structural relaxations in a glassy crystal. *Physica A: Statistical Mechanics and its Applications*, 201(1):346–362, 1993.

[107] JF Willart, M Descamps, and N Benzakour. Polymorphism of a glass forming plastic crystal: A kinetic investigation. *The Journal of Chemical Physics*, 104:2508, 1996.

[108] O Delcourt, M Descamps, J Even, M Bertault, and JF Willart. Peculiarities of the enthalpy relaxation of a glassy crystal. *Chemical Physics*, 215(1):51–57, 1997.

[109] Bogdan Kuchta, Marc Descamps, and Frédéric Affouard. A monte carlo study of metastable structures of the cyanoadamantane crystal. *The Journal of Chemical Physics*, 109(16):6753–6763, 1998.

[110] R Brand, P Lunkenheimer, and A Loidl. Relaxation dynamics in plastic crystals. *The Journal of Chemical Physics*, 116:10386, 2002.

[111] Roberto Otero, Maya Lukas, Ross EA Kelly, Wei Xu, Erik Lægsgaard, Ivan Stensgaard, Lev N Kantorovich, and Flemming Besenbacher. Elementary structural motifs in a random network of cytosine adsorbed on a gold (111) surface. *Science*, 319(5861):312–315, 2008.

[112] Matthias Marschall, Joachim Reichert, Alexander Weber-Bargioni, Knud Seufert, Willi Auwärter, Svetlana Klyatskaya, Giorgio Zoppellaro, Mario

Ruben, and Johannes V Barth. Random two-dimensional string networks based on divergent coordination assembly. *Nature Chemistry*, 2(2):131–137, 2010.

[113] Matthew O Blunt, James C Russell, María del Carmen Giménez-López, Juan P Garrahan, Xiang Lin, Martin Schröder, Neil R Champness, and Peter H Beton. Random tiling and topological defects in a two-dimensional molecular network. *Science*, 322(5904):1077–1081, 2008.

[114] Marina Pivetta, Marie-Christine Blüm, François Patthey, and Wolf-Dieter Schneider. Two-dimensional tiling by rubrene molecules self-assembled in supramolecular pentagons, hexagons, and heptagons on a au (111) surface. *Angewandte Chemie*, 120(6):1092–1095, 2007.

[115] G M Whitesides, J P Mathias, and C T Seto. Molecular self-assembly and nanochemistry: a chemical strategy for the synthesis of nanostructures. *Science (New York, N.Y.)*, 254(5036):1312–9, November 1991.

[116] Richard W Kriwacki, Ludger Hengst, Linda Tennant, Steven I Reed, and Peter E Wright. Structural studies of p21waf1/cip1/sdi1 in the free and cdk2-bound state: conformational disorder mediates binding diversity. *Proceedings of the National Academy of Sciences*, 93(21):11504–11509, 1996.

[117] Tanja Mittag, Lewis E Kay, and Julie D Forman-Kay. Protein dynamics and conformational disorder in molecular recognition. *Journal of Molecular Recognition*, 23(2):105–116, 2009.

[118] Satoshi Horike, Satoru Shimomura, and Susumu Kitagawa. Soft porous crystals. *Nature chemistry*, 1(9):695–704, 2009.

[119] David Ecija, Knud Seufert, Daniel Heim, Willi Auwärter, Claudia Aurisicchio, Chiara Fabbro, Davide Bonifazi, and Johannes V Barth. Hierarchic self-assembly of nanoporous chiral networks with conformationally flexible porphyrins. *ACS nano*, 4(8):4936–42, August 2010.

[120] Luc Piot, Fabien Silly, Ludovic Tortech, Yohann Nicolas, Philippe Blanchard, Jean Roncali, and Denis Fichou. Long-range alignments of single fullerenes by site-selective inclusion into a double-cavity 2d open network. *Journal of the American Chemical Society*, 131(36):12864–12865, 2009.

[121] According to Ernest L. Eliel and Samuel H. Wilen in Stereochemistry of Organic Compounds (1994, p. 20-19), "the most fundamental distinction one can make between configuration and conformation, is to say that configurational differences imply differences in bond angles, whereas conformational differences involve differences in torsion angles (including in both case, differences, that are exclusively in sign)." Based on this distinction, isolable molecules of identical constitution but differing in bond angles under the current instrumental conditions can be thus considered configurational isomers.

[122] CC Perry, S Haq, BG Frederick, and NV Richardson. Face specificity and the role of metal adatoms in molecular reorientation at surfaces. *Surface science*, 409(3):512–520, 1998.

[123] U Schlickum, R Decker, F Klappenberger, G Zoppellaro, S Klyatskaya, M Ruben, I Silanes, A Arnau, K Kern, H Brune, et al. Metal-organic honeycomb nanomeshes with tunable cavity size. *Nano letters*, 7(12):3813–3817,

2007.

[124] F Klappenberger, A Weber-Bargioni, W Auwärter, M Marschall, A Schiffrin, and JV Barth. Temperature dependence of conformation, chemical state, and metal-directed assembly of tetrapyridyl-porphyrin on cu (111). *The Journal of Chemical Physics*, 129:214702, 2008.

[125] Carlos-Andres Palma, Jonas Bjork, Massimo Bonini, Matthew S Dyer, Anna Llanes-Pallas, Davide Bonifazi, Mats Persson, and Paolo SamorŞ. Tailoring bicomponent supramolecular nanoporous networks: Phase segregation, polymorphism, and glasses at the solid- liquid interface. *Journal of the American Chemical Society*, 131(36):13062–13071, 2009.

[126] Xiang Yang Liu and Jim De Yoreo. *Nanoscale Structure and Assembly at Solid-fluid Interfaces: Assembly in hybrid and biological systems.* Springer London, 2004.

[127] Wesley R Browne and Ben L Feringa. Making molecular machines work. *Nature nanotechnology*, 1(1):25–35, 2006.

[128] Josef Michl and E Charles H Sykes. Molecular rotors and motors: recent advances and future challenges. *ACS nano*, 3(5):1042–1048, 2009.

[129] David Écija, Willi Auwärter, Saranyan Vijayaraghavan, Knud Seufert, Felix Bischoff, Kentaro Tashiro, and Johannes V Barth. Assembly and manipulation of rotatable cerium porphyrinato sandwich complexes on a surface. *Angewandte Chemie (International ed. in English)*, 50(17):3872–7, April 2011.

[130] Masato Ikeda, Masayuki Takeuchi, Seiji Shinkai, Fumito Tani, and Yoshinori Naruta. Synthesis of new diaryl-substituted triple-decker and tetraaryl-substituted double-decker lanthanum (iii) porphyrins and their porphyrin ring rotational speed as compared with that of double-decker cerium (iv) porphyrins. *Bulletin of the Chemical Society of Japan*, 74(4):739–746, 2001.

[131] Joe Otsuki, Satoru Kawaguchi, Toshihisa Yamakawa, Masumi Asakawa, and Koji Miyake. Arrays of double-decker porphyrins on highly oriented pyrolytic graphite. *Langmuir*, 22(13):5708–5715, 2006.

[132] Koji Miyake, Megumi Fukuta, Masumi Asakawa, Yukari Hori, Taichi Ikeda, and Toshimi Shimizu. Molecular motion of surface-immobilized double-decker phthalocyanine complexes. *Journal of the American Chemical Society*, 131(49):17808–17813, 2009.

[133] Joe Otsuki, Yuji Komatsu, Daiya Kobayashi, Masumi Asakawa, and Koji Miyake. Rotational libration of a double-decker porphyrin visualized. *Journal of the American Chemical Society*, 132(20):6870–6871, 2010.

[134] Saranyan Vijayaraghavan, David Écija, Willi Auwärter, Sushobhan Joshi, Knud Seufert, Ari P Seitsonen, Kentaro Tashiro, and Johannes V Barth. Selective supramolecular fullerene-porphyrin interactions and switching in surface-confined C60-Ce(TPP)2 dyads. *Nano letters*, 12(8):4077–83, August 2012.

[135] Lionel R Milgrom and Martin J Warren. *The colours of life: an introduction to the chemistry of porphyrins and related compounds.* Oxford University Press New York., 1997.

[136] Dayong Sun, Fook S Tham, Christopher A Reed, and Peter DW Boyd. Extend-

ing supramolecular fullerene-porphyrin chemistry to pillared metal-organic frameworks. *Proceedings of the National Academy of Sciences*, 99(8):5088–5092, 2002.

[137] Kazuya Ogawa and Yoshiaki Kobuke. Formation of a giant supramolecular porphyrin array by self-coordination. *Angewandte Chemie International Edition*, 39(22):4070–4073, 2000.

[138] James P Collman, Jonathan L Kendall, Judy L Chen, KA Collins, and Jean-Claude Marchon. Formation of charge-transfer complexes from neutral bis (porphyrin) sandwiches. *Inorganic Chemistry*, 39(8):1661–1667, 2000.

[139] Wayne M Campbell, Anthony K Burrell, David L Officer, and Kenneth W Jolley. Porphyrins as light harvesters in the dye-sensitised tio< sub> 2</sub> solar cell. *Coordination Chemistry Reviews*, 248(13):1363–1379, 2004.

[140] Xuebing Leng, Chi-Fung Choi, Pui-Chi Lo, and Dennis KP Ng. Assembling a mixed phthalocyanine-porphyrin array in aqueous media through host-guest interactions. *Organic Letters*, 9(2):231–234, 2007.

[141] Johann Deisenhofer, James R Norris, et al. *The photosynthetic reaction center. Volume 1.* Academic Press Inc., 1993.

[142] Aiko Kira, Tomokazu Umeyama, Yoshihiro Matano, Kaname Yoshida, Seiji Isoda, Jong Kang Park, Dongho Kim, and Hiroshi Imahori. Supramolecular donor- acceptor heterojunctions by vectorial stepwise assembly of porphyrins and coordination-bonded fullerene arrays for photocurrent generation. *Journal of the American Chemical Society*, 131(9):3198–3200, 2009.

[143] Hsueh-Pei Lu, Chen-Yuan Tsai, Wei-Nan Yen, Chou-Pou Hsieh, Cheng-Wei Lee, Chen-Yu Yeh, and Eric Wei-Guang Diau. Control of dye aggregation and electron injection for highly efficient porphyrin sensitizers adsorbed on semiconductor films with varying ratios of coadsorbate. *The Journal of Physical Chemistry C*, 113(49):20990–20997, 2009.

[144] Takeru Bessho, Shaik M Zakeeruddin, Chen-Yu Yeh, Eric Wei-Guang Diau, and Michael Grätzel. Highly efficient mesoscopic dye-sensitized solar cells based on donor–acceptor-substituted porphyrins. *Angewandte Chemie International Edition*, 49(37):6646–6649, 2010.

[145] James P Kirby, Niels A van Dantzig, Chi K Chang, and Daniel G Nocera. Formation of porphyrin donor-acceptor complexes via an amidinium-carboxylate salt bridge. *Tetrahedron letters*, 36(20):3477–3480, 1995.

[146] Naoto Ishikawa, Miki Sugita, Tadahiko Ishikawa, Shin-Ya Koshihara, and Youkoh Kaizu. Lanthanide double-decker complexes functioning as magnets at the single-molecular level. *Journal of the American Chemical Society*, 125(29):8694–5, July 2003.

[147] Lapo Bogani and Wolfgang Wernsdorfer. Molecular spintronics using single-molecule magnets. *Nature materials*, 7(3):179–86, March 2008.

[148] Ludovica Margheriti, Daniele Chiappe, Matteo Mannini, Pierre-E Car, Philippe Sainctavit, Marie-Anne Arrio, Francesco Buatier de Mongeot, Julio C Cezar, Federica M Piras, Agnese Magnani, et al. X-ray detected magnetic hysteresis of thermally evaporated terbium double-decker oriented films. *Advanced Materials*, 22(48):5488–5493, 2010.

[149] Gérard Guillaud, Manaa Al Sadoun, Monique Maitrot, Jacques Simon, and Marcel Bouvet. Field-effect transistors based on intrinsic molecular semiconductors. *Chemical Physics Letters*, 167(6):503–506, 1990.

[150] S Shinkai, M Ikeda, a Sugasaki, and M Takeuchi. Positive allosteric systems designed on dynamic supramolecular scaffolds: toward switching and amplification of guest affinity and selectivity. *Accounts of Chemical Research*, 34(6):494–503, June 2001.

[151] Zhiming Liu, Amir a Yasseri, Jonathan S Lindsey, and David F Bocian. Molecular memories that survive silicon device processing and real-world operation. *Science (New York, N.Y.)*, 302(5650):1543–5, November 2003.

[152] Yongzhong Bian, Jianzhuang Jiang, Ye Tao, Michael TM Choi, Renjie Li, Anthony CH Ng, Peihua Zhu, Na Pan, Xuan Sun, Dennis P Arnold, et al. Tuning the valence of the cerium center in (na) phthalocyaninato and porphyrinato cerium double-deckers by changing the nature of the tetrapyrrole ligands. *Journal of the American Chemical Society*, 125(40):12257–12267, 2003.

[153] John K Duchowski and David F Bocian. Effects of. pi.. pi. interaction on the electronic properties of asymmetrical lanthanide porphyrin sandwich complexes. *Inorganic Chemistry*, 29(20):4158–4160, 1990.

[154] Masato Ikeda, Tomoyuki Tanida, Masayuki Takeuchi, and Seiji Shinkai. Allosteric silver (i) ion binding with peripheral π clefts of a ce (iv) double decker porphyrin. *Organic letters*, 2(13):1803–1805, 2000.

[155] Koen Binnemans, Jurgen Sleven, Steven De Feyter, Frans C De Schryver, Bertrand Donnio, and Daniel Guillon. Structure and mesomorphic behavior of alkoxy-substituted bis (phthalocyaninato) lanthanide (iii) complexes. *Chemistry of materials*, 15(20):3930–3938, 2003.

[156] R. E. Haufler, Y. Chai, L. P. F. Chibante, J. Conceicao, Changming Jin, Lai-Sheng Wang, Shigeo Maruyama, and R. E. Smalley. Carbon arc generation of c60. *MRS Proceedings*, 206, 0 1990.

[157] RC Haddon, RE Palmer, HW Kroto, and PA Sermon. The fullerenes: Powerful carbon-based electron acceptors [and discussion]. *Philosophical Transactions of the Royal Society of London. Series A: Physical and Engineering Sciences*, 343(1667):53–62, 1993.

[158] Lai-Sheng Wang, J Conceicao, Changming Jin, and RE Smalley. Threshold photodetachment of cold c60. *Chemical Physics Letters*, 182(1):5–11, 1991.

[159] RC Haddon. Electronic structure, conductivity and superconductivity of alkali metal doped (c60). *Accounts of Chemical Research*, 25(3):127–133, 1992.

[160] François Diederich and Marcos Gómez-López. Supramolecular fullerene chemistry. *Chem. Soc. Rev.*, 28(5):263–277, 1999.

[161] I. Fernández Torrente, K.J. Franke, and J. Ignacio Pascual. Spectroscopy of C60 single molecules: the role of screening on energy level alignment. *Journal of Physics: Condensed Matter*, 20:184001, 2008.

[162] R Hesper, LH Tjeng, and GA Sawatzky. Strongly reduced band gap in a correlated insulator in close proximity to a metal. *EPL (Europhysics Letters)*, 40(2):177, 2007.

[163] C Rogero, JI Pascual, J Gomez-Herrero, and AM Baro. Resolution of site-specific bonding properties of c adsorbed on au (111). *The Journal of Chemical Physics*, 116:832, 2002.

[164] Xinghua Lu, M. Grobis, K. Khoo, Steven Louie, and M. Crommie. Charge transfer and screening in individual C60 molecules on metal substrates: A scanning tunneling spectroscopy and theoretical study. *Physical Review B*, 70(11):1–8, September 2004.

[165] C. W. Tang. Two-layer organic photovoltaic cell. *Applied Physics Letters*, 48(2):183, 1986.

[166] G Yu, J Gao, and JC Hummelen. Polymer photovoltaic cells: enhanced efficiencies via a network of internal donor-acceptor heterojunctions. *Science-AAAS-Weekly*, 270:1789–1790, 1995.

[167] Fan Yang, Max Shtein, and Stephen R. Forrest. Controlled growth of a molecular bulk heterojunction photovoltaic cell. *Nature Materials*, 4(1):37–41, December 2004.

[168] Serap Günes, Helmut Neugebauer, and Niyazi Serdar Sariciftci. Conjugated polymer-based organic solar cells. *Chemical reviews*, 107(4):1324–38, April 2007.

[169] Jean Roncali. Molecular bulk heterojunctions: an emerging approach to organic solar cells. *Accounts of Chemical Research*, 42(11):1719–30, November 2009.

[170] Paul Heremans, David Cheyns, and Barry P Rand. Strategies for increasing the efficiency of heterojunction organic solar cells: material selection and device architecture. *Accounts of Chemical Research*, 42(11):1740–7, November 2009.

[171] Dirk M. Guldi. Fullerene–porphyrin architectures; photosynthetic antenna and reaction center models. *Chemical Society Reviews*, 31(1):22–36, March 2002.

[172] Peter D W Boyd and Christopher a Reed. Fullerene-porphyrin constructs. *Accounts of Chemical Research*, 38(4):235–42, April 2005.

[173] Nazario Martín, Luis Sánchez, Beatriz Illescas, and Ignacio Pérez. C(60)-Based Electroactive Organofullerenes. *Chemical reviews*, 98(7):2527–2548, November 1998.

[174] Yanli Chen, Wei Su, Ming Bai, Jianzhuang Jiang, Xiyou Li, Yunqi Liu, Lingxuan Wang, and Shuangqing Wang. High performance organic field-effect transistors based on amphiphilic tris(phthalocyaninato) rare earth triple-decker complexes. *Journal of the American Chemical Society*, 127(45):15700–1, November 2005.

[175] Dennis K. P. Ng and Jianzhuang Jiang. Sandwich-type heteroleptic phthalocyaninato and porphyrinato metal complexes. *Chemical Society Reviews*, 26(6):433, 1997.

[176] Jianzhuang Jiang and Dennis KP Ng. A decade journey in the chemistry of sandwich-type tetrapyrrolato- rare earth complexes. *Accounts of Chemical Research*, 42(1):79–88, 2008.

[177] Yong Li, Yongzhong Bian, Ming Yan, Prem S. Thapaliya, Daniel Johns, Xingzhong Yan, David Galipeau, and Jianzhuang Jiang. Mixed (porphyrinato)(phthalocyaninato) rare-earth(III) double-decker complexes for broadband light harvesting organic solar cells. *Journal of Materials Chemistry*, 21(30):11131, 2011.

[178] Qi Wang, Yong Li, Xingzhong Yan, Monika Rathi, Michael Ropp, David Galipeau, and Jianzhuang Jiang. Organic photovoltaic cells made from sandwich-type rare earth phthalocyaninato double and triple deckers. *Applied Physics Letters*, 93(7):073303, 2008.

[179] Mark O. Liu and Andrew Teh Hu. Microwave-assisted synthesis of phthalocyanine–porphyrin complex and its photoelectric conversion properties. *Journal of Organometallic Chemistry*, 689(15):2450–2455, August 2004.

[180] Lung-chang Liu and Andrew Teh Hu. Synthesis of soluble functional dye phthalocyanines and perylene tetracarboxylic derivatives by microwave irradiation and their photoelectric performances. *Journal of Porphyrins and Phthalocyanines*, 7(08):565–571, 2003.

[181] Yi-Bo Wang and Zhenyang Lin. Supramolecular interactions between fullerenes and porphyrins. *Journal of the American Chemical Society*, 125(20):6072–3, May 2003.

[182] P.D.W. Boyd, M.C. Hodgson, C.E.F. Rickard, A.G. Oliver, Leila Chaker, P.J. Brothers, R.D. Bolskar, F.S. Tham, and C.A. Reed. Selective Supramolecular Porphyrin/Fullerene Interactions1. *Journal of the American Chemical Society*, 121(45):10487–10495, 1999.

[183] Meng-Sheng Liao, John D Watts, and Ming-Ju Huang. Interaction of metal porphyrins with fullerene C60: a new insight. *The journal of physical chemistry. B*, 111(17):4374–82, May 2007.

[184] Tsutomu Ishi-i, Ritsuko Iguchi, Erwin Snip, Masato Ikeda, and Seiji Shinkai. [60] fullerene can reinforce the organogel structure of porphyrin-appended cholesterol derivatives: Novel odd-even effect of the (ch2) n spacer on the organogel stability. *Langmuir*, 17(19):5825–5833, 2001.

[185] Barry C Thompson and Jean M J Fréchet. Polymer-fullerene composite solar cells. *Angewandte Chemie (International ed. in English)*, 47(1):58–77, January 2008.

[186] Beatriz Ballesteros, Gema de la Torre, Axel Shearer, Anita Hausmann, M Angeles Herranz, Dirk M Guldi, and Tomás Torres. Lanthanide(III) bis(phthalocyaninato)-[60]fullerene dyads: synthesis, characterization, and photophysical properties. *Chemistry (Weinheim an der Bergstrasse, Germany)*, 16(1):114–25, January 2010.

[187] Dirk M Guldi, Andreas Gouloumis, Purificación Vázquez, Tomás Torres, Vasilios Georgakilas, and Maurizio Prato. Nanoscale organization of a phthalocyanine-fullerene system: remarkable stabilization of charges in photoactive 1-D nanotubules. *Journal of the American Chemical Society*, 127(16):5811–3, April 2005.

[188] Francesco Sedona, Marco Di Marino, Mauro Sambi, Tommaso Carofiglio, Elisa Lubian, Maurizio Casarin, and Eugenio Tondello. Fullerene/porphyrin multi-

component nanostructures on Ag(110): from supramolecular self-assembly to extended copolymers. *ACS nano*, 4(9):5147–54, September 2010.

[189] Andreas Kiebele, Davide Bonifazi, Fuyong Cheng, Meike Stöhr, François Diederich, Thomas Jung, and Hannes Spillmann. Adsorption and dynamics of long-range interacting fullerenes in a flexible, two-dimensional, nanoporous porphyrin network. *Chemphyschem : a European journal of chemical physics and physical chemistry*, 7(7):1462–70, July 2006.

[190] Johann W. Buchler, Andre. De Cian, Jean. Fischer, Martina. Kihn-Botulinski, Helmut. Paulus, and Raymond. Weiss. Metal complexes with tetrapyrrole ligands. 40. cerium(iv) bis(octaethylporphyrinate) and dicerium(iii) tris(octaethylporphyrinate): Parents of a new family of lanthanoid double-decker and triple-decker molecules. *Journal of the American Chemical Society*, 108(13):3652–3659, 1986.

[191] Meng-Sheng Liao, John D Watts, and Ming-Ju Huang. DFT/TDDFT study of lanthanide(III) mono- and bisporphyrin complexes. *The journal of physical chemistry. A*, 110(48):13089–98, December 2006.

[192] Luis Sánchez, Roberto Otero, José María Gallego, Rodolfo Miranda, and Nazario Martín. Ordering fullerenes at the nanometer scale on solid surfaces. *Chemical reviews*, 109(5):2081–91, May 2009.

[193] K. Ai t Mansour, Pascal Ruffieux, P. Gro ning, Roman Fasel, and O. Gro ning. Positional and Orientational Templating of C60 Molecules on the Ag/Pt (111) Strain-Relief Pattern. *The Journal of Physical Chemistry C*, 113(13):5292–5299, 2009.

[194] James a Theobald, Neil S Oxtoby, Michael a Phillips, Neil R Champness, and Peter H Beton. Controlling molecular deposition and layer structure with supramolecular surface assemblies. *Nature*, 424(6952):1029–31, August 2003.

[195] Sebastian Stepanow, Magalí Lingenfelder, Alexandre Dmitriev, Hannes Spillmann, Erik Delvigne, Nian Lin, Xiaobin Deng, Chengzhi Cai, Johannes V Barth, and Klaus Kern. Steering molecular organization and host-guest interactions using two-dimensional nanoporous coordination systems. *Nature materials*, 3(4):229–33, April 2004.

[196] Sebastian Stepanow, Nian Lin, Johannes V Barth, and Klaus Kern. Non-covalent binding of fullerenes and biomolecules at surface-supported metallo-supramolecular receptors. *Chemical communications (Cambridge, England)*, (20):2153–5, May 2006.

[197] E. Mena-Osteritz and P. Bäuerle. Complexation of C60 on a Cyclothiophene Monolayer Template. *Advanced Materials*, 18(4):447–451, February 2006.

[198] Ge-Bo Pan, Jun-Min Liu, Hui-Min Zhang, Li-Jun Wan, Qi-Yu Zheng, and Chun-Li Bai. Configurations of a calix[8]arene and a C60/calix[8]arene complex on a Au(111) surface. *Angewandte Chemie (International ed. in English)*, 42(24):2747–51, June 2003.

[199] Davide Bonifazi, Hannes Spillmann, Andreas Kiebele, Michael de Wild, Paul Seiler, Fuyong Cheng, Hans-Joachim Güntherodt, Thomas Jung, and François Diederich. Supramolecular patterned surfaces driven by cooperative assembly of C60 and porphyrins on metal substrates. *Angewandte Chemie (International*

ed. in English), 43(36):4759–63, September 2004.

[200] M Di Marino, F Sedona, M Sambi, T Carofiglio, E Lubian, M Casarin, and E Tondello. STM investigation of temperature-dependent two-dimensional supramolecular architectures of C60 and amino-tetraphenylporphyrin on Ag(110). *Langmuir : The ACS Journal of Surfaces and Colloids*, 26(4):2466–72, February 2010.

[201] F. Nishiyama, T. Yokoyama, T. Kamikado, S. Yokoyama, S. Mashiko, K. Sakaguchi, and K. Kikuchi. Interstitial Accommodation of C60 in a Surface-Supported Supramolecular Network. *Advanced Materials*, 19(1):117–120, January 2007.

[202] Tomas Samuely, S.X. Liu, Marco Haas, Silvio Decurtins, T.A. Jung, and M. Sto hr. Self-Assembly of Individually Addressable Complexes of C60 and Phthalocyanines on a Metal Surface: Structural and Electronic Investigations. *The Journal of Physical Chemistry C*, 113(45):19373–19375, 2009.

[203] Soichiro Yoshimoto, Eishi Tsutsumi, Yosuke Honda, Yasujiro Murata, Michihisa Murata, Koichi Komatsu, Osamu Ito, and Kingo Itaya. Controlled Molecular Orientation in an Adlayer of a Supramolecular Assembly Consisting of an Open-Cage C60 Derivative and ZnII Octaethylporphyrin on Au(111). *Angewandte Chemie*, 116(23):3106–3109, June 2004.

[204] Soichiro Yoshimoto, Yosuke Honda, Yasujiro Murata, Michihisa Murata, Koichi Komatsu, Osamu Ito, and Kingo Itaya. Dependence of molecular recognition of fullerene derivative on the adlayer structure of zinc octaethylporphyrin formed on Au(100) surface. *The journal of physical chemistry. B*, 109(18):8547–50, May 2005.

[205] Soichiro Yoshimoto, Yosuke Honda, Osamu Ito, and Kingo Itaya. Supramolecular pattern of fullerene on 2D bimolecular "chessboard" consisting of bottom-up assembly of porphyrin and phthalocyanine molecules. *Journal of the American Chemical Society*, 130(3):1085–92, January 2008.

[206] Wende Xiao, Daniele Passerone, Pascal Ruffieux, Kamel Aït-Mansour, Oliver Gröning, Erio Tosatti, Jay S Siegel, and Roman Fasel. C60/corannulene on Cu(110): a surface-supported bistable buckybowl-buckyball host-guest system. *Journal of the American Chemical Society*, 130(14):4767–71, April 2008.

[207] Tobias Bauert, Kim K Baldridge, Jay S Siegel, and Karl-Heinz Ernst. Surface-assisted bowl-in-bowl stacking of nonplanar aromatic hydrocarbons. *Chemical communications (Cambridge, England)*, 47(28):7995–7, July 2011.

[208] Thomas Frederiksen, K.J. Franke, Andrés Arnau, Gunnar Schulze, J.I. Pascual, and Nicolás Lorente. Dynamic Jahn-Teller effect in electronic transport through single C60 molecules. *Physical Review B*, 78(23):233401, 2008.

[209] I. Fernández-Torrente, K. Franke, and J. Pascual. Vibrational Kondo Effect in Pure Organic Charge-Transfer Assemblies. *Physical Review Letters*, 101(21):217203, November 2008.

[210] M. Grobis, a. Wachowiak, R. Yamachika, and M. F. Crommie. Tuning negative differential resistance in a molecular film. *Applied Physics Letters*, 86(20):204102, 2005.

[211] K. Franke, G. Schulze, N. Henningsen, I. Fernández-Torrente, J. Pascual,

S. Zarwell, K. Rück-Braun, M. Cobian, and N. Lorente. Reducing the Molecule-Substrate Coupling in C60-Based Nanostructures by Molecular Interactions. *Physical Review Letters*, 100(3):036807, January 2008.

[212] T Sakurai, Q K Xue, T Hashizume, and H Shinohara. Scanning tunneling microscopy of Fullerene Study. *Progress in Surface Science*, 51(4):263–408, 1996.

[213] a. Tamai, a. Seitsonen, R. Fasel, Z.-X. Shen, J. Osterwalder, and T. Greber. Doping-induced reorientation of C60 molecules on Ag(111). *Physical Review B*, 72(8):085421, August 2005.

[214] H. Li, K. Pussi, K. Hanna, L.-L. Wang, D. Johnson, H.-P. Cheng, H. Shin, S. Curtarolo, W. Moritz, J. Smerdon, R. McGrath, and R. Diehl. Surface Geometry of C60 on Ag(111). *Physical Review Letters*, 103(5):056101, July 2009.

[215] P Bhyrappa and K Karunanithi. Porphyrin-fullerene, C60, cocrystallates: influence of C60 on the porphyrin ring conformation. *Inorganic chemistry*, 49(18):8389–400, September 2010.

[216] D. Keeling, M. Humphry, R. Fawcett, P. Beton, C. Hobbs, and L. Kantorovich. Bond Breaking Coupled with Translation in Rolling of Covalently Bound Molecules. *Physical Review Letters*, 94(14):146104, April 2005.

[217] M. Muntwiler, W. Auwärter, a. Seitsonen, J. Osterwalder, and T. Greber. Rocking-motion-induced charging of C60 on h-BN/Ni(111). *Physical Review B*, 71(12):121402, March 2005.

[218] Uwe Bovensiepen, Hrvoje Petek, and Martin Wolf. *Dynamics at Solid State Surfaces and Interfaces: Volume 1-Current Developments*. Wiley-VCH, 2010.

[219] John E Fischer, Paul A Heiney, and Amos B Smith III. Solid-state chemistry of fullerene-based materials. *Accounts of Chemical Research*, 25(3):112–118, 1992.

[220] I Horcas, R Fernandez, JM Gomez-Rodriguez, J Colchero, JWSXM Gómez-Herrero, and AM Baro. Wsxm: A software for scanning probe microscopy and a tool for nanotechnology. *Review of Scientific Instruments*, 78(1):013705–013705, 2007.

[221] Simon C Benjamin, Arzhang Ardavan, G Andrew D Briggs, David a Britz, Daniel Gunlycke, John Jefferson, Mark a G Jones, David F Leigh, Brendon W Lovett, Andrei N Khlobystov, S a Lyon, John J L Morton, Kyriakos Porfyrakis, Mark R Sambrook, and Alexei M Tyryshkin. Towards a fullerene-based quantum computer. *Journal of Physics: Condensed Matter*, 18(21):S867–S883, May 2006.

[222] O. Kurnosikov, O. Adam, H. Swagten, W. de Jonge, and B. Koopmans. Probing quantum wells induced above a subsurface nanocavity in copper. *Physical Review B*, 77(12):125429, March 2008.

[223] Peter Liljeroth, Karin Overgaag, Ana Urbieta, Bruno Grandidier, Stephen Hickey, and Daniël Vanmaekelbergh. Variable Orbital Coupling in a Two-Dimensional Quantum-Dot Solid Probed on a Local Scale. *Physical Review Letters*, 97(9):1–4, September 2006.

[224] BC Stipe, MA Rezaei, and W Ho. Single-molecule vibrational spectroscopy and microscopy. *Science*, 280(5370):1732–1735, 1998.

[225] Cyrus F Hirjibehedin, Chiung-yuan Lin, Alexander F Otte, Markus Ternes, Christopher P Lutz, Barbara A Jones, and Andreas J Heinrich. Large Magnetic Anisotropy of a a Surface Molecular Network. (August):1199–1203, 2007.

[226] N. Knorr, H. Brune, M. Epple, a. Hirstein, M. Schneider, and K. Kern. Long-range adsorbate interactions mediated by a two-dimensional electron gas. *Physical Review B*, 65(11):1–5, March 2002.

[227] Fabien Silly, Marina Pivetta, Markus Ternes, François Patthey, Jonathan Pelz, and Wolf-Dieter Schneider. Creation of an Atomic Superlattice by Immersing Metallic Adatoms in a Two-Dimensional Electron Sea. *Physical Review Letters*, 92(1):016101, January 2004.

[228] Harald Brune, Marcella Giovannini, Karsten Bromann, and Klaus Kern. Self-organized growth of nanostructure arrays on strain-relief patterns. 394(July):451–453, 1998.

[229] Kazuo Yamashita, Yutaka Harima, and Tatsuro Matsubayashi. Conductance control of porphyrin solids by molecular design and doping. *The Journal of Physical Chemistry*, 93(13):5311–5315, 1989.

[230] Roberto Robles, Nicolás Lorente, Hironari Isshiki, Jie Liu, Keiichi Katoh, Brian K Breedlove, Masahiro Yamashita, and Tadahiro Komeda. Spin doping of individual molecules by using single-atom manipulation. *Nano letters*, 12(7):3609–12, July 2012.

[231] Wolfgang Krenner, Florian Klappenberger, Dirk K§hne, Katharina Diller, Zhi-Rong Qu, Mario Ruben, and Johannes V Barth. Positioning of single co atoms steered by a self-assembled organic molecular template. *The Journal of Physical Chemistry Letters*, 2(13):1639–1645, 2011.

[232] R Decker, U Schlickum, F Klappenberger, G Zoppellaro, S Klyatskaya, M Ruben, JV Barth, and H Brune. Using metal-organic templates to steer the growth of fe and co nanoclusters. *Applied Physics Letters*, 93(24):243102–243102, 2008.

[233] Daniel Wegner, Ryan Yamachika, Xiaowei Zhang, Yayu Wang, Tunna Baruah, Mark Pederson, Bart Bartlett, Jeffrey Long, and Michael Crommie. Tuning Molecule-Mediated Spin Coupling in Bottom-Up-Fabricated Vanadium-Tetracyanoethylene Nanostructures. *Physical Review Letters*, 103(8):1–4, August 2009.

[234] P Gambardella, a Dallmeyer, K Maiti, M C Malagoli, W Eberhardt, K Kern, and C Carbone. Ferromagnetism in one-dimensional monatomic metal chains. *Nature*, 416(6878):301–4, March 2002.

[235] Noriyuki Tsukahara, Ken-ichi Noto, Michiaki Ohara, Susumu Shiraki, Noriaki Takagi, Shik Shin, and Maki Kawai. Adsorption-Induced Switching of Magnetic Anisotropy in a Single Iron(II) Phthalocyanine Molecule on an Oxidized Cu(110) Surface. *Physical Review Letters*, 102(16):1–4, April 2009.

[236] R Bennewitz, J N Crain, a Kirakosian, J-L Lin, J L McChesney, D Y Petrovykh, and F J Himpsel. Atomic scale memory at a silicon surface. *Nanotechnology*, 13(4):499–502, August 2002.

[237] R Yamachika, M Grobis, A Wachowiak, and MF Crommie. Controlled atomic doping of a single c60 molecule. *Science*, 304(5668):281–284, 2004.

[238] Wolfgang Hieringer, Ken Flechtner, Andreas Kretschmann, Knud Seufert, Willi Auwärter, Johannes V Barth, Andreas Görling, Hans-Peter Steinrück, and J Michael Gottfried. The surface trans effect: Influence of axial ligands on the surface chemical bonds of adsorbed metalloporphyrins. *Journal of the American Chemical Society*, 133(16):6206–6222, 2011.

[239] Knud Seufert, Willi Auwärter, and Johannes V Barth. Discriminative response of surface-confined metalloporphyrin molecules to carbon and nitrogen monoxide. *Journal of the American Chemical Society*, 132(51):18141–18146, 2010.

[240] Christian Wäckerlin, Dorota Chylarecka, Armin Kleibert, Kathrin Müller, Cristian Iacovita, Frithjof Nolting, Thomas a Jung, and Nirmalya Ballav. Controlling spins in adsorbed molecules by a chemical switch. *Nature communications*, 1:61, January 2010.

[241] Pietro Gambardella, Sebastian Stepanow, Alexandre Dmitriev, Jan Honolka, Frank M F de Groot, Magalí Lingenfelder, Subhra Sen Gupta, D D Sarma, Peter Bencok, Stefan Stanescu, Sylvain Clair, Stéphane Pons, Nian Lin, Ari P Seitsonen, Harald Brune, Johannes V Barth, and Klaus Kern. Supramolecular control of the magnetic anisotropy in two-dimensional high-spin Fe arrays at a metal interface. *Nature materials*, 8(3):189–93, March 2009.

[242] Peter Liljeroth, Jascha Repp, and Gerhard Meyer. Current-induced hydrogen tautomerization and conductance switching of naphthalocyanine molecules. *Science (New York, N.Y.)*, 317(5842):1203–6, August 2007.

[243] Shuan Pan, Qiang Fu, Tian Huang, Aidi Zhao, Bing Wang, Yi Luo, Jinlong Yang, and Jianguo Hou. Design and control of electron transport properties of single molecules. *Proceedings of the National Academy of Sciences of the United States of America*, 106(36):15259–63, September 2009.

[244] Micol Alemani, Maike V Peters, Stefan Hecht, Karl-Heinz Rieder, Francesca Moresco, and Leonhard Grill. Electric field-induced isomerization of azobenzene by STM. *Journal of the American Chemical Society*, 128(45):14446–7, November 2006.

[245] Fabian Mohn, Jascha Repp, Leo Gross, Gerhard Meyer, Matthew S Dyer, and Mats Persson. Reversible bond formation in a gold-atom–organic-molecule complex as a molecular switch. *Physical Review Letters*, 105(26):266102, 2010.

[246] Nikolai Wintjes, Davide Bonifazi, Fuyong Cheng, Andreas Kiebele, Meike Stöhr, Thomas Jung, Hannes Spillmann, and François Diederich. A Supramolecular Multiposition Rotary Device. *Angewandte Chemie*, 119(22):4167–4170, May 2007.

[247] Willi Auwärter, Knud Seufert, Florian Klappenberger, Joachim Reichert, Alexander Weber-Bargioni, Alberto Verdini, Dean Cvetko, Martina Dell'Angela, Luca Floreano, Albano Cossaro, Gregor Bavdek, Alberto Morgante, Ari P. Seitsonen, and Johannes V. Barth. Site-specific electronic and geometric interface structure of Co-tetraphenyl-porphyrin layers on Ag(111). *Physical Review B*, 81(24):245403, June 2010.

[248] Karmen Comanici, Florian Buchner, Ken Flechtner, Thomas Lukasczyk, J Michael Gottfried, Hans-Peter Steinrück, and Hubertus Marbach. Understanding the contrast mechanism in scanning tunneling microscopy (STM) images of an intermixed tetraphenylporphyrin layer on Ag(111). *Langmuir : The ACS Journal of Surfaces and Colloids*, 24(5):1897–901, March 2008.

[249] Knud Seufert, Marie-Laure Bocquet, Willi Auwärter, Alexander Weber-Bargioni, Joachim Reichert, Nicolás Lorente, and Johannes V Barth. Cis-dicarbonyl binding at cobalt and iron porphyrins with saddle-shape conformation. *Nature chemistry*, 3(2):114–9, March 2011.

[250] Ken Flechtner, Andreas Kretschmann, Hans-Peter Steinrück, and J Michael Gottfried. No-induced reversible switching of the electronic interaction between a porphyrin-coordinated cobalt ion and a silver surface. *Journal of the American Chemical Society*, 129(40):12110–12111, 2007.

[251] Linus Pauling. *The nature of the chemical bond and the structure of molecules and crystals: an introduction to modern structural chemistry*, volume 18. Ithaca, NY, Cornell University Press, 1960.

[252] Harald Ibach. *Physics of surfaces and interfaces.* Springer, 2007.

[253] S. Stepanow, P. Miedema, a. Mugarza, G. Ceballos, P. Moras, J. Cezar, C. Carbone, F. de Groot, and P. Gambardella. Mixed-valence behavior and strong correlation effects of metal phthalocyanines adsorbed on metals. *Physical Review B*, 83(22):220401, June 2011.

[254] G Kresse and J Hafner. Ab initio molecular dynamics for open-shell transition metals. *Physical Review B*, 48(17):13115, 1993.

[255] John P Perdew, Kieron Burke, and Matthias Ernzerhof. Generalized gradient approximation made simple. *Physical Review Letters*, 77(18):3865–3868, 1996.

[256] Stefan Grimme. Semiempirical gga-type density functional constructed with a long-range dispersion correction. *Journal of Computational Chemistry*, 27(15):1787–1799, 2006.

[257] N Lorente, E Hasselbrink, and BI Lundqvist. Dynamics, handbook of surface science, 2008.

[258] Knud Johannes Seufert. *Surface anchored porphyrins - investigations of assembly, reactivity, manipulation and in-situ synthesis.* PhD thesis, Technische Universität München, 2011.

[259] Jorge Lobo-Checa, Manfred Matena, Kathrin Müller, Jan Hugo Dil, Fabian Meier, Lutz H Gade, Thomas a Jung, and Meike Stöhr. Band formation from coupled quantum dots formed by a nanoporous network on a copper surface. *Science (New York, N.Y.)*, 325(5938):300–3, July 2009.

[260] Y Pennec, W Auwärter, A Schiffrin, A Weber-Bargioni, A Riemann, and JV Barth. Supramolecular gratings for tuneable confinement of electrons on metal surfaces. *Nature nanotechnology*, 2(2):99–103, 2007.

[261] Jenny Nelson. Organic photovoltaic films. *Current Opinion in Solid State and Materials Science*, 6(1):87–95, 2002.